Title

Southeast Asian autumn monsoon variability over the last 45,000 years

Author

Patterson, Elizabeth W

Publication Date

2023

Peer reviewed|Thesis/dissertation

UNIVERSITY OF CALIFORNIA,
IRVINE

Southeast Asian autumn monsoon variability over the last 45,000 years

DISSERTATION

submitted in partial satisfaction of the requirements
for the degree of

DOCTOR OF PHILOSOPHY

in Earth System Science

by

Elizabeth W. Patterson

Dissertation Committee:
Professor Kathleen Johnson, Chair
Professor Claudia I. Czimczik
Professor Jin-Yi Yu

2023

TABLE OF CONTENTS

Page

LIST OF FIGURES

LIST OF TABLES

ACKNOWLEDGEMENTS

My work was supported by US NSF P2C2 awards # 2103129/1603056, the Ridge to Reef NSF Research Traineeship award # DGE- 1735040, and the AGeS2 (Awards for Geochronology Student research) Program award # EAR-1759200 and -1759353. Chapter 2 is a reproduction of an article as it appears in the Proceedings of the National Academy of Sciences 2023. Coauthors include K.R. Johnson, M.L Griffiths, C.W. Kinsley, D. McGee, X. Du, T. Pico, A. Wolf, V. Ersek, R.A. Mortlock, K.A. Yamoah, T.N. Bùi, M.X. Trần, Q. Đỗ-Trọng, T.V. Võ, and T.H. Đinh. The dissertation author is the primary investigator and author of this paper.

I would like to thank my advisor, Kathleen Johnson, for your mentorship and all the amazing opportunities. You have taught me so much more than science and I wish to follow your example wherever my career may lead me.

I would like to thank Claudia Czimczik and Jin-Yi Yu for serving on my dissertation committee and providing helpful guidance throughout my time at UCI.

I thank members of my lab group, Chris Wood, Jessica Wang, Kevin Wright, Annabel Wolf, Bryant Pahl, Cesiah Coreas, Rhys-Jasper Leon, Kumalie Wijesekare, and Cynthia Abuede, whose knowledge and support has been invaluable over the past five years.

I would like to thank all my collaborators, especially Mick Griffiths, Christopher Kinsley, David McGee, Vanessa Skiba, Alliya Akhtar, and Quoc Đỗ-Trọng. I would also like to thank the Phong Nha-Ke Bang National Park management board and community members T.N. Bùi, M.X. Trần, T.V. Võ, T.H. Đinh, D. Nguyen, and H.Q. Nguyen for their support of our research in the park.

I would like to thank my friends and family for their support through the years. A special thanks to my partner, Alex, for an amazing 4 years and running. I'm excited for what the future may hold and our next adventure in New York. Thank you to my mother, Virginia Weis, for just about everything. You were my secret weapon through all of this. Thank you to my brother Will Patterson and his wife, Madeleine, for the engaging rants and the life changing sunscreen products.

Lastly, I must also thank reality tv – specifically the Bachelor franchise – and sports – specifically tennis and the works of R. Federer – for keeping me sane through all those hours of lab work. Couldn't have done it without you.

VITA

Elizabeth W. Patterson

Education

Ph.D. Earth System Science, University of California, Irvine, CA	2018-2023
M.S. Geoscience, University of Arizona, Tucson, AZ	2016-2018
B.S. Geology, Bates College, Lewiston, ME	2012-2016

Publications

Patterson, E.W., K.R. Johnson, M.L. Griffiths, C.W. Kinsley, D. McGee, X. Du, T. Pico, A. Wolf, V. Ersek, R. Mortlock, K.A. Yamoah, T.N. Bui, M.X. Tran, Q. Do-Trong, T.V. Vo, and T.H. Dinh, 2023. Glacial changes in sea level modulated millennial-scale variability of Southeast Asian autumn monsoon rainfall. *Proceedings of the National Academy of Sciences*, *120*(27), p.e2219489120.

Grants and Awards

2023	Inclusive Excellence Award, Department of Earth System Science, UCI
2022-2023	Ridge to Reef (R2R) NSF Fellow ($68,000)
2020-2021	Ridge to Reef (R2R) NSF Fellow ($68,000)
2020	UCI Division of Teaching Excellence and Innovation Fellowship ($5,000)
2020	GSA Award for Geochronology Student Research (AGeS2) grant ($9,000)
2019-2023	Ridge to Reef NSF Research Trainee at UCI
2019	GSA Graduate Student Research Grant ($2,200)
2018	Graduate Deans Recruitment Fellowship, UCI ($5,000)
2018	ChevronTexaco Geology Fellowship ($1,400)
2017	Outstanding Student Paper Award, AGU Fall Meeting
2012-2016	Dean's list for all semesters enrolled at Bates College
2016	Bates student travel grant ($900)
2015	Bouley Fund, Bates College ($500)
2015	Bates Student Research Fund ($800)
2014	NSF REU at Oregon State University CEOAS ($5,650)

Presentations

Glacial changes in sea level modulated millennia-scale variability of the Southeast Asian autumn monsoon (Oral) In *AGU Fall Meeting*, Chicago, Illinois, December 2022

Glacial changes in sea level modulated millennia-scale variability of the Southeast Asian autumn monsoon (Oral) In: *Climate Change: The Karst Record IX (KR9)*, Innsbruck, Austria, July 2022

A stalagmite record (4-45 ka) of fall/winter monsoon variability from central Vietnam (Poster) In: *AGU Fall Meeting*, New Orleans, Louisiana, December 2021

Using stalagmites to reconstruct Southeast Asian hydroclimate (Oral) Bates College, Zoom, May 2021. INVITED SEMINAR

A preliminary record (4-45 ka) of fall/winter monsoon variability from central Vietnam (Poster) In: *KROnline Seminar*, Zoom, January 2021

Reconstructing 20,000 years of Southeast Asian monsoon variability (Poster) In: *3rd Annual Environmental Research Symposium*, Irvine, California, December 2019

Reconstructing Southeast Asian monsoon variability with speleothems (Oral) In: *Advanced Climate Dynamics Courses (ACDC)*, Wawona, California, September 2019

Reconstructing 20,000 years of Southeast Asian monsoon variability (Poster) In: *Speleothem Summer School (S4)*, Cluj-Napoca, Romania, August 2019

A northern Australian coral record of seasonal rainfall and terrestrial runoff (1775-1983) (Oral) In: *University of Arizona Geoscience Symposium (Geodaze)*, Tucson, Arizona, March 2018

A northern Australian coral record of seasonal rainfall and terrestrial runoff (1775-1986) (Poster) In: *American Geophysical Union (AGU) Fall Meeting*, New Orleans, Louisiana, December 2017

Climate variability in northern Australia using coral-based reconstructions of rainfall and SST (Poster) In: *University of Arizona Geoscience Symposium (Geodaze)*, Tucson, Arizona, March 2017

Identifying the sources and amounts of carbon buried in the salt marshes and sea grass beds of Lagoa Dos Patos in Rio Grande, Brazil (Poster) In: *Mount David Summit*, Lewiston, Maine, April 2016

Identifying the sources and amounts of carbon buried in the salt marshes and sea grass beds of Lagoa Dos Patos in Rio Grande, Brazil (Poster) In: *European Geoscience Union General Assembly (EGU)*, Vienna, April 2016

Teaching and mentoring

Spring, Fall 2022: Guest lecture (4 lectures), Physical Geology, UCI

- Topics: “plate tectonics”, “weathering and sedimentary rocks”, “metamorphic rocks”, and “volcanoes”

Fall 2021: Teaching Assistant, GIS for Environmental Science, UCI
Spring 2019, 2020, 2022: Teaching Assistant, Physical Geology, UCI
Fall 2019: Teaching Assistant, Catastrophes, UCI
Spring 2017: Teaching Assistant, Ocean Sciences, University of Arizona
Spring 2016: Teaching Assistant, Earth Surface Environments, Bates College
Spring 2014, Fall 2015: Teaching Assistant, Environmental Geochemistry, Bates College

Undergraduate mentoring

Rhys-Jasper Leon (UCI ’23) – Honors Thesis	2021-2023
Kumalie Wijesekare (UCI ’23)	2022-2023
Cynthia Abuede (UCI ’23)	2022-2023
Cesiah Coreas (UCI ’22) – Independent Project	2019-2022
Maria Snyder (UA ’20)	2018
Jessie McCraw (UA ’18)	2017-2018

Involvement

Unlearning Racism in Geosciences (URGE) 2021-2023

- Member of UCI ESS URGE pod to develop new departmental policies focused on Diversity, Equity, and Inclusion

Climate Literacy, Empowerment And iNquiry (CLEAN) 2018-2023

- Climate focused educational program for middle schoolers led by graduate students
- Board Member 2020-2023
- Lead presenter of the paleoclimate and weather & climate lessons
- Developed online and in person curriculum

Member of Planning Committee for Summer School on Speleothem Science (S4) 2019-2023

- S4 is a graduate student-led summer school on speleothem science (cave deposits).
- Planned S4 Online on Zoom (January-February 2022), Mini S4 in Innsbruck, Austria (July 2022), and S4 2023 in Sao Paulo, Brazil (August, 2023)

Department Seminar Committee (UCI ESS) 2021-2022

- Graduate student representative

‘Half-baked’ Co-organizer 2020-2022

- Graduate student-led department seminar series (UCI)

Mentor for Arizona’s Science, Engineering, and Math Scholars Program (ASEMS) 2017-2018

- Mentoring program for undergraduates from underrepresented backgrounds

Geodaze planning committee 2017-2018

- Graduate student-led conference at the University of Arizona, Dept. of Geosciences

University of Arizona Travel Grant Judge 2016-2018

Skills
Field

- Cave monitoring and stalagmite sampling
- Sampling sediment cores from marshes and seagrass beds
- Geological field mapping

Laboratory

- ICP-OES, ICP-MS, LA-ICP-MS
- Kiel IV Carbonate device with a Delta V Plus isotope ratio mass spectrometry (IRMS)
- Drilling coral and stalagmite samples using a micromill

Computational

- Advanced in MATLAB and Microsoft Office
- Proficient in Python, R, and ArcGIS

Professional Affiliations and Societies
American Geophysical Union (2017-present)
Geological Society of America (2014-present)
Phi Beta Kappa
Sigma Xi

ABSTRACT OF THE DISSERTATION

Southeast Asian autumn monsoon variability over the last 45,000 years

By

Elizabeth W. Patterson

Doctor of Philosophy in Earth System Science

University of California, Irvine, 2023

Professor Kathleen Johnson, Chair

The Southeast Asian autumn monsoon affects millions of people along the eastern coast of Mainland Southeast Asia. Relatively small changes to autumn rainfall amount can cause floods and prolonged droughts, which impact regional agriculture, water availability, and infrastructure. Thus, understanding Southeast Asian autumn monsoon variability and how it might change in the future is crucial for the livelihood of those living in the region. However, instrumental records are short and future projections are unclear, leaving the variability of the autumn monsoon poorly constrained. Records of past climate from reliable hydroclimate archives, such as cave deposits, would improve our understanding of the Southeast Asian autumn monsoon, particularly on longer timescales.

My dissertation uses a stalagmite from central Vietnam to generate a multiproxy record of the Southeast Asian autumn monsoon from 45 to 4 ka. I use stable carbon isotopes and trace elements to generate a record of local rainfall change, which shows substantial, and at times abrupt, change over the last 45,000 years. Using the record in conjunction with climate model output, I identify ice sheet-driven sea-level change as the

primary driver of Southeast Asian autumn monsoon variability on millennial to orbital timescales. During periods of low sea level, the exposure of nearby landmasses (the Gulf of Tonkin and the South China Shelf) decreases autumn moisture delivery to central Vietnam. The opposite occurs during periods of high sea level. I next semi-quantitatively estimate this sea-level-driven rainfall change using calcium isotopes, a relatively new proxy. The calcium isotope record reveals that when sea level was low during the termination of the last glacial period, rainfall amount was up to 50 % less than modern levels. Lastly, I use stable oxygen isotopes to investigate large-scale changes in hydroclimate. I find that the stalagmite oxygen isotope record reflects changes in regional precipitation as well as an in-cave process called "prior calcite precipitation". After removing this in-cave effect using a geochemical model, I find that the oxygen isotope record follows the expected pattern from regional stalagmite records and climate model output.

The collective results of my dissertation provide new insights to the past variability and main drivers of the Southeast Asian autumn monsoon over the last 45,000 years. By employing cutting-edge proxies and innovative geochemical models, I have also contributed significant advancements to the field, with far-reaching implications for speleothem science. Moreover, my results contribute to the validation of climate model output, which improve projections of future hydroclimate change.

CHAPTER 1: INTRODUCTION

Supporting information located in Appendix A.

1.1. The Southeast Asian autumn monsoon

In most tropical monsoon regions, the summer monsoon drives local rainfall variability. However, along the eastern coasts of many of these regions, the oft-overlooked autumn monsoon strongly influences local hydroclimate (Ramesh et al., 2021). One such region is Mainland Southeast Asia (MSEA), where the Southeast Asian autumn monsoon impacts millions of people along the eastern coast of Vietnam. Much of MSEA receives the majority of its annual rainfall from the southwesterly summer monsoon (strongest from June – August), where moisture is sourced and transported from the Indian Ocean and Bay of Bengal (Figure 1.1a) (Misra & DiNapoli, 2014). The onset of the autumn monsoon (strongest from September – November) occurs with the southward shift of the Intertropical Convergence Zone (ITCZ), which changes the prevailing wind direction from the southwest to the northeast, bringing moisture from the western Pacific and South China Sea (Wolf et al., 2020). This northeasterly moisture is then orographically uplifted by the Truong Son mountains, a N-S trending mountain range along the Vietnam – Laos border, concentrating autumnal rainfall in eastern Vietnam, particularly along the central coast (Figure 1.1b)(Sengupta & Nigam, 2019).

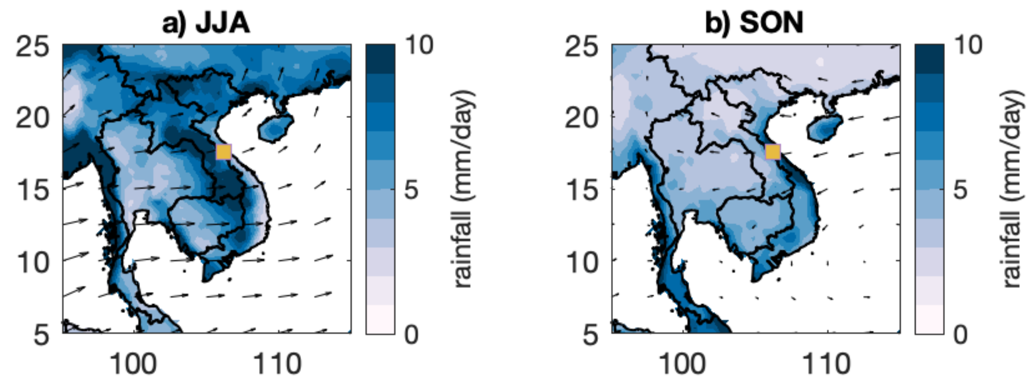

Figure 1.1. Rainfall and wind climatology of Mainland Southeast Asia. Average a) JJA and b) SON rainfall (1951-2007) derived from Asian Precipitation-Highly Resolved Observational Data Integration Towards Evaluation (APHRODITE)(Yatagai et al., 2012) and 850 mb winds (1951-2007) derived from NCEP reanalysis winds (Kalnay et al., 1996). The yellow square denotes the location of the study site. Figure modified from Patterson et al., 2023.

Variations in autumn rainfall amount have large impacts on regional agriculture, water availability, and infrastructure in central Vietnam. Tropical cyclones during the autumn monsoon cause catastrophic flooding (Luu et al., 2020, 2021; Nguyen-Thi et al., 2012). Droughts, even short in duration, strongly affect agriculture (T. L. T. Du et al., 2018; Stojanovic et al., 2020), one of the largest industries in the region. Thus, understanding autumn rainfall variability and how it might change in the future has important implications for the livelihood of the millions living in the region. While modern instrumental data suggest that autumn rainfall amount and tropical cyclones may increase in the future (Wang et al., 2015), recent CMIP6 climate model projections of precipitation in Vietnam only show a moderate increase of 9 % and 11% in the 21st century for the SSP2-4.5 and SSP5-8.5 scenarios, respectively (Supharatid et al., 2021). Notably, the CMIP6 models exhibit a strong wet bias in central Vietnam, likely because of the complex topography and low density of instrumental data (Supharatid et al., 2021), making future projections of hydroclimate change in the region unreliable. Records of past climate would help constrain the variability of the Southeast Asian autumn monsoon and its drivers over a range of timescales. Comparing these records to paleoclimate model output, would help identify which climate models best simulate rainfall variability, improving our estimates of future monsoon change.

Our understanding of past Southeast Asian autumn monsoon variability is limited, particularly on longer timescales. Instrumental records draw strong links between autumn rainfall and local sea surface temperature and the El Niño Southern Oscillation (Chen et al., 2012; Li et al., 2015; Wang et al., 2015). However, these records cover less than a century, leaving the long-term drivers of the autumn monsoon largely unknown. Although there are many hydroclimate paleorecords from MSEA (Chawchai et al., 2021; Cook et al., 2010; Griffiths et al., 2020; Wang et al., 2019; Yamoah et al., 2016, 2021), there are relatively few from central Vietnam or of the autumn monsoon (Buckley et al., 2017; He et al., 2021; Sun et al., 2018). Generating new paleorecords of the Southeast Asian autumn monsoon, particularly during periods of abrupt or rapid change, would provide important advancements in our understanding of this understudied phenomenon. This dissertation uses a speleothem, a reliable paleoarchive of hydroclimate, to reconstruct local and regional hydroclimate variability in central Vietnam. The remainder of the introduction will introduce the study site and sample (*section 1.2*), discuss the speleothem archive and its proxies (*section 1.3*), and outline the research questions and data chapters in the dissertation (*sections 1.4 and 1.5*).

1.2. Study site

All samples collected for this dissertation are from Phong Nha-Ke Bang National Park in Quang Binh Province, Vietnam (Figure 1.1). Located on the eastern flank of the Truong Son mountain range, Phong Nha-Ke Bang National Park is ideally located to study the Southeast Asian autumn monsoon because the mountains act as an orographic barrier, blocking moisture from the SW summer monsoon and trapping moisture from the NE autumn monsoon. From 1951 – 2007 Phong Nha-Ke Bang National Park received 47% of its annual rainfall during the autumn monsoon (SON) and only 30% during JJA (Yatagai et al., 2012). Thus, paleorecords of hydroclimate from the park should reflect a combination of summer and autumn rainfall, with a particularly strong influence from the autumn monsoon.

The speleothem sample used in this dissertation (HH-1) was collected from Hoa Huong cave (17.5°N, 106.2°E, Elev.411 m). The karst above Hoa Huong cave, which is covered in dense forest, ranges in thickness from meters near the entrance to >100 meters in deeper sections of the cave. Cave monitoring data collected since March 2020 demonstrate that Hoa Huong cave is well-suited for speleothem-based paleoclimate reconstruction. Mean cave temperature is 20 °C, close to the mean annual surface air temperature, with a small seasonal cycle of 1.5-2 °C and relatively humidity is consistently high (>95 %). Additional cave monitoring data and analyses can be found in *Appendix A.*

Speleothem sample HH-1, is a 3.7 m-long previously broken stalagmite that was collected ~150 m from the cave entrance in March 2020 (Figure 1.2). All three data chapters (Chapters 2-4) use geochemical measurements from HH-1. I discuss how speleothems are used as a paleoarchive next.

Figure 1.2. Scans of stalagmite HH-1. See *Appendix A* for image with U-Th dates labeled.

1.3. Speleothems as archives of past hydroclimate

Speleothems, cave deposits, are reliable paleoclimate archives of the last 500,000 years. They are particularly suitable for paleoclimate reconstructions because they are often well preserved, are deposited in continuous layers, can be precisely dated using U-Th techniques, and contain a variety of environmental and climatic proxies (Table 1.1) (Fairchild et al., 2006). The number of speleothem-based paleoclimate records has increased in recent years, forming an extensive global network (Comas-Bru et al., 2020), which when combined with other paleoclimate archives, has dramatically improved our understanding of past climate. In low-latitude and monsoon regions, a variety of speleothem geochemical proxies have been successfully used to reconstruct local and regional hydroclimate variability.

1.3.1. Speleothem formation

Speleothems are calcium carbonate formations ($CaCO_3$) that form as either calcite or aragonite in limestone caves. When precipitation percolates into the soil, it is exposed to higher pCO_2 levels from root and microbial respiration, forming a weak carbonic acid (Eq. 1). Carbonic acid dissolves limestone bedrock as it moves through the epikarst, the bedrock above the cave, carrying Ca^{2+} ions (Eq. 2). Once it reaches the cave, the lower pCO_2 within the cave causes CO_2 degassing from the drip water (the water feeding a cave deposit), which results in calcite precipitation and speleothem formation (Eq. 3, Figure 1.3) (Fairchild et al., 2006). The geochemistry of the drip water reflects a variety of environmental and climatic factors. When calcite precipitates from the drip water to form a speleothem, the speleothem preserves this geochemical signature. These signatures (proxies) can be measured to create records of past climate change.

$$H_2O + CO_2 \rightarrow H_2CO_3 \qquad \text{(Eq. 1)}$$

$$CaCO_3 + H_2CO_3 \rightarrow Ca^{2+} + 2HCO^{3-} \qquad \text{(Eq. 2)}$$

$$Ca^{2+} + 2HCO^{3-} \rightarrow CaCO_3 + H_2O + CO_2 \qquad \text{(Eq. 3)}$$

Even though speleothems refer to all secondary minerals that form in caves, most paleoclimate reconstructions utilize stalagmites due to their simple growth geometry and progressively layered formation (Fairchild & Baker, 2012).

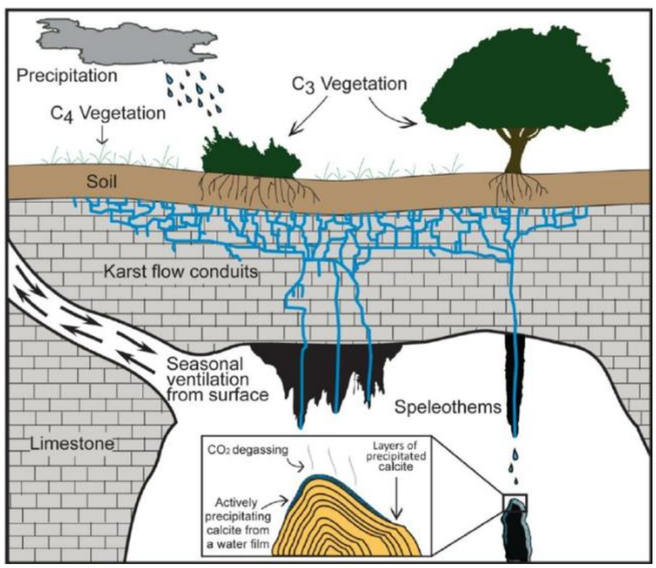

Figure 1.3. Schematic of speleothem formation. Figure adapted from Meyer et al. (2011)**.**

1.3.2. U-Th Dating

U-series dating is the primary method for constructing speleothem chronologies (Wendt et al., 2021). U-Th dating ($^{234}U/^{230}Th$) utilizes a portion of the U-series decay chain

($^{238}U \rightarrow {}^{234}U \rightarrow {}^{230}Th$). During speleothem formation, trace amounts of soluble uranium (UO_2^{2+}) are transported through the bedrock and are co-precipitated as a carbonate along with calcite (Dorale et al., 2004). The included ^{234}U undergoes alpha decay to the radioactive daughter isotope ^{230}Th. The comparatively short half-life of ^{230}Th (~75 kyrs vs 245 kyrs for ^{234}U) limits the $^{234}U/^{230}Th$ dating technique to ~7 half-lives of ^{230}Th, at which point the decay chain reaches secular equilibrium, a condition where all isotopes are decaying at the same rate. As a result, U-series dating methods can provide reliable age estimates for periods up to ~500,000 years (Cheng et al., 2013; Edwards et al., 1987).

U-series dating assumes that all ^{230}Th forms from radioactive decay after deposition. This is based on the behavior of Th, which is insoluble and is largely excluded from speleothem calcite (Richards & Dorale, 2003). However, speleothems are rarely completely devoid of initial thorium, meaning most U-series ages require a small correction for initial Th. This is done by measuring non-radiogenic ^{232}Th, an indicator of initial Th. When ^{232}Th is low, U-series ages are commonly corrected using the average ($^{230}Th/^{232}Th$) value, parentheses denote activity ratio, of the bulk earth (Hellstrom, 2006), though a wide range of initial values may be reasonable depending on the local geology. Samples with higher ^{232}Th are either not suitable for dating or necessitate more complex measurements of the cave environment (drip water, modern calcite, etc…) and/or isochron methods to estimate $^{230}Th/^{232}Th$ (Hellstrom, 2006).

1.3.3. Delta Notation (δ)

Several of the proxies discussed below (oxygen isotopes - $\delta^{18}O$, carbon isotopes - $\delta^{13}C$, uranium isotopes - $\delta^{234}U_{initial}$, and calcium isotopes - $\delta^{44}Ca$) are expressed by delta notation (δ) in units of per mil (‰), calculated by the following equation (example for $\delta^{18}O$):

$$\delta^{18}O = \left(\frac{(R^{sample} - R^{standard})}{R^{standard}} - 1\right) * 1000$$

Where R = O^{18}/O^{16} (Eq. 4)

1.3.4. Oxygen isotopes

Stable oxygen isotopes ($^{18}O/^{16}O$, $\delta^{18}O$), are the most utilized speleothem proxy. When precipitated under isotopic equilibrium, speleothem $\delta^{18}O$ values generally reflect a combination of drip water $\delta^{18}O$ and cave temperature (Lachniet, 2009), which is ultimately controlled by the temperature-dependent fractionation factor between water and calcite (Daëron et al., 2019; Hendy, 1971; Kim & O'Neil, 1997). In tropical regions, drip water $\delta^{18}O$ dominates speleothem $\delta^{18}O$ variability because temperature change is generally small (e.g. ~4 °C cooler during the Last Glacial Maximum), and the temperature effect on speleothem $\delta^{18}O$ is only -0.23 ‰ per 1 °C of warming (Kim & O'Neil, 1997). Using this relationship, temperature change since the Last Glacial Maximum would only change speleothem $\delta^{18}O$ by -1.15 ‰, a much smaller range than the 3-5 ‰ change exhibited by speleothem records of the Asian monsoon (Cheng et al., 2016). Thus, the $\delta^{18}O$ of precipitation ($\delta^{18}O_p$) falling above the cave is the primary driver of drip water $\delta^{18}O$, meaning tropical speleothem $\delta^{18}O$ variability generally tracks changes in $\delta^{18}O_p$. However, the interpretation of speleothem $\delta^{18}O$ in the Asian monsoon region is complex, as there are several controls on $\delta^{18}O_p$ such as rainfall amount, upstream rainout, moisture source, and seasonality (Cheng et al., 2009; Hu et al., 2008; Pausata et al., 2011; Tabor et al., 2018; Wang et al., 2001; Wolf et al., 2020; Yang et al., 2016). Regardless of the control, many speleothem records from the region interpret $\delta^{18}O$ as a qualitative measure of large-scale "monsoon intensity" or "monsoon strength", with more negative values indicating a stronger monsoon.

In MSEA, upstream rainout is the primary driver of summer monsoon $\delta^{18}O_p$ (Yang et al., 2016), meaning variations in $\delta^{18}O_p$ reflect change between the moisture source region and the cave site, resulting in an integrated signal of the Asian monsoon region. Increased rainfall (increased monsoon intensity) results in decreased $\delta^{18}O_p$ due to Rayleigh distillation (Pausata et al., 2011). Much less is known about the drivers of autumn monsoon $\delta^{18}O_p$. Importantly, local precipitation amount does not affect summer and autumn $\delta^{18}O_p$ in MSEA (Wolf et al., 2020), meaning mean annual $\delta^{18}O_p$ reflects large-scale changes in hydroclimate rather than local precipitation. The seasonal cycle of $\delta^{18}O_p$ in central Vietnam is similar to the rest of MSEA (Wolf et al., 2020), with more negative values in the summer months and more positive values in the winter months (Figure 1 in *Appendix A*). Since central Vietnam receives rainfall from the summer and autumn monsoons, the relative proportion of summer (lower $\delta^{18}O_p$) versus autumn rainfall (higher $\delta^{18}O_p$) is the primary control on mean annual $\delta^{18}O_p$ (Wolf et al., 2020). Ultimately, central Vietnam $\delta^{18}O_p$ could reflect variability from both monsoon systems.

Often overlooked, processes in the soil (evaporation), epikarst (karst hydrology), and cave (kinetic fractionation) may also affect speleothem $\delta^{18}O$ (Baker et al., 2019; Hendy, 1971; Mickler et al., 2006; Treble et al., 2022). This includes "prior calcite precipitation" (PCP), a well-known control on other speleothem proxies ($\delta^{13}C$, Mg/Ca, Sr/Ca, etc…). PCP occurs when CO_2 degasses (and calcite precipitates) from the drip water in the epikarst or on the cave ceiling (Johnson et al., 2006). This process causes heavier isotopes and certain elements (e.g. ^{18}O, ^{13}C, ^{44}Ca, Mg, and Sr) to be preferentially concentrated in the remaining drip water. The effects of PCP increase during drier conditions, when transport times are slow and less water is in the epikarst. Currently the effects of PCP on $\delta^{18}O$ have only been modeled and have yet to be observed in a speleothem record (Deininger et al., 2021; Skiba & Fohlmeister, 2023). Nevertheless, to avoid misinterpretation of speleothem $\delta^{18}O$, these potential controls should not be overlooked.

1.3.5. Carbon isotopes

Speleothem stable carbon isotopes ($^{13}C/^{12}C$, $\delta^{13}C$) are increasingly used to interpret past hydroclimate variability (Fohlmeister et al., 2020). Unlike speleothem $\delta^{18}O$, which generally reflects large-scale atmospheric processes, speleothem $\delta^{13}C$ values may reflect a variety of local climatic or environmental variables such as changes in C3:C4 vegetation (Dorale et al., 1998), atmospheric CO_2 concentration (Wong & Breecker, 2015), rate of soil respiration (Genty et al., 2003), the degree PCP along the drip water transport pathway (Johnson et al., 2006), open versus closed system dissolution (Hendy, 1971; Wood, 2019), and kinetic fractionation during CO_2 degassing (Frisia et al., 2011). Importantly, except for open versus closed dissolution, all of these processes affect speleothem $\delta^{13}C$ in the same direction, with higher $\delta^{13}C$ values occurring during drier conditions. When used in conjunction with multiple proxies and cave monitoring, speleothem $\delta^{13}C$ can provide a robust record of local hydroclimate.

1.3.6. Trace elements

Compared to stable isotopes, trace elements (reported as X/Ca ratios) are a newer speleothem geochemical proxy. Like $\delta^{13}C$, trace elements are used as a tracer of local hydrology. While there are many different trace elements measured in speleothems (Mg, Sr, Ba, Y, Cu, Pb, Fe, U, Ni, etc…), which have a variety of controls (Fairchild & Treble, 2009), here I focus on Mg and Sr, the two trace element proxies reported in this dissertation. The Mg and Sr in speleothems is sourced from the bedrock or overlying soil and are substituted for Ca during calcite precipitation (Fairchild et al., 2000). PCP is a major driver of both elements, where higher degrees of PCP during dry conditions concentrate Mg and Sr in the drip water, ultimately increasing Mg/Ca and Sr/Ca in the speleothem (Johnson et al., 2006). The temperature-dependent partition coefficient of the element (D_x) (see Day and Henderson (2013) and Wassenburg et al. (2020)) dictates this process, where elements with $D_x < 1$ (Mg and Sr) are preferentially excluded during calcite precipitation, causing Mg/Ca and Sr/Ca to increase in drip waters during PCP. Non-hydroclimate factors also affect speleothem Mg/Ca and Sr/Ca. Temperature is a known control on the Mg/Ca of precipitated calcite (Day & Henderson, 2013; Huang & Fairchild, 2001; Wassenburg et al., 2020), however, the hydrological signal often overprints this effect (Johnson et al., 2006). Speleothem Sr/Ca shows a less clear dependence on precipitation rate when growth rate is high (Gabitov et al., 2014). Because of the various controls on Mg/Ca and Sr/Ca, cave monitoring is important for trace element interpretation and records are often complemented by a multiproxy approach with $\delta^{13}C$ values (Griffiths et al., 2020; Patterson et al., 2023; Wright et al., 2022).

1.3.7. Uranium isotopes ($\delta^{234}U_{initial}$)

Speleothem uranium isotopes ($(^{234}U/^{238}U)_{initial}$, often reported as $\delta^{234}U_{initial}$, are a hydroclimate proxy measured in the course of U-series dating. While not commonly used as the primary proxy in a speleothem record, $\delta^{234}U$ measurements provide an important complement to other speleothem hydroclimate proxies. This is because speleothem $\delta^{234}U_{initial}$ is unaffected by PCP, making it an independent measure of hydroclimate variability. Instead, water-rock interaction and weathering control speleothem $\delta^{234}U_{initial}$ (Cross et al., 2015; Wendt et al., 2020). ^{234}U is produced by alpha decay of ^{238}U via two short-lived intermediate daughter isotopes, and ejected directly into solution or leached from damaged crystal lattice sites in the bedrock, reflecting weathering (Fleischer & Raabe, 1978; Ivanovich, 1982; McGee et al., 2012). During dry periods, slower infiltration rates elevate $(^{234}U/^{238}U)_{initial}$, due to increased water-rock interaction times and/or the accumulation of ^{234}U in the epikarst (Cross et al., 2015; Hellstrom & McCulloch, 2000; Maher et al., 2006). Similarities between $\delta^{234}U_{initial}$ and other proxies controlled by PCP confirm that variations in the speleothem record reflect hydroclimate rather than within-cave processes.

1.3.8. Calcium isotopes

Calcium isotopes ($^{44}Ca/^{42}Ca$, $\delta^{44}Ca$) are a promising new speleothem proxy because of their potential to provide semi-quantitative estimates of local rainfall amount (Johnson, 2021). All current speleothem hydroclimate proxies, including the ones used in this dissertation ($\delta^{18}O$, $\delta^{13}C$, Mg/Ca, Sr/Ca, and $\delta^{234}U_{initial}$), only provide qualitative measurements of hydroclimate (e.g. “wetter” or “drier”). While qualitative measurements are useful, quantifying rainfall amount would substantially improve the utility of a speleothem hydroclimate record. Thus, speleothem δ^{44}Ca records are an important advancement in speleothem science.

Using δ^{44}Ca as a hydroclimate proxy relies on the assumption that PCP is the primary driver of speleothem δ^{44}Ca variability. However, other climate and environmental factors such as growth rate (Lemarchand et al., 2004; Reynard et al., 2011; Tang et al., 2008), temperature (Tang et al., 2008), and bedrock dissolution (de Wet et al., 2021) may impact speleothem δ^{44}Ca values. Importantly, none of these controls are particularly strong, with most studies identifying PCP as the primary control on their speleothem δ^{44}Ca record (Li et al., 2018; Magiera et al., 2019; Owen et al., 2016; Stoll et al., 2022; de Wet et al., 2021). Owen et al. (2016) developed a novel method to reconstruct local rainfall from speleothem δ^{44}Ca. The method first quantifies PCP amount using established geochemical relationships and modern δ^{44}Ca measurements of the cave environment (bedrock, modern calcite, drip water). Then assuming a linear relationship between PCP amount and rainfall, rainfall amount is derived from PCP amount using local rainfall data. Due to the remaining uncertainties surrounding δ^{44}Ca systematics and the relationship between PCP and rainfall, this study and all subsequent studies utilizing this approach (Li et al., 2018; Magiera et al., 2019; de Wet et al., 2021), refer to these reconstructions as semi-quantitative rather than quantitative. Nevertheless, calcium isotopes provide an important step towards estimating quantitative rainfall change from speleothems.

1.3.9. Summary of geochemical proxies

In this dissertation I utilize the methods and proxies described above on stalagmite HH-1 to investigate the Southeast Asian autumn monsoon and central Vietnam hydroclimate over the last 45,000 years (Table 1.1). My results from HH-1 are the first long record (> 10,000 years) from Vietnam and one of the longest from anywhere in MSEA. In Chapter 2, I use U-series dating to construct an age model and measurements of $\delta^{13}C$, trace elements, and $\delta^{234}U_{initial}$, to reconstruct qualitative local hydroclimate change. In Chapter 3, I generate a semi-quantitative record of rainfall change using $\delta^{44}Ca$ measurements. In Chapter 4, I explore the effects of PCP on the HH-1 $\delta^{18}O$ record. This dissertation demonstrates how one speleothem sample can generate a multi-faceted record of past hydroclimate change. See further details in section 1.5.

Table 1.1. Summary of speleothem proxies and their drivers.

Proxy	Drivers (**BOLD** = dominant in HH-1 record)	Climate conditions indicated by increased values (for dominant drivers only)
$\delta^{18}O$	**$\delta^{18}O_p$**, temperature, **PCP**	Decreased upstream rainout and/or change in seasonality ($\delta^{18}O_p$), drier local hydroclimate (PCP)
$\delta^{13}C$	**PCP,** C3 versus C4 vegetation, atmospheric CO_2, soil respiration, open versus closed system dissolution	drier local hydroclimate
Trace elements (Mg/Ca & Sr/Ca)	**PCP**, **growth rate (Sr only)**, temperature (Mg only)	drier local hydroclimate (PCP), faster growth (growth rate)
$\delta^{234}U_{initial}$	Water-rock interaction, weathering (dominant driver unknown)	drier local hydroclimate
$\delta^{44}Ca$	**PCP**, growth rate, temperature, bedrock dissolution	drier local hydroclimate

1.4. Research Objectives

My dissertation uses a speleothem from central Vietnam to investigate the following research questions:

1. What are the dominant drivers of Southeast Asian autumn monsoon variability over the last 45,000 years on millennial to orbital timescales? (Chapter 2)
2. How much did rainfall amount change in central Vietnam over the last 45,000 years? (Chapter 3)
3. Does prior calcite precipitation (PCP) affect speleothem oxygen isotopes ($\delta^{18}O$)? Can the PCP signal be removed from a speleothem $\delta^{18}O$ record? (Chapter 4)

1.5. Outline of Chapters

Chapter 2: Glacial changes in sea level modulated millennial-scale variability of Southeast Asian autumn monsoon rainfall

In Chapter 2 I use a new multi-proxy record from stalagmite HH-1 to reconstruct Southeast Asian autumn monsoon variability over the last 45,000 years. The record shows that autumn rainfall in central Vietnam underwent substantial and abrupt change on millennial-to-orbital timescales. To support my findings from the HH-1 record, I show that climate models simulate similar autumn rainfall change in central Vietnam. Using climate model simulations, I identify sea level, more specifically the inundation or exposure of the Gulf of Tonkin and the South China Shelf, as the primary driver of Southeast Asian autumn monsoon rainfall on millennial-to-orbital timescales. This previously unknown control on the Southeast Asian autumn monsoon causes wet conditions during high sea level (inundated land) and dry conditions during low sea level (exposed land). My work is the first paleorecord of Southeast Asian autumn monsoon rainfall spanning the Late Pleistocene-Holocene, addressing an important gap in our understanding of hydroclimate in MSEA.

Chapter 3: A semi-quantitative estimate of Late Pleistocene sea-level-driven rainfall change in central Vietnam

The hydroclimate record presented in Chapter 2 is qualitative, and thus cannot quantify rainfall change in central Vietnam. In Chapter 3, I present a semi-quantitative reconstruction of rainfall from central Vietnam using calcium isotope measurements (δ^{44}Ca) from stalagmite HH-1. After demonstrating that PCP is the dominant control on HH-1 δ^{44}Ca, I first derive PCP amount and then convert PCP amount to rainfall. My reconstruction shows that rainfall may have been 50 % lower than modern levels during the sea-level lowstand in the Last Glacial Maximum (~20 ka). I then compare this estimate to climate model simulations which show similar, but somewhat weaker, rainfall reductions of 25 – 35 %. While significant uncertainty with the δ^{44}Ca-rainfall calibration remains, my work demonstrates an important advancement towards quantifying past rainfall change in MSEA.

Chapter 4: Exploring and removing the influence of prior calcite precipitation on speleothem oxygen isotopes in Southeast Asia

In Chapter 4, I investigate the influence of PCP on the HH-1 oxygen isotope record ($\delta^{18}O$). Through multiproxy comparison, I demonstrate that PCP, rather than rainfall $\delta^{18}O$ (the expected driver of HH-1 $\delta^{18}O$), primarily drives HH-1 $\delta^{18}O$ variability. I then utilize a new method, which uses the HH-1 Mg/Ca record, cave monitoring data, a geochemical model built on established geochemical relationships, to remove the PCP signal from the HH-1 $\delta^{18}O$ record. Once corrected, HH-1 $\delta^{18}O$ better agrees with regional speleothem $\delta^{18}O$ records and climate model output of precipitation $\delta^{18}O$. These results reveal that once the influence of PCP is removed, HH-1 $\delta^{18}O$ does record regional $\delta^{18}O$ rainfall variability. This work demonstrates that PCP, a previously debated control on speleothem $\delta^{18}O$, can overprint the rainfall $\delta^{18}O$ signal in speleothem $\delta^{18}O$ records. While PCP is unlikely to affect most speleothem $\delta^{18}O$ records, my findings have important implications for the field of speleothem science by demonstrating the PCP must be considered a potential driver of speleothem $\delta^{18}O$ to avoid misinterpretation of the proxy record.

Summary

The collective results of my dissertation improve our understanding of hydroclimate change in MSEA. More specifically, my work sheds light on the past variability of the Southeast Asian autumn monsoon. My interest in the Southeast Asian autumn monsoon is motivated by the absence of long paleorecords in central Vietnam and the high vulnerability those living in the region face from changes in autumn monsoon rainfall. Furthermore, I use innovative geochemical techniques that not only generate a nuanced analysis of central Vietnam hydroclimate, but have potentially far-reaching implications for the field of speleothem science.

APPENDIX A

Monitoring data from Phong Nha-Ke Bang and Hoa Huong cave

1. Phong Nha rainfall $\delta^{18}O_p$

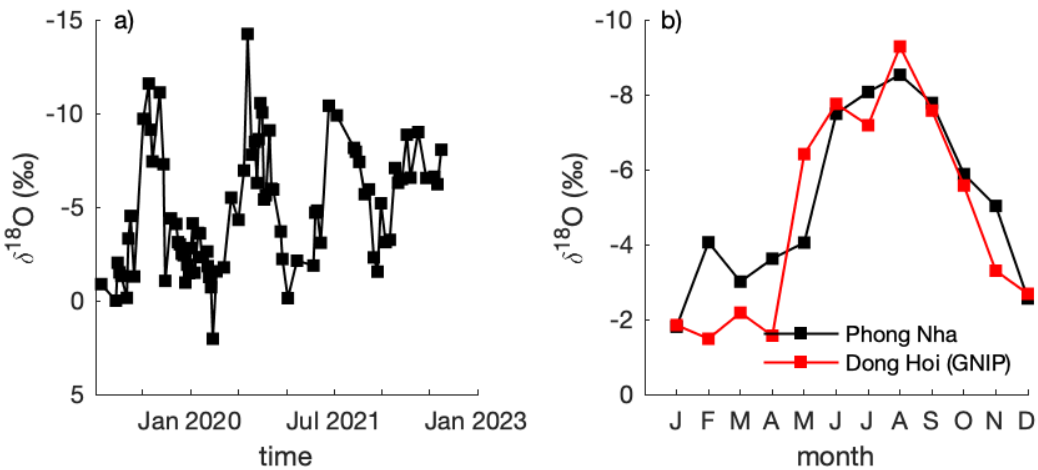

Figure 1. Precipitation oxygen isotopes ($\delta^{18}O_p$, VSMOW) results from Phong Nha. a) $\delta^{18}O_p$ time series of all precipitation samples collected at Phong Nha-Ke Bang National Park headquarters from January 2019-August 2022. b) Average $\delta^{18}O_p$ seasonal cycle of Phong Nha (black) compared to Dong Hoi (red; data from GNIP database - https://www.iaea.org/services/networks/gnip).

Table 1. $\delta^{18}O_p$ and δD data from Phong Nha-Ke Bang National Park headquarters

Date (m/d/yr)	$\delta^{18}O_p$ (‰)	δD (‰)
1/23/19	-0.88	5.32
3/20/19	0.00	7.49
3/27/19	-2.03	-4.99
4/3/19	-1.51	-2.80
4/10/19	-1.31	0.37
5/1/19	-0.15	5.56
5/7/19	-3.32	-16.68
5/15/19	-4.53	-25.12
5/29/19	-1.30	0.97
7/3/19	-9.71	-67.72
7/24/19	-11.59	-85.02
7/31/19	-9.12	-71.33
8/7/19	-7.43	-55.27
9/4/19	-11.12	-78.44
9/18/19	-7.29	-50.13
9/25/19	-1.06	7.13
10/17/19	-4.39	-16.39
11/6/19	-4.10	-13.70
11/13/19	-3.13	-7.63
11/20/19	-3.01	-7.53
11/27/19	-2.51	-4.47
12/4/19	-2.42	-3.81
12/11/19	-0.97	7.26
12/18/19	-1.92	-5.56
12/25/19	-1.47	-2.20
1/1/20	-2.81	-10.39
1/8/20	-4.13	-19.86
1/15/20	-1.49	-0.72
1/29/20	-3.62	-7.01

Date (m/d/yr)	$\delta^{18}O_p$ (‰)	δD (‰)
2/5/20	-3.59	-6.68
2/12/20	-2.33	-1.30
3/4/20	-2.62	-7.45
3/6/20	-1.84	-2.00
3/11/20	-1.27	18.87
3/18/20	-0.72	22.01
3/25/20	2.03	33.48
4/8/20	-1.57	18.94
5/6/20	-1.78	16.07
6/3/20	-5.50	-17.63
7/1/20	-4.32	-19.04
7/22/20	-6.95	-27.43
8/5/20	-14.24	-87.32
8/21/20	-7.79	-38.18
9/2/20	-8.48	-44.83
9/10/20	-6.28	-24.94
9/16/20	-8.63	-25.40
9/23/20	-10.55	-48.04
9/30/20	-10.04	-50.73
10/7/20	-5.40	-7.71
10/14/20	-5.63	-10.39
10/28/20	-9.10	-44.20
11/4/20	-5.98	-18.59
11/11/20	-5.94	-19.40
12/10/20	-3.70	-9.65
12/16/20	-2.22	-1.06
1/6/21	-0.14	14.58
2/10/21	-2.13	4.09
4/14/21	-1.88	4.12

Date (m/d/yr)	$\delta^{18}O_p$ (‰)	δD (‰)
4/28/21	-4.80	-17.12
5/12/21	-3.10	-17.88
6/12/21	-10.41	-10.82
7/12/21	-9.89	-69.30
9/16/21	-8.16	-69.44
9/23/21	-7.95	-56.11
10/6/21	-7.41	-56.30
10/27/21	-5.68	-43.56
11/12/21	-5.94	-30.19
12/1/21	-2.31	-30.88
12/15/21	-1.55	-1.55
12/28/21	-5.20	-25.58
1/15/22	-3.12	-11.11
1/31/22	-3.25	-11.29
2/20/22	-7.08	-45.68
3/4/22	-6.30	-38.63
3/18/22	-6.49	-39.19
4/6/22	-8.86	-62.21
4/20/22	-6.56	-39.45
5/20/22	-9.00	-62.19
6/20/22	-6.55	-39.54
7/20/22	-6.61	-38.98
8/1/22	-6.22	-40.00
8/16/22	-8.06	-53.16

Mean standard deviation for $\delta^{18}O$ and δD is 0.06 ‰ and 0.12 ‰, respectively. Values reported in VSMOW.

2. Hoa Huong cave

Cave monitoring at Hoa Huong cave is ongoing. The data presented here were collected from March 2020 – March 2023 and are primarily from three field expeditions in March 2020, August 2022, and March 2023. A summary of each field expedition is below.

March 4th, 2020

- Left a HOBO data logger near Drip Site 1 to record cave temperature (Figure 3)
- Collected drip water (Figure 4, Table 3) and recorded measurements of cave environment (Table 2)
- Left a Stalagmate at Drip Site 1 to record drip rate (Figure 5)
- Collected stalagmite HH-1

August 8th, 2022

- Collected drip water and recorded measurements of cave environment
- Swapped the in cave HOBO data logger, left an aboveground HOBO data logger
- Swapped the Stalagmate at Drip Site 1

March 7th, 2023

- Collected drip water and recorded measurements of cave environment
- Swapped the aboveground HOBO data logger, left a new HOBO data logger near Drip Site 2
- Swapped the Stalagmate at Drip Site 1
- Left a Vaisala $_pCO_2$ monitor

2.1 Sampling locations

<u>Drip Site 1:</u> Drip Site 1 is located ~60 m from the cave entrance (Figure 2). Most measurements of cave environment (Table 2) were recorded at or near Drip Site 1. This includes cave temperature (Figure 3) and drip rate (Figure 5).
<u>Drip Site 2 and HH-1 sample location:</u> HH-1 was collected ~100 m from the cave entrance (Figure 2). There is no active drip at or near the HH-1 collected site. The Vaisala $_pCO_2$ probe was placed on a ledge above the HH-1 sample location. Drip Site 2 is ~10 m deeper into the cave from HH-1. Only one drip water measurement is currently available from Drip Site 2. However, the site is the target of future monitoring efforts.

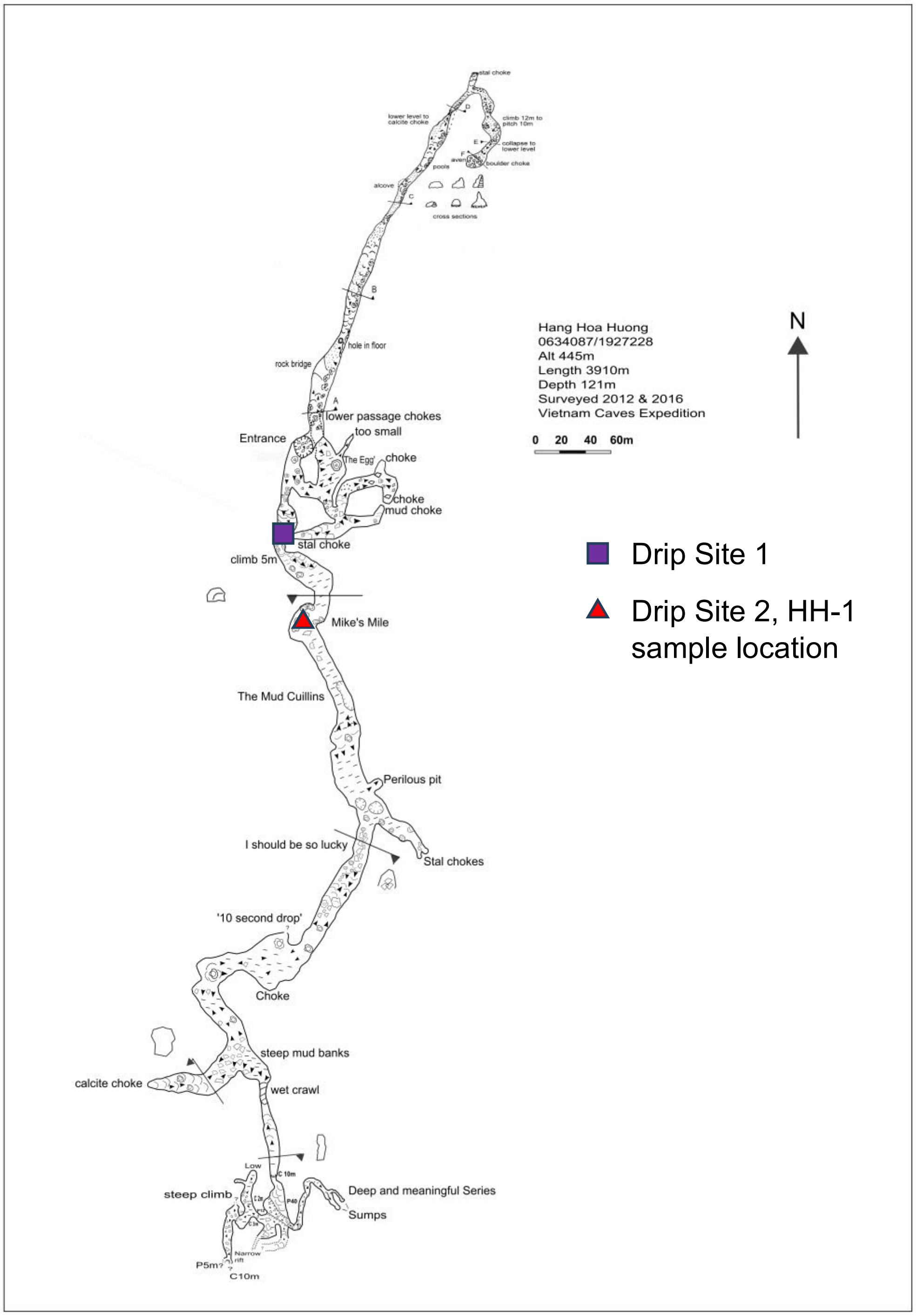

Figure 2. Map of Hoa Huong cave with approximate locations of Drip Site 1 (purple square) and Drip Site 2 and HH-1 sample location (red triangle).

2.2 Cave environment

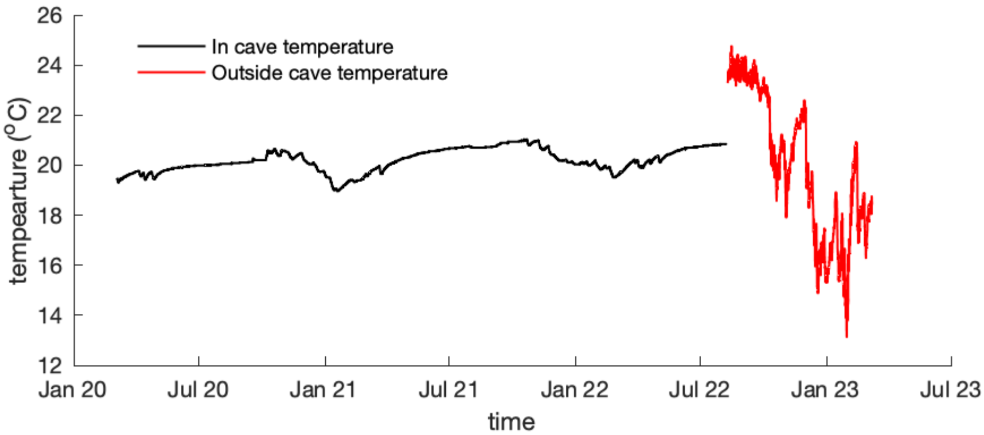

Figure 3. Time series of cave temperature (black, March 2020 – August 2022) and aboveground temperature (red, August 2022 – March 2023). The aboveground temperature was recorded within several hundred meters of the entrance of Hoa Huong cave in a rock shelter.

Table 2. Measurements of Hoa Huong cave environment at or near Drip Site 1.

Measurement	March 2020	August 2022	March 2023
Air temp (°C)	19.5, 18.4 (rock)	19.9-20.2	19.6
Relative humidity (%)	86.1 (unreliable)	99	92
Cave air pCO_2 (ppm)	820	3120	510
Drip water temp (°C)	NA	20.0	NA
Drip water pH	8.4 (unreliable)	7.93	8.38
Drip water alkalinity (ppm)	168	175	148

2.3 Drip water monitoring

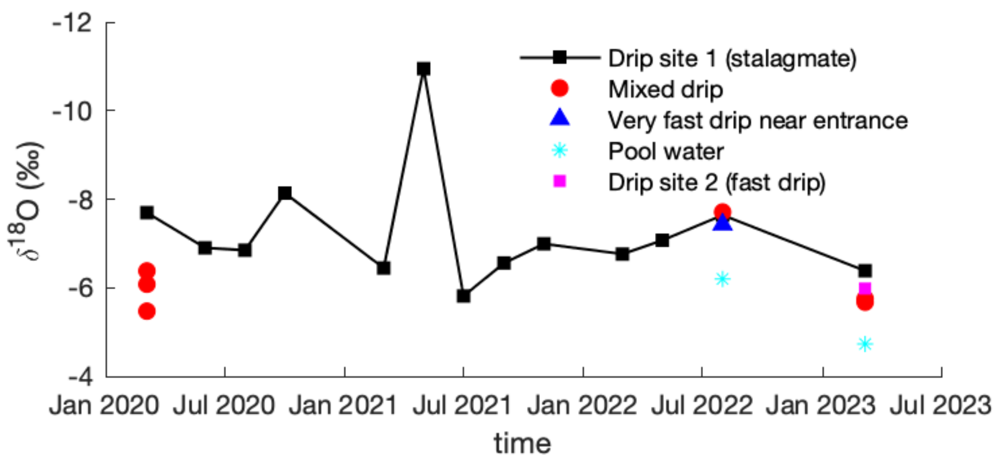

Figure 4. Drip water measurements from Hoa Huong cave. Black squares show a time series curve of 12 drip water samples taken from Drip Site 1 from March 2020 – March 2023. Red circles are mixed drips (water collected from multiple drips), cyan asterisks are

water collected from the pool near Drip Site 1, blue triangles are from a very fast drip near the cave entrance, and magenta squares are from Drip Site 2.

Table 3. Drip water $\delta^{18}O$ from Hoa Huong cave

Sample location/type	Date (m/d/yr or m/yr)	$\delta^{18}O_p$ (‰, VSMOW)	δD (‰)
Drip site 1	3/4/20	-7.70	-46.67
Mixed drip (DS 1)	3/4/20	-6.38	-35.69
Mixed drip (DS 1)	3/4/20	-6.08	-32.93
Mixed drip (DS 1)	3/4/20	-5.47	-28.26
Drip site 1	6/20	-6.90	-40.73
Drip site 1	8/20	-6.85	-40.40
Drip site 1	10/20	-8.14	-53.66
Drip site 1	3/21	-6.45	-36.85
Drip site 1	5/21	-10.95	-77.14
Drip site 1	7/21	-5.81	-33.84
Drip site 1	9/21	-6.56	-40.48
Drip site 1	11/21	-6.99	-47.18
Drip site 1	3/21	-6.76	-41.07
Drip site 1	5/21	-7.07	-43.97
Drip site 1	8/22/22	-7.64	-55.71
HH Mix	8/22/22	-7.71	-54.72
Fast drip near entrance	8/22/22	-7.43	-53.78
Pool	8/22/22	-6.20	-51.39
Drip site 1	3/7/23	-6.38	-36.8
Mixed drip (DS 1)	3/7/23	-5.67	-30.9
Drip site 2	3/7/23	-5.98	-32.8
Mixed drip (DS 2)	3/7/23	-5.75	-31.2
Pool	3/7/23	-4.73	-22.6

Mean standard deviation for $\delta^{18}O$ and δD is 0.06 ‰ and 0.12 ‰, respectively. Values reported in VSMOW.

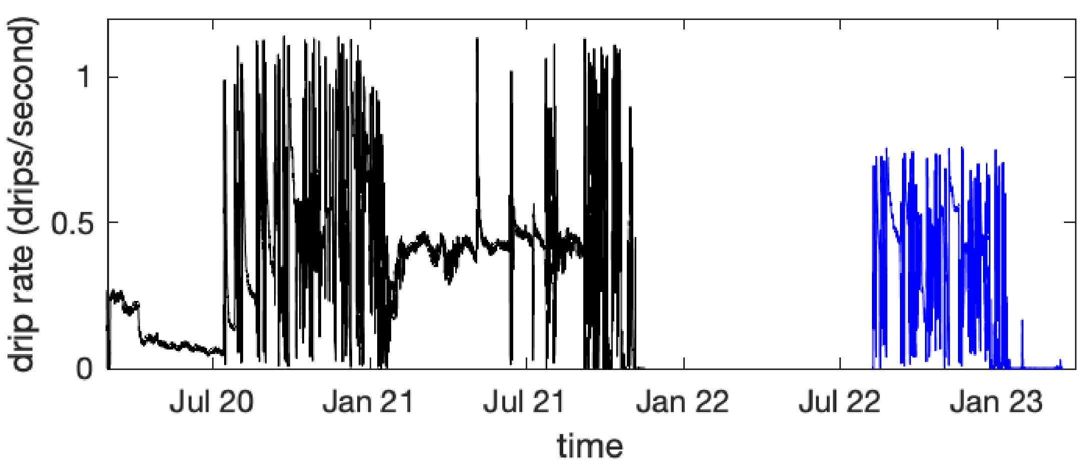

Figure 5. Drip rate time series from Drip Site 1.

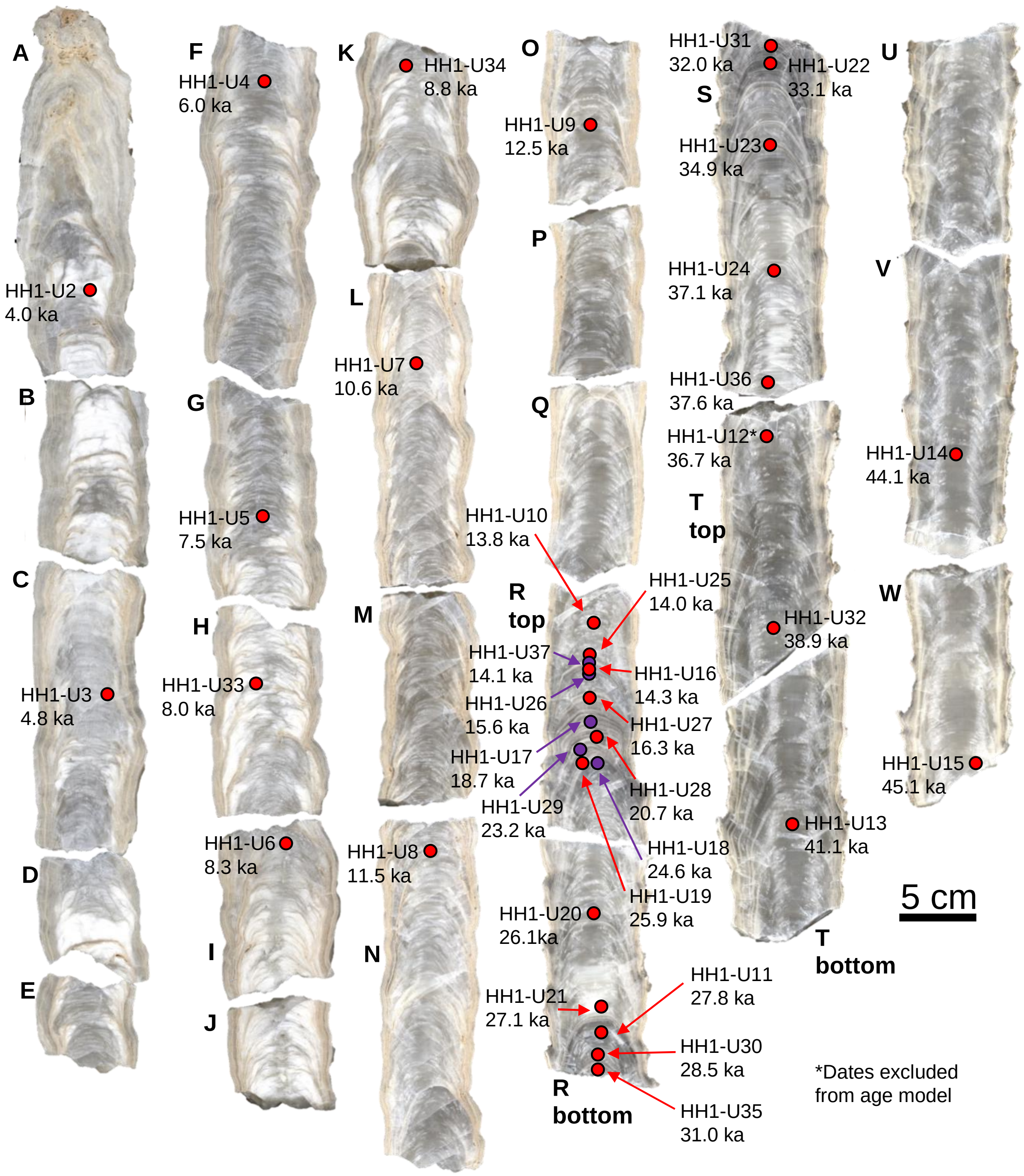

Figure 6. Scans of stalagmite HH-1 with U-Th dates labeled.

CHAPTER 2: Glacial changes in sea level modulated millennial-scale variability of Southeast Asian autumn monsoon rainfall

Adapted from:

Patterson, E.W., K.R. Johnson, M.L. Griffiths, C.W. Kinsley, D. McGee, X. Du, T. Pico, A. Wolf, V. Ersek, R. Mortlock, K.A. Yamoah, T.N. Bui, M.X. Tran, Q. Do-Trong, T.V. Vo, and T.H. Dinh, 2023. Glacial changes in sea level modulated millennial-scale variability of Southeast Asian autumn monsoon rainfall. *Proceedings of the National Academy of Sciences*, *120*(27), p.e2219489120.

Supporting information located in Appendix B.

2.1. Abstract

Most paleoclimate studies of Mainland Southeast Asia hydroclimate focus on the summer monsoon, with few studies investigating rainfall in other seasons. Here we present a multiproxy stalagmite record (45,000 – 4,000 years) from central Vietnam, a region that receives most of its annual rainfall in autumn (September-November). We find evidence of a prolonged dry period spanning the last glacial maximum that is punctuated by an abrupt shift to wetter conditions during the deglaciation at ~14 ka. Paired with climate model simulations, we show that sea level change drives autumn monsoon rainfall variability on glacial-orbital timescales. Consistent with the dry signal in the stalagmite record, climate model simulations reveal that lower glacial sea level exposes land in the Gulf of Tonkin and along the South China Shelf, reducing convection and moisture delivery to central Vietnam. When sea level rises and these landmasses flood at ~14 ka, moisture delivery to central Vietnam increases causing an abrupt shift from dry to wet conditions. On millennial timescales, we find signatures of well-known Heinrich Stadials (dry conditions) and Dansgaard-Oeschger Events (wet conditions). Model simulations show that during the dry

Heinrich Stadials, changes in sea surface temperature related to meltwater forcing cause the formation of an anomalous anticyclone in the Western Pacific, which advects dry air across central Vietnam decreasing autumn rainfall. Notably, sea level modulates the magnitude of millennial-scale dry and wet phases by muting dry events and enhancing wet events during periods of low sea level, highlighting the importance of this mechanism to autumn monsoon variability.

2.2. Introduction

The seasonal rains of the Southeast Asian monsoon affect over 650 million people. Relatively small fluctuations in rainfall cause flooding events and prolonged droughts, phenomena that have been affecting the people of Mainland Southeast Asia (MSEA – Vietnam, Laos, Cambodia, Thailand, Myanmar, and Peninsular Malaysia) for millennia (Buckley et al., 2010; Chawchai et al., 2020; Griffiths et al., 2020). Paleoclimate records not only reveal these fluctuations in the Southeast Asian monsoon, but also help constrain the dominant drivers of hydroclimate over a range of timescales (Buckley et al., 2010; Chawchai et al., 2020; Griffiths et al., 2020; Wang et al., 2019; Yamoah et al., 2016). Yet, with few paleorecords from MSEA, the hydroclimate variability of the region remains poorly constrained. Extending the MSEA paleorecord back into the Late Pleistocene will reveal how the regional hydroclimate responded to climate forcings and feedbacks during periods of rapid global change, such as events associated with the last glacial period and deglaciation (e.g., Heinrich Stadials (HS) and Dansgaard-Oeschger (DO) Events). Additionally, ice volume driven sea level change impacted MSEA hydroclimate during this time. For example, the relative exposure or inundation of the Sunda and Sahul shelves influenced hydroclimate patterns across MSEA via changes in deep convection in the tropical Indo-Pacific and the resulting reorganization of the Walker Circulation (Di Nezio et al., 2016; DiNezio & Tierney, 2013; Hällberg et al., 2022; Pico et al., 2020; Yamoah et al., 2021).We know far less about the effects of land exposure change in northeast MSEA and South China. Even though these landmasses are much smaller than the Sunda and Sahul shelves, their proximal location to MSEA could cause substantial local hydroclimate change. Ultimately, new paleorecords from MSEA serve as crucial benchmarks to test whether the climate models we use to project future climate accurately capture changes in MSEA hydroclimate after large perturbations in external forcings.

The Southeast Asian monsoon, a part of the greater Asian monsoon system, is comprised of two main components, the southwest (SW) monsoon (May-August) with moisture sourced from the Indian Ocean and Bay of Bengal, and the northeast (NE) monsoon (September-April) with moisture sourced from the South China Sea (Figure S1a,b, S2)(Wolf et al., 2020). In contrast to most of MSEA, which receives the majority of its annual rainfall from the SW monsoon during the summer months (July-August; Figure S1c), much of the eastern coast of Vietnam receives a large proportion of its annual rainfall from the NE monsoon during autumn (September-November; Figure S1d); from here on we refer to this as the Southeast Asian autumn monsoon. While not a common rainfall pattern in the region, the Southeast Asian autumn monsoon is part of the a global network of autumn monsoon regions, which occur along the eastern coasts of some landmasses in the tropics (He et al., 2021; Ramesh et al., 2021). During the autumn monsoon, the Truong Son Mountains, a N-S trending mountain range along the Vietnam-Laos border, cause orographic uplift of the NE monsoon winds, which concentrates rainfall on the eastern side of the mountains (Sengupta & Nigam, 2019). This phenomenon co-occurs with the tropical cyclone season, resulting in strong rainfall events that can lead to catastrophic flooding in central Vietnam (Luu et al., 2020), the most recent occurring in October 2020 (Luu et al., 2021). While the summer and winter monsoons across Asia have been researched extensively (Cheng et al., 2016; Goldsmith et al., 2017; Sun et al., 2011; Wen et al., 2016; Yancheva et al., 2007; Zhang et al., 2018), the limited instrumental records, climate model analyses, and paleoclimate records of autumn hydroclimate leave this important component of the Southeast Asian monsoon severely understudied (Ramesh et al., 2021; Sengupta & Nigam, 2019; Wolf et al., 2020).

Here we present an autumn monsoon rainfall record from MSEA spanning 45-4 ka. We use a multiproxy stalagmite record from central Vietnam to show that the autumn monsoon underwent significant change over the last 45,000 years. Paired with climate model simulations, we find that glacially modulated sea level, a previously unknown control on MSEA hydroclimate, is a dominant driver of autumn monsoon rainfall variability on millennial-orbital timescales.

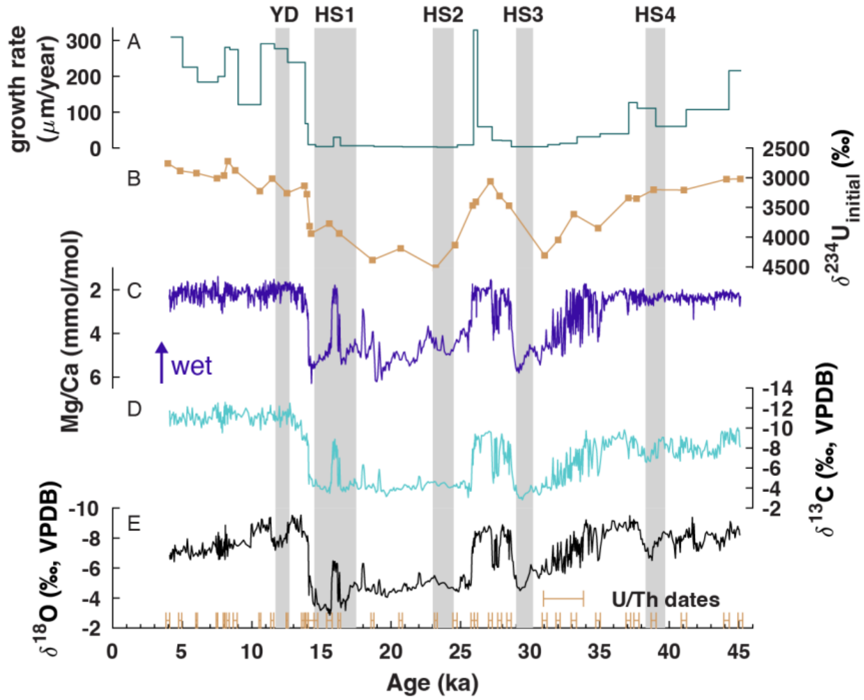

Figure 2.1. Time series of HH-1 proxies. Speleothem a) growth rate (green), b) $\delta^{234}U_{initial}$ (tan), c) Mg/Ca (blue), d) $\delta^{13}C$ (turquoise), and e) $\delta^{18}O$ (black) and 2σ error bars of U/Th ages (tan) from 4-45 ka. Gray shading denotes Heinrich Stadials 1-4 (HS) and the Younger Dryas (YD).

2.3. Results and Discussion

2.3.1. Autumn monsoon rainfall variability inferred from a central Vietnam stalagmite

For this study, we use a previously broken 3.7 m long stalagmite, HH-1 (Figure S3a), collected from Hoa Huong cave, a hydrologically active cave in Phong Nha-Ke Bang National Park in central Vietnam (17.5°N, 106.2°E; Elev. 411 m; See *SI Appendix*). Unlike the majority of MSEA, which primarily receives rainfall during the summer (JJA), from 1951-2007 our study site in central Vietnam received nearly half of its annual rainfall (~47%) during the autumn monsoon (SON) and only ~30% during JJA (Figure S1c,d) (Yatagai et al., 2012). The HH-1 age model was constrained in time with 35 U-Th dates (see *Methods*; Figure S3c,

Table S1) and shows that it grew continuously between 45.1 and 4.0 ka, but at a highly variable growth rate (Figure 2.1a). The fastest rates occur after the deglaciation (120-329 μm/yr), while the slowest rates occur during Heinrich Stadials 1-3 and the Last Glacial Maximum (LGM, ~20 ka; 2-10 μm/yr; Figure 2.1a). The HH-1 record consists of 768 carbon ($\delta^{13}C$) and oxygen ($\delta^{18}O$) stable isotope analyses and 1,384 Mg/Ca analyses, resulting in an average resolution of ~50 years and ~30 years, respectively (Figure 2.1c-e, see *Methods*).

Similar to many studies (Cross et al., 2015; Griffiths et al., 2020; Wright et al., 2022), we interpret speleothem $\delta^{13}C$ and Mg/Ca as tracers of local hydroclimate. The remarkable synchronicity of HH-1 $\delta^{13}C$ and Mg/Ca records suggests a common control (Figure 2.1), which we propose to be prior calcite precipitation (PCP). PCP is caused by CO_2 degassing in the epikarst and within the cave and affects both speleothem $\delta^{13}C$ and Mg/Ca (Johnson et al., 2006). During PCP, lighter isotopes (^{12}C) and calcium are preferentially removed from solution leaving the remaining dripwater, and in turn speleothem carbonate, enriched in heavier isotopes (^{13}C) and trace elements (Mg). Generally, periods of high PCP (high $\delta^{13}C$ and Mg/Ca) reflect dry conditions and periods of low PCP (low $\delta^{13}C$ and Mg/Ca) reflect wet conditions (Griffiths et al., 2020). In addition to PCP, there are several other known controls on speleothem $\delta^{13}C$ such as vegetation type, soil respiration rate, atmospheric CO_2 concentration, and open vs closed system dissolution (Fohlmeister et al., 2020; Genty et al., 2003; Hendy, 1971; Wong & Breecker, 2015), which are difficult to deconvolve without multiproxy analyses. We point to the covariation between HH-1 $\delta^{13}C$ and Mg/Ca ($r = 0.89$, $p < 0.01$), a robust indicator of PCP (Cross et al., 2015; Griffiths et al., 2020; Wright et al., 2022), as further evidence that PCP is likely the dominant control on both proxies. HH-1 Sr/Ca, a proxy also affected by PCP (Cross et al., 2015), also shows similarities with the

Mg/Ca record (Figure S4). However, the records are antiphased, opposite to the expected in phase relationship between Mg/Ca and Sr/Ca (Johnson et al., 2006), suggesting that PCP does not drive HH-1 Sr/Ca. Due to the similarities between HH-1 Sr/Ca and growth rate (Figure S4), another known control on speleothem Sr/Ca (Gabitov et al., 2014), we propose that growth rate dominates HH-1 Sr/Ca. Because it is challenging to interpret climate from growth rate changes of a single stalagmite, we choose to focus our analyses on the PCP-driven Mg/Ca and $\delta^{13}C$ records.

We use speleothem $\delta^{234}U_{initial}$ values from our 35 U-series measurements to provide an independent measure of hydroclimate that is not affected by PCP but rather water-rock interaction and weathering (Cross et al., 2015; Wendt et al., 2020). ^{234}U, produced by alpha decay of ^{238}U via two short-lived intermediate daughter isotopes, may be directly ejected into solution during decay or more easily leached from radiation damaged crystal lattice sites (i.e. alpha recoil), causing most natural water samples to deviate from secular equilibrium and exhibit a ($^{234}U/^{238}U$) activity ratio greater than 1 (Fleischer & Raabe, 1978; Ivanovich, 1982; McGee et al., 2012). During dry periods, slower infiltration rates may further elevate ($^{234}U/^{238}U$), increasing $\delta^{234}U_{initial}$ in infiltrating water due to increased water-rock interaction times and/or accumulation and subsequent flushing of ^{234}U in the epikarst (Cross et al., 2015; Hellstrom & McCulloch, 2000; Maher et al., 2006). During wet periods, increased bedrock dissolution and/or faster infiltration may lead to lower $\delta^{234}U_{initial}$. The covariation between the $\delta^{234}U_{initial}$ and the $\delta^{13}C$ and Mg/Ca records serves as additional evidence for our use of $\delta^{13}C$ and Mg/Ca as hydroclimate proxies (Figure 2.1). The similarities between these three proxies ($\delta^{13}C$, Mg/Ca, and $\delta^{234}U_{initial}$) indicates that hydroclimate, rather than in cave processes, control PCP and thus the $\delta^{13}C$ and Mg/Ca signals.

As with other speleothem records from low latitude regions, we expect HH-1 $\delta^{18}O$ to primarily reflect variations in precipitation $\delta^{18}O$ ($\delta^{18}O_p$). For most of MSEA, the main control on interannual to orbital-scale $\delta^{18}O_p$ variability is upstream rainout during the summer monsoon, an indicator of large-scale summer monsoon intensity (Pausata et al., 2011; Yang et al., 2016). Despite the different rainfall seasonality in central Vietnam, the average $\delta^{18}O_p$ seasonal cycle is very similar to the majority of MSEA, with more negative values occurring during the summer months and more positive values occurring during the winter months (Figure S1h). However, because central Vietnam receives the majority of its rainfall during autumn, the controls on weighted mean annual $\delta^{18}O_{p,}$ and hence cave dripwater $\delta^{18}O$, are more complex, and likely reflect the relative contribution of summer (more negative $\delta^{18}O$) vs autumn (more positive $\delta^{18}O$) rainfall. This signal is closely linked to the seasonal migration of the Intertropical Convergence Zone (ITCZ), which changes the annual contribution of isotopically light summer precipitation sourced from the Bay of Bengal and Indian Ocean vs isotopically heavier autumn precipitation sourced from the South China Sea and the Western Pacific (Figure S1g)(Wolf et al., 2020). Finally, it is possible that tropical cyclones may also influence $\delta^{18}O_p$ on short timescales, though we expect that mean annual $\delta^{18}O_p$ in central Vietnam is likely dominated by large-scale changes to atmospheric circulation rather than local rainfall events. Nevertheless, we find that HH-1 $\delta^{18}O$ shows a strong relationship with both $\delta^{13}C$ and Mg/Ca ($r = 0.79, 0.87$, $p < 0.01$ respectively), suggesting that HH-1 $\delta^{18}O$ may also reflect local hydroclimate change. If seasonality-driven changes in mean $\delta^{18}O_p$ were the primary control, though, we might expect periods of increased autumn rainfall, as indicated by $\delta^{13}C$ and Mg/Ca, to be associated with a more positive $\delta^{18}O$ signal due to increased contribution of higher $\delta^{18}O$ autumn rainfall, but we see the opposite relationship (locally wet periods exhibit more negative $\delta^{18}O$). An alternative explanation for the observed $\delta^{18}O$ pattern is that PCP, another potential control on speleothem $\delta^{18}O$ that has recently been proposed (Deininger et al., 2021), may also influence HH-1 $\delta^{18}O$ and explain the striking similarity between $\delta^{18}O$, $\delta^{13}C$, and Mg/Ca records. Because of these complex controls on $\delta^{18}O_p$ and the potential for local PCP driven changes to impact HH-1 $\delta^{18}O$, we focus our climatic interpretation on the Mg/Ca and $\delta^{13}C$ records.

Using the $\delta^{13}C$ and Mg/Ca records as tracers of local rainfall amount, we find that the Southeast Asian autumn monsoon underwent substantial change over the last 45,000 years (Figure 2.1). Low Mg/Ca, $\delta^{13}C$, and $\delta^{234}U_{initial}$ and high growth rate indicate relatively wet conditions prior to ~35 ka, followed by a gradual drying marked by increasing Mg/Ca, $\delta^{13}C$, and $\delta^{234}U_{initial}$ and decreasing growth rates. There is a rapid dry-wet transition at the end of HS3 (~30 ka), which is followed by an abrupt return to dry conditions at ~25 ka. With the exception of a 500 yr wet excursion at ~16 ka, dry conditions persist throughout the LGM and HS1. At ~14 ka there is an abrupt dry-wet shift marking the transition to persistent wet conditions for the remainder of the record.

With an average temporal resolution of ~30-50 years, the HH-1 record best resolves centennial-orbital scale hydroclimate variability. Thus, the HH-1 record is not likely to reflect short-term El Niño Southern Oscillation (ENSO) variability, a known control of

Southeast Asian hydroclimate on interannual-multidecadal timescales (Buckley et al., 2017; Sengupta & Nigam, 2019; Yamoah et al., 2016). On longer timescales, precessionally-driven Indo-Pacific Warm Pool ocean heat content has been linked to ENSO as well as ocean-continent moisture transport in the Asian monsoon region (Dang et al., 2020; Jian et al., 2022). However, the abrupt nature of change in the HH-1 record points towards different controls on central Vietnam hydroclimate, rather than the more gradual changes in ocean heat content.

The appearance of millennial scale events in the HH-1 record, such as Heinrich Stadials (dry conditions) and some DO events (wet conditions) (Figure 2.2), demonstrate that the Southeast Asian autumn monsoon is sensitive to changes in Atlantic Meridional Overturning Circulation. On orbital timescales, the HH-1 record shows little resemblance to East Asian summer or winter monsoon variability. Since precessionally-driven changes in insolation drive both systems (Wen et al., 2016), our results indicate that insolation forcing does not exert a direct control on Southeast Asian autumn monsoon rainfall variability. Instead, HH-1 $\delta^{13}C$ and Mg/Ca mirror changes in local sea level driven by global ice sheet volume changes (Figure 2.2). Periods of higher sea level correspond to wetter conditions and vice versa. This manifests as wet conditions during the sea level high stand of the late Marine Isotope Stage (MIS) 3 transitioning to a drying trend from 35-30 ka, which is followed by pronounced dry conditions during the LGM sea level low stand. An abrupt shift during Meltwater Pulse 1A (MWP1a; ~14.5 – 14 ka), a period of rapid sea level rise, punctuates the dry period, which is followed by wet conditions and higher sea level for the remainder of the record. While sea level change is a known driver of Indo-Pacific hydroclimate (Di Nezio et al., 2016; DiNezio & Tierney, 2013; Griffiths et al., 2009; Pico et al., 2020), few studies explore this relationship in MSEA (Hällberg et al., 2022; Yamoah et al., 2021). Notably, most studies focus on hydroclimate changes associated with the inundation of the Sunda and Sahul shelves during the deglaciation, which largely flooded after MWP1a, with the most rapid change occurring after the Younger Dryas (YD; 12.9 – 11.7 ka) (Figure S5a). An important difference in the HH-1 Mg/Ca and $\delta^{13}C$ records is that they show no hydroclimate response during or after the YD, but instead exhibit a large shift at ~14.2 ka, ~ 2 ka earlier than the YD. In fact, the HH-1 record better resembles the inundation history of the Gulf of Tonkin and the South China Shelf, located northeast of the study site, which first flood during MWP1a (Figure 2e, S5a). This indicates that local sea level change may drive changes in Southeast Asian autumn monsoon rainfall rather than the more distally located Sunda and Sahul shelves. Additionally, the Sunda/Sahul region is not a moisture source of modern central Vietnam rainfall (Figure S2), suggesting that the exposure/inundation of these landmasses are unlikely to affect moisture delivery to central Vietnam.

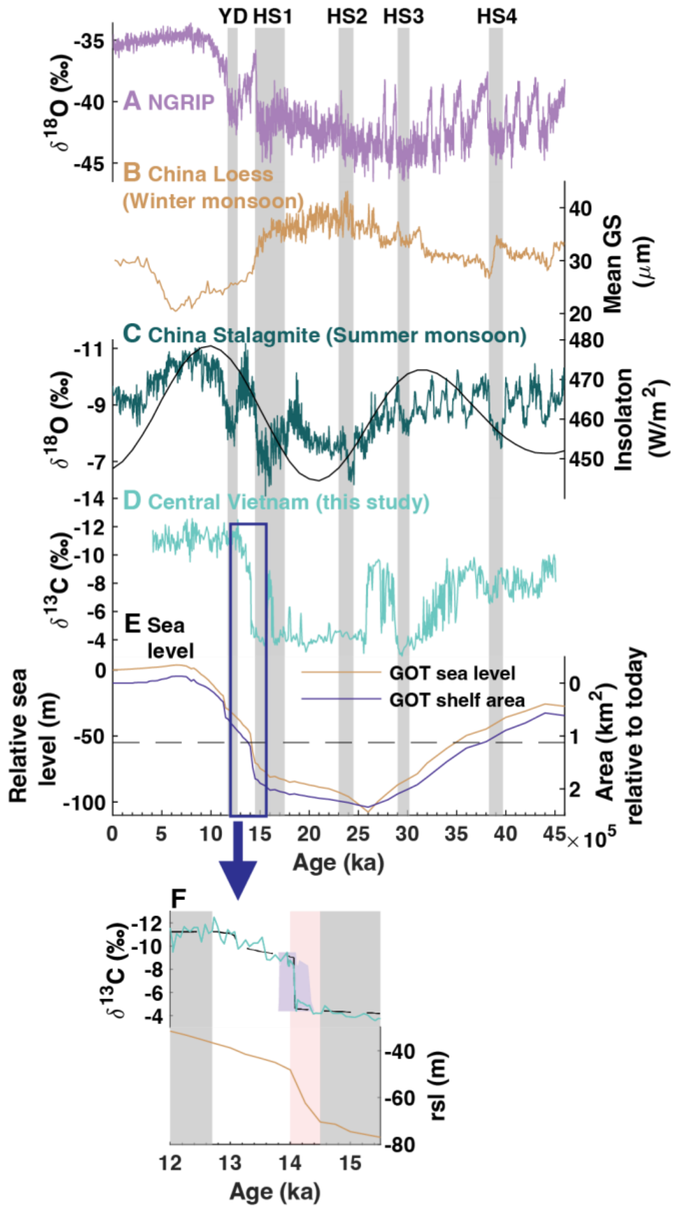

Figure 2.2. Comparison of HH-1 to regional records. a) Ice core $\delta^{18}O$ (VSMOW) from the North Greenland Ice Core Project (NGRIP; purple), b) mean grain size (GS) of the Jingyuan loess sequence from the northwestern Loess Plateau in China (tan)(Youbin Sun et al., 2010), c) composite stalagmite $\delta^{18}O$ (VPDB) record from China (green) (Cheng et al., 2016), d) HH-1 $\delta^{13}C$ (VPDB; turquoise), and e) Gulf of Tonkin (GOT) relative sea level (yellow) and shelf area (blue) reconstructed from the ICE-PC2 data product (Pico et al., 2017). GOT shelf are threshold of 120,000 km^2 plotted as black dashed line. f) Highlights a period of rapid change in HH-1 $\delta^{13}C$ (top) coinciding with rapid relative sea level rise (bottom) during MWP1a (pink shading; 14-14.5 ka). Black dashed curve in the top panel shows changepoints calculated using a Bayesian change-point algorithm (Ruggieri, 2013), which identifies a significant regime shift at 14.2 kyrs BP. The 2σ age model uncertainty (blue shading) shows that the $\delta^{13}C$ shift occurs during or after MWP1a.

2.3.2. Deglacial autumn monsoon rainfall variability characterized by rapid centennial-scale changes

Rapid mean-state change is a notable feature of the HH-1 record. Two prominent dry-wet shifts occur at the end of HS3 (~30ka) and during MWP1a, a period associated with rapid sea level rise (Figure 2.2). To further investigate the mechanisms behind these shifts, we utilize iTRACE, an isotope enabled transient climate model simulation which spans the deglaciation 20 - 11 ka (see *Methods*). We focus our analyses on the transition between HS1 and the Bølling-Allerød (BA) interstadial because this period encompasses substantial change in both sea level and meltwater flux. Note, we use the term *meltwater forcing* to refer to freshwater fluxes into the north Atlantic during Heinrich Stadials and the Younger Dryas. Meltwater forcing minimally contributes to sea level change, which is instead primarily driven by large-scale changes in continental ice sheet volume (Carlson & Clark, 2012).

Simulated precipitation from the grid cell encompassing Hoa Huong cave closely matches the HH-1 speleothem record (Figure 2.3a,b). Similarities include dry conditions throughout the LGM and HS1, and an abrupt shift to wet conditions at ~14 ka. The iTRACE simulations reveal that SON precipitation, rather than JJA precipitation, drives the jump at 14 ka observed in the speleothem record (Figure 2.3b). Indeed, the similarities between simulated precipitation in iTRACE and the HH-1 record support our interpretation of HH-1 being a robust proxy for autumn monsoon rainfall and demonstrate the strong control of SON precipitation variability on MSEA hydroclimate. On a regional scale, this shift (BA-HS1) manifests as a pronounced dry pattern during SON centered over the northern South

China Sea and extending into eastern MSEA (Figure 2.4b), whereas JJA precipitation change only causes weak drying in eastern MSEA (Figure 2.4a).

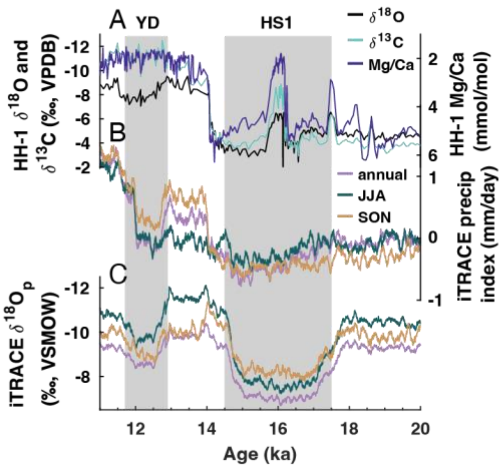

Figure 2.3. Comparison of HH-1 to iTRACE time series from 11-20 ka. a) HH-1 geochemical proxies, b) iTRACE precipitation (index) and, c) iTRACE weighted $\delta^{18}O_p$. In b and c we plot the annual mean (light purple), JJA (green), and SON (tan) from the grid cell encompassing the study site. We smoothed the iTRACE time series with a 100 yr running mean for aesthetic purposes and readability.

Using the iTRACE simulations, we attribute the SON drying pattern to two different mechanisms related to meltwater forcing and sea level change (Figure 2.4c,d). To isolate the effect of meltwater forcing, we assess the difference between the LGM (i.e., no meltwater forcing) and HS1 (i.e., enhanced meltwater forcing). The resulting pattern reveals anomalously dry conditions during HS1 across the northern South China Sea and western Pacific, which is caused by an anomalous anticyclone that advects dry air masses over eastern MSEA (Figure 2.4c). He *et al.*, 2021 (He et al., 2021) first described this phenomenon where a weakening of the Atlantic Meridional Overturning Circulation causes the convergence of anomalous northerly and southerly winds over South China during SON, creating a north-south precipitation dipole across South China (wet) and MSEA (dry). The antiphasing of the HH-1 record and the South China speleothem records is consistent with this dipole pattern (Figure S6). We find that this relationship even extends to the 16 ka wet excursion in the HH-1 record (dry in South China), a feature unexplained by the iTRACE simulations, demonstrating some regional coherence for this event. The dry conditions during HS2 (Mg/Ca), HS3 ($\delta^{13}C$ and Mg/Ca), and HS4 ($\delta^{13}C$) indicate that this mechanism persisted beyond the last deglaciation (Figure 2.2). However, we find that the Mg/Ca and $\delta^{13}C$ proxies do not consistently record dry conditions during all Heinrich Stadials, suggesting that drying from this mechanism may be limited. For example, we attribute the absence of drying during HS2 in the $\delta^{13}C$ record to the co-occurrence of the LGM, an already dry period in the record, which may obscure the drying effects from meltwater forcing. Similarly, neither Mg/Ca nor $\delta^{13}C$ show particularly dry conditions during HS1 when compared to the LGM, suggesting that both proxies may be less sensitive once conditions are already dry.

The 14 ka autumn precipitation jump in the iTRACE simulations corresponds to a change in global sea level (ICE forcing in Fiure. S7b) when the Gulf of Tonkin and the South China Shelf were flooded (Figure S8). The abrupt shift in the HH-1 record (14.2 ka) occurs slightly before this shift in the model (14 ka), but still falls within the timing of MWP1a, which is the most rapid period of global and local sea level rise during the deglaciation (Figure 2f). When we isolate the effect of this sea level forcing (BA-LGM), the iTRACE simulations reveal a strong regional drying pattern encompassing much of the northern South China Sea, eastern MSEA, and South China (Figure 2.4d). The strongest drying occurs over the Gulf of Tonkin and a shelf in South China, exposed landmasses during the LGM. iTRACE simulates anomalous subsidence over this region ($\omega > 0$) (Figure S9). Similar to the drying mechanism over the Maritime Continent during the LGM (DiNezio & Tierney, 2013; Du et al., 2021), this exposed land cools more than the adjacent ocean, reducing convection

(Figure S9). This decrease in moisture ultimately reduces MSEA SON rainfall, as this region lies northeast of MSEA, along the moisture transport pathway of the Southeast Asian autumn monsoon (Figure S2c).

To summarize, we attribute the abrupt dry-wet shift at the end of HS3 to meltwater forcing, whereas the shift at 14.2 ka is primarily driven by rapid sea level rise during MWP1a. However, it is worth noting that neither the sea level or meltwater mechanisms explain the abrupt drying at 25 ka, or the wet excursion during HS1 (~16 ka). We propose that the wet conditions during 30 – 25 ka reflect the two DO events that occur during this time, which may have created wet conditions before returning to dry conditions at ~25 ka. The 16 ka event likely reflects a more localized hydroclimate shift, with some evidence that it is a regional event spanning from central Vietnam to South China (Figure S6). Another notable discrepancy is the shift to dry conditions in the iTRACE simulations during the YD, a feature that does not appear in the $\delta^{13}C$ or Mg/Ca records. Similar to BA-HS1 drying, iTRACE analyses reveal that both meltwater forcing and sea level rise contribute to the dry-wet transition at the end of the YD (Figure S10). This discrepancy indicates that iTRACE may overestimate drying during this period, or that the $\delta^{13}C$ or Mg/Ca proxies at our cave site are not sensitive enough to detect this change. Notably HH-1 $\delta^{18}O$ does increase during the YD. Since the controls on $\delta^{18}O$ are unclear, this feature could reflect local drying and/or large-scale changes to atmospheric circulation.

Consistent with previous findings that local rainfall amount does not control central Vietnam $\delta^{18}O_p$ (Wolf et al., 2020), weighted iTRACE $\delta^{18}O_p$ and precipitation show some important differences. Unlike iTRACE precipitation and the HH-1 local hydroclimate proxies (Figure 2.3a,b), iTRACE $\delta^{18}O_p$ does not exhibit an abrupt shift associated with sea level rise during MWP1a (Figure 2.3c). Instead, changes in iTRACE $\delta^{18}O_p$ show ties to meltwater forcing with values increasing at the onset and decreasing at the end of HS1. On a spatial scale, iTRACE $\delta^{18}O_p$ does not resemble rainfall anomalies across MSEA (Figure 2.4a,b, Figure S11), further demonstrating the dissociation of local rainfall and $\delta^{18}O_p$.

Since central Vietnam receives rainfall during summer and autumn, it is possible that summer rainfall contributes to changes in the HH-1 record. In addition to decreased autumn rainfall, decreased summer rainfall may add to the dry conditions during Heinrich Stadials. iTRACE simulations reveal a weak meltwater-driven drying pattern over the study site during HS1 (Figure 2.4a, MWP curve in S7a). This is a well-known phenomenon, where weakened Atlantic Meridional Overturning Circulation during Heinrich Stadials shifts the ITCZ and the westerly jet south, weakening the Asian summer monsoon and changing rainfall patterns across the region (He et al., 2021; Zhang & Delworth, 2005). Conversely, we do not expect sea level change at the Gulf of Tonkin and South China Shelf to affect summer precipitation because the moisture source and transport pathway lie west of the study site (Figure S2b). While the inundation/emergence of the Sunda Shelf does affect summer rainfall across MSEA (Yamoah et al., 2021), we reiterate that the Sunda Shelf inundation history does not match the hydroclimate change documented in the HH-1 record (Figure S5a). For this reason, we suggest that hydroclimate changes due to sea level change reflect shifts in autumn monsoon rainfall.

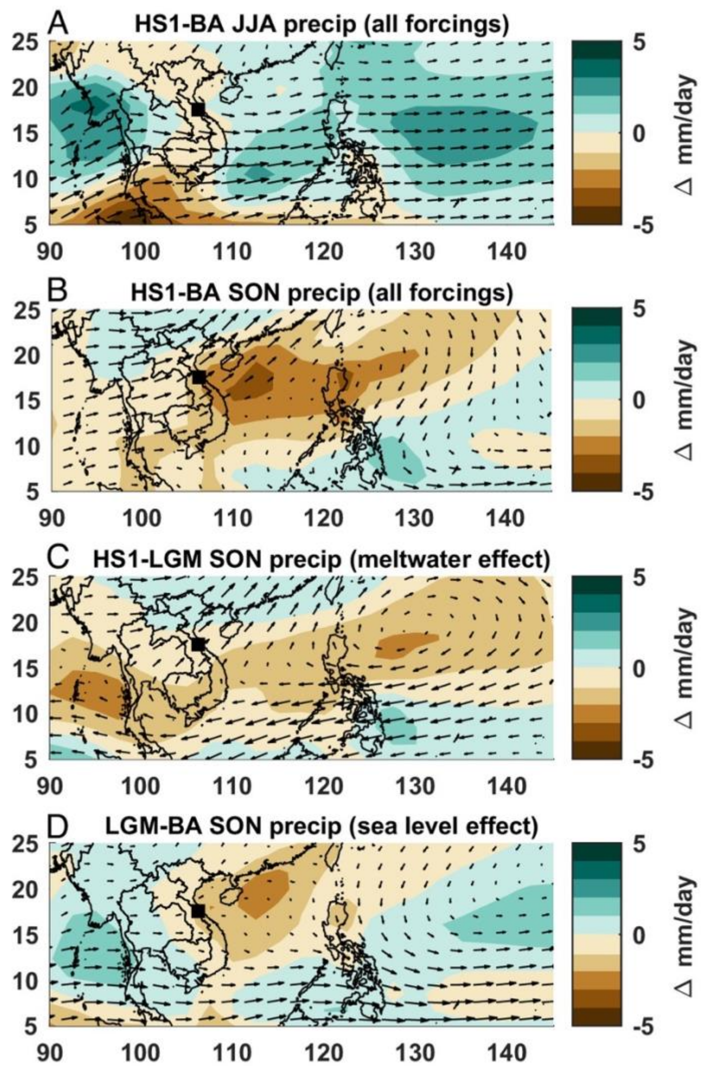

Figure 2.4. iTRACE precipitation and 850 mbar wind anomalies over MSEA. a) and b) show anomalies between HS1 and BA for JJA and SON, respectively. c) HS1-LGM isolates the meltwater effect on SON precipitation during HS1 by subtracting the LGM, a baseline cold period with no meltwater forcing, from HS1. d) LGM-BA isolates the sea level effect on SON precipitation by subtracting the LGM, a period of low sea level and no meltwater forcing, from BA, a period of high sea level. The black square in all panels denotes the location of Hoa Huong cave.

2.3.3. Sea level change modulates MSEA autumn monsoon rainfall variability

On orbital timescales, local sea level change is the dominant driver of Southeast Asian autumn monsoon rainfall variability. HH-1 does not linearly track relative sea level change, but rather follows the inundation history of the Gulf of Tonkin and the South China Shelf (Figure 2.2e, S8d,e). Wet conditions from 45-35 ka and 13-4 ka correspond to periods when these landmasses were largely inundated. The driest conditions occur during the LGM, when sea level is lowest (Figure 2.2e). The drying trend during late MIS 3 from 35-30 ka occurs during a period when global mean sea level dropped > 40 m (Figure S5b) (Yokoyama et al., 2018), exposing the Gulf of Tonkin and the South China Shelf (Figure S8e). The abrupt shift to wet conditions during MWP1a occurs during rapid regional inundation from 14.5 – 14 ka (Figure S8d). Wetting conditions continue in the HH-1 record from 14 – 13 ka, but at a slower rate than during MWP1a, matching a similar shift in the rate of local sea level rise (Figure 2.2f). Notably, sea level is higher prior to 35 ka and after 13 ka, but we do not see a corresponding wetting trend in the HH-1 proxies. Instead, the HH-1 Mg/Ca and $\delta^{13}C$ records appear to reach a lower limit indicating that there may be a threshold where shelf exposure no longer contributes to regional drying. We note that this threshold occurs at a similar stage in sea level history regardless of increasing or decreasing sea level, when the Gulf of Tonkin shelf exposure is ~112,000 km^2 (dashed black line in Figure 2.2e). Alternatively, this limit may reflect a threshold in the proxies themselves, where they are no longer sensitive to wetter conditions (i.e. PCP = 0).

While sea level is not the only driver of Southeast Asian autumn monsoon rainfall variability, its relative state (high or low) appears to modulate centennial- and millennial-scale events in the HH-1 record. This is most obvious during wet events, which are dampened during sea level highstands and amplified during low sea level. For example, the DO events during high sea level (45-35 ka) result in ~1 ‰ negative excursions in $\delta^{13}C$ record, whereas the two DO events during low sea level coincide with a ~6 ‰ negative excursion from 30 - 25 ka (Figure 2.2). Other anomalies in the HH-1 record, including the wet excursion during HS1 and pronounced variability during the 35-30 ka drying trend, further demonstrate how a lower sea level contributes to a more volatile hydroclimate in central Vietnam. The relationship between sea level and dry events is less clear. However, the strongest drying response to meltwater forcing in the $\delta^{13}C$ record occurs during HS4, a period of high sea level. The drying during Heinrich Stadials 1-3 is more muted, suggesting that the stronger sea level mechanism may obscure the weaker meltwater drying signal associated with Heinrich Stadials.

In conclusion, our multiproxy record reveals that sea level is the main driver of Southeast Asian autumn monsoon rainfall variability on orbital timescales. Changes in sea level and meltwater forcing lead to abrupt hydroclimate change in central Vietnam, demonstrating the important role autumn rainfall plays in MSEA across a variety of timescales. Finally, the agreement between climate model analyses and the HH-1 record adds confidence that climate projections may correctly simulate the Southeast Asian autumn monsoon, improving our understanding of how rainfall changes might affect this densely populated region.

2.4. Methods

2.4.1. U-Th dating and age model construction

We drilled 36 samples for U-Th dates from the central growth axis of stalagmite HH-1 using a handheld rotary tool with a diamond bur. U-Th measurements were conducted at Massachusetts Institute of Technology where powdered samples (~100-250 mg) were dissolved, spiked with a ^{229}Th-^{233}U-^{236}U tracer, separated of U and Th by iron co-precipitation and elution in columns with AG1-X8 resin, and analyzed using a Nu Plasma II-

ES multi-collector inductively coupled plasma mass spectrometer (MC-ICP-MS) equipped with an Aridus 2 desolvating nebulizer, following methods described in Burns *et al*., 2016 (Burns et al., 2016). We corrected raw ages for initial ^{230}Th using an initial $^{230}Th/^{232}Th$ value of 25±12.5 ppm. All dates are in stratigraphic order (Table S1), except for UU-H12, which we excluded from the final age model. The top and bottom dates are 3,961 and 45,109 years before present, respectively. To construct the HH-1 age model and 95% confidence interval (Figure S3c), we performed 2,000 Monte-Carlo simulations via the COPRA age-depth modeling software (Breitenbach et al., 2012).

2.4.2. Geochemical analyses

We drilled samples for geochemical analyses along the central axis of HH-1. Since the growth rate of HH-1 ranges from 2-329 μm/yr, we opted to vary the sampling interval dependent on growth rate. For fast growing portions of the stalagmite, we sampled at 2.5-5 mm intervals using a handheld rotary tool fitted with a 1 mm diameter diamond bur. We sampled slow growing portions of the stalagmite continuously at 0.25-0.5 mm resolution using a Sherline micromill.

We analyzed 1,385 samples for Mg/Ca on a Nu Instruments Attom High-Resolution Inductively Coupled Plasma Mass Spectrometer (HR-ICP-MS) at the Center for Isotope Tracers in Earth Science (CITIES) laboratory at the University of California, Irvine (average uncertainty (1σ) = 3%). Raw intensities were converted to concentrations utilizing an external calibration curve constructed using five standards of known concentration and a blank. To correct for instrument drift, we spiked all samples, standards, and blanks with an internal Ge standard prior to analysis. The final HH-1 Ma/Ca record has an average resolution of ~30 years.

Due to the similarities between the Mg/Ca and isotope records we chose to analyze a subset of 771 samples for stable isotopes, which yields an average resolution of ~50 years. Stable carbon and oxygen isotopes measurements were performed at the University of Arizona Stable Isotope Lab, using a KIEL-III Carbonate Device coupled to a Finnigan MAT252 isotope ratio mass spectrometer (1σ of ± 0.11 ‰ for $\delta^{18}O$, 0.08 ‰ for $\delta^{13}C$) and in the Department of Earth and Planetary Sciences, Rutgers University, using a Multiprep device attached to a MicroMass Optima Mass Spectrometer. Isotope ratios were calibrated to repeated measurement of NBS-19 and NBS-18 at the University of Arizona and to an in house lab reference material (RGF1) at Rutgers, which is routinely calibrated to NBS19 at Rutgers. We applied a small correction the University of Arizona $\delta^{18}O$ measurements, which are offset by +0.2 ‰ relative to the Rutgers measurements. Values reported in VPDB.

2.4.3. iTRACE

iTRACE is a water isotope enabled transient simulation of the last deglaciation (11-20ka) (He et al., 2021). iTRACE simulations are performed in iCESM1.3 (Brady et al., 2019), which is comprised of Community Atmosphere Model version 1.3 (CAM5.3), the Community Land Model version 4 (CLM4), Parallel Ocean Program version 2 (POP2), and Los Alamos Sea Ice Model version 4 (CICE4). The resolution of the land and atmosphere is 1.9°x2.5° (latitude and longitude) with 30 vertical levels in the atmosphere. iCESM 1.3 simulations are well validated against modern observations of global precipitation and precipitation isotopes (Brady et al., 2019; Nusbaumer et al., 2017; Wong et al., 2017). When compared to modern observations, preindustrial iCESM 1.3 simulations closely capture seasonal changes in rainfall and $\delta^{18}O_p$ across MSEA and central Vietnam, including the transition from the SW summer monsoon to the NE autumn monsoon (Figure S1).

iTRACE uses four forcing factors (ICE: continental ice sheets from the ICE-6G model (Peltier et al., 2015) and KMT ocean bathymetry, ORB: orbital forcing, GHG: greenhouse gas concentrations from ice core reconstructions (Lüthi et al., 2008; Petit et al., 1999; Schilt et al., 2010), and MWF: meltwater fluxes (hosing) following TRACE-21ka (Liu et al., 2009), which are applied additively to create four parallel simulations (ICE, ICE + ORB, ICE + ORB + GHG, and ICE + ORB + GHG + MWF). The first three simulations start at 20 ka, whereas the MWF experiment begins at 19ka. Ice sheet configuration changes in 1,000 year increments and ocean bathymetry is modified twice at 14ka and 12ka based on changes in global sea level from the ICE-6G model (Figure S8a-c). At 14ka the Gulf of Tonkin and the shelf in South China are flooded. At 12ka the Sunda and Sahul shelves are flooded. To approximate the effect of a single forcing, we subtracted simulations from each other (e.g. ORB = (ICE + ORB) – ICE). Refer to (He et al., 2021) for additional details on the forcings. In this study, we compare the mean state of several time periods including 11.1 ka (11.1 – 11 ka, the last 100 years), the YD (12.7 – 12.4 ka), the BA (13.8 - 13.3 ka), HS1 (15.5 - 15 ka) and the LGM (20 – 19 ka).

2.4.4. Sea level and paleoshoreline reconstruction

To calculate relative sea-level change at the Gulf of Tonkin, we used a gravitationally self-consistent glacial isostatic adjustment model. Our calculations are based on the theory and pseudo-spectral algorithm described by Kendall et al. (2005) (Kendall et al., 2005) with a spherical harmonic truncation at degree and order 512. These calculations include the impact of load-induced Earth rotation changes on sea level (Milne & Mitrovica, 1996; Mitrovica et al., 2005), evolving shorelines and the migration of grounded, marine-based ice (Johnston, 1993; Kendall et al., 2005; Lambeck et al., 2003; Milne et al., 1999).

Our numerical predictions require models for Earth's viscoelastic structure and the history of global ice cover. We adopted the viscosity profile VM2 (Peltier & Fairbanks, 2006) and the ICE-PC2 global ice history (Pico et al., 2017) to reconstruct relative sea level and paleoshorelines. The ICE-PC2 global ice history is characterized by a peak GMSL value during MIS 3 of −37.5 m at 44 ka, following Pico et al. (2016) (Pico et al., 2016), and −15 and −10 m during MIS 5a and 5c, respectively, which are within the ranges derived by Creveling et al. 2017 (Creveling et al., 2017). We plot relative sea level from the nearest present day ocean grid cell east of the study site (~18 ºN, 107 ºE) and calculated the inundation history of the Gulf of Tonkin within the area 15-23 ºN, 105-112 ºE (Figure 2.2e). To reconstruct paleoshorelines, we subtracted the predicted relative sea level change of a particular time step from the present day topography (BOCD GEBCO data set, https://www.gebco.net/). ICE-PC2 interpolates sea level between MIS 3 and the LGM. To address this uncertainty, we also compare the HH-1 record to a coral-based global mean sea level reconstruction (Figure S5b) (Yokoyama et al., 2018), a more detailed record of sea level change during this time.

APPENDIX B

1. Cave and speleothem sample.

Hoa Huong Cave (HH cave) is a 3,910 m-long cave located 411 m above sea level in Phong Nha-Ke Bang National Park in Quang Binh Province, Vietnam (17.5°N, 106.2°E). Members from the Vietnam Caves Expedition group extensively surveyed HH cave in 2012 and 2016. HH cave has one known entrance, which intersects the continuous cave passageway. The thickness of bedrock overlying the cave ranges from a few meters close to the entrance to >100 meters in the deeper sections of the cave. Dense, tropical, evergreen forest comprise the vegetation overlying and surrounding HH cave.

We have conducted cave monitoring at HH cave since March 2020. Over two years of logger data reveal that mean cave temperature is 20 °C with a seasonal cycle of 1.5-2 °C. While mean annual temperature in the nearest town, Phong Nha, is ~23 °C, we believe that HH cave temperature still reflects mean annual temperature because of its higher elevation (>200 m higher than Phong Nha) and location in densely vegetated forest. Cave relative humidity is over 95% throughout the year. These relatively constant temperature and relative humidity conditions are favorable for stalagmite formation. Two cave air pCO_2 measurements from March 2020 (820ppm) and August 2022 (3120pm) suggest that HH cave may have seasonal ventilation. Additional pCO_2 measurements are needed to confirm the presence/or and magnitude of the seasonal cycle.

We collected the previously broken stalagmite, HH-1 (Figure S3a,b), ~150 m from the cave entrance. There is no active drip above the base of HH-1, so no dripwater monitoring is possible at this specific location in the cave. The top of the sample and the ceiling of the cave show remnants of a soda straw, which was likely connected to the top of the stalagmite before it fell. HH-1 is comprised of dense calcite. While speleothem morphology remains relatively constant throughout the sample, indicating a constant drip rate (Martín-Chivelet et al., 2017), fabric changes coincide with changes in growth rate. Darker banding corresponds with slower growing portions of the stalagmite, whereas white or clear banding corresponds with faster growing portions (Figure S3b). To confirm that HH-1 grew continuously, we sampled U-Th dates on either side of fabric changes (Table S1).

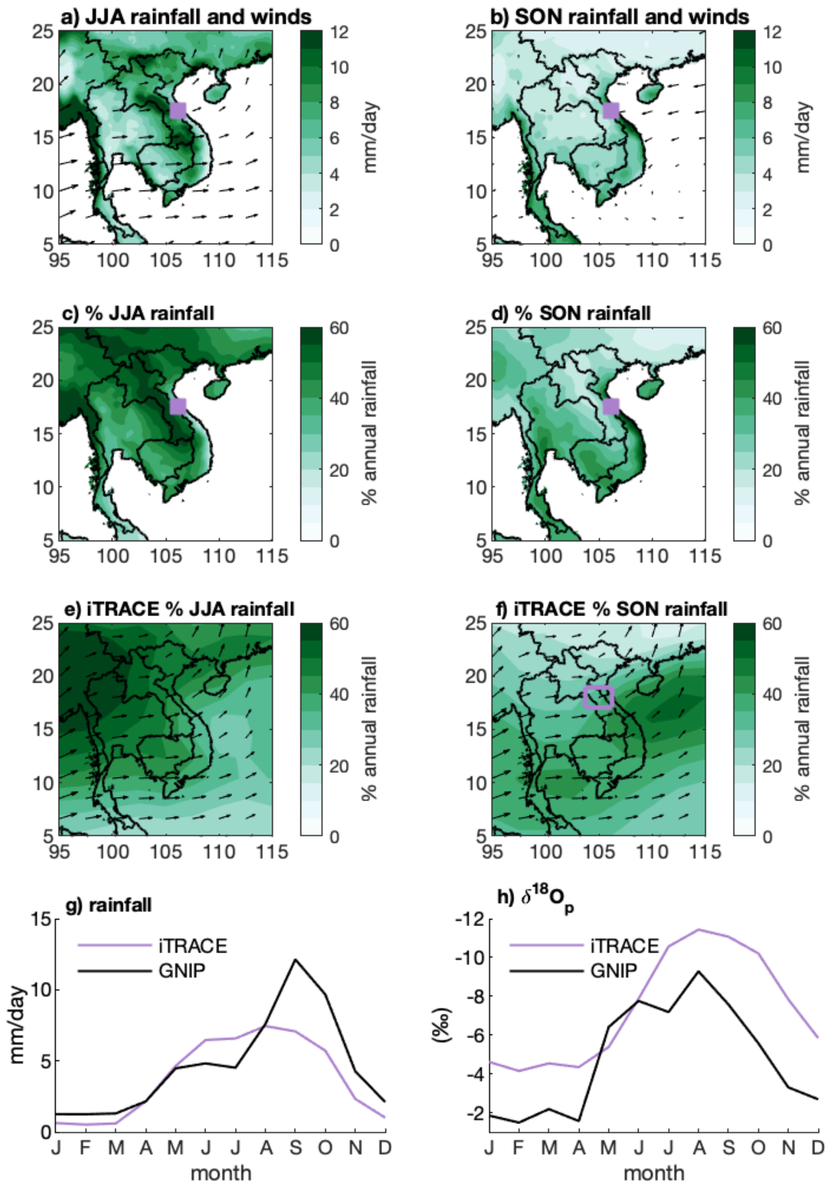

Fig. S1. Central Vietnam climatology and comparison to iTRACE. Average a) JJA and b) SON rainfall (1951-2007) derived from Asian Precipitation-Highly Resolved Observational Data Integration Towards Evaluation (APHRODITE)(Yatagai et al., 2012) and 850 mb winds (1951-2007) derived from NCEP reanalysis winds (Kalnay et al., 1996). Annual proportion of c) JJA and d) SON rainfall. The purple square denotes the location of Hoa Huong cave. Panels e) and f) are the same as c) and d) but show % annual rainfall and average 850 mb winds from the iTRACE preindustrial simulation. Seasonal cycle of g) rainfall from Aphrodite (black) and iTRACE (purple) and h) $\delta^{18}O_p$ from the GNIP station in Dong Hoi (black) and iTRACE (purple). iTRACE seasonal cycle derived from the grid cell encompasses HH cave (purple box in f).

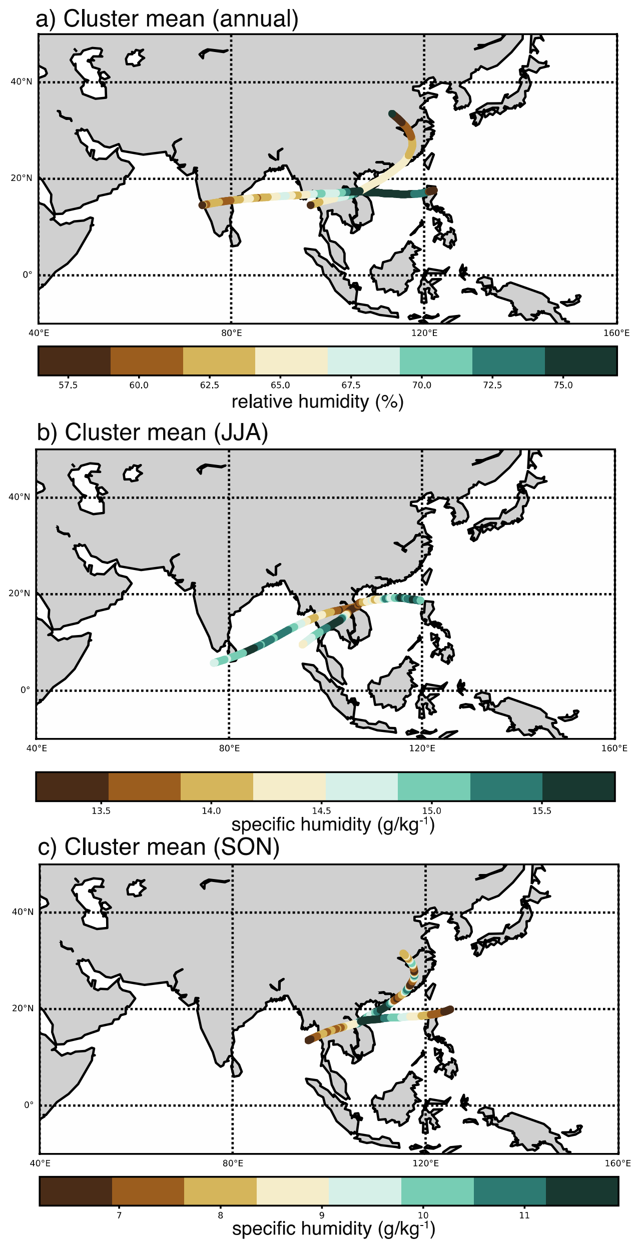

Fig. S2. Moisture source back-trajectory for rainfall in central Vietnam. Main Hybrid Single-Particle Lagrangian Integrated Trajectories (HYSPLIT) (Stein et al., 2015) cluster trajectories showing relative humidity for a) annual, and specific humidity for b) JJA, and c) SON. Clusters constructed from daily rain-bearing trajectories from 2006-2018 using meteoric parameters from the Global Data Assimilation System (GDAS) 0.5° dataset. We use the HYSPLIT model to calculate daily backward trajectories every 6 hours tracing for 120 hours, at a height of 1500 m above mean sea level. The simulated trajectories are used to calculate the cluster means using a cluster analysis method in HYSPLIT (Wolf, 2023). Only rain-bearing trajectories are included in the cluster means. Evaporation and precipitation thresholds were set to -0.2 and 0.2, respectively.

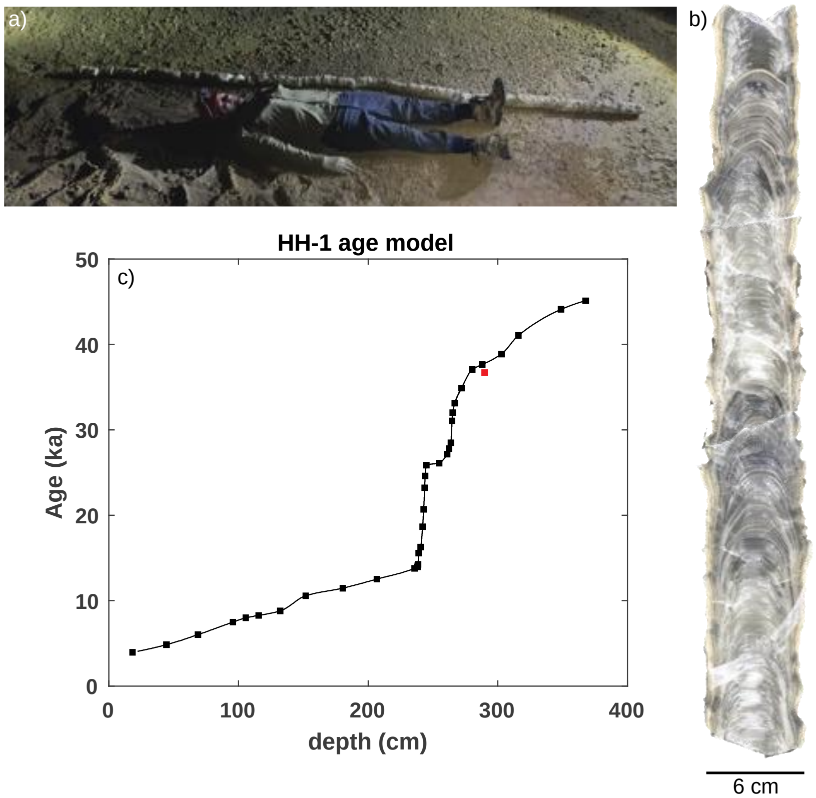

Fig. S3. HH-1 morphology and age model. a) Photo of HH-1 in HH cave. b) Scanned image of a portion of HH-1 to show representative fabric. c) HH-1 age-depth model. Black squares indicate U-Th dates and the red square indicates the one date excluded from the age model. The 2σ error bars are plotted, but are smaller than the symbol. Age uncertainty can also be found in Table S1.

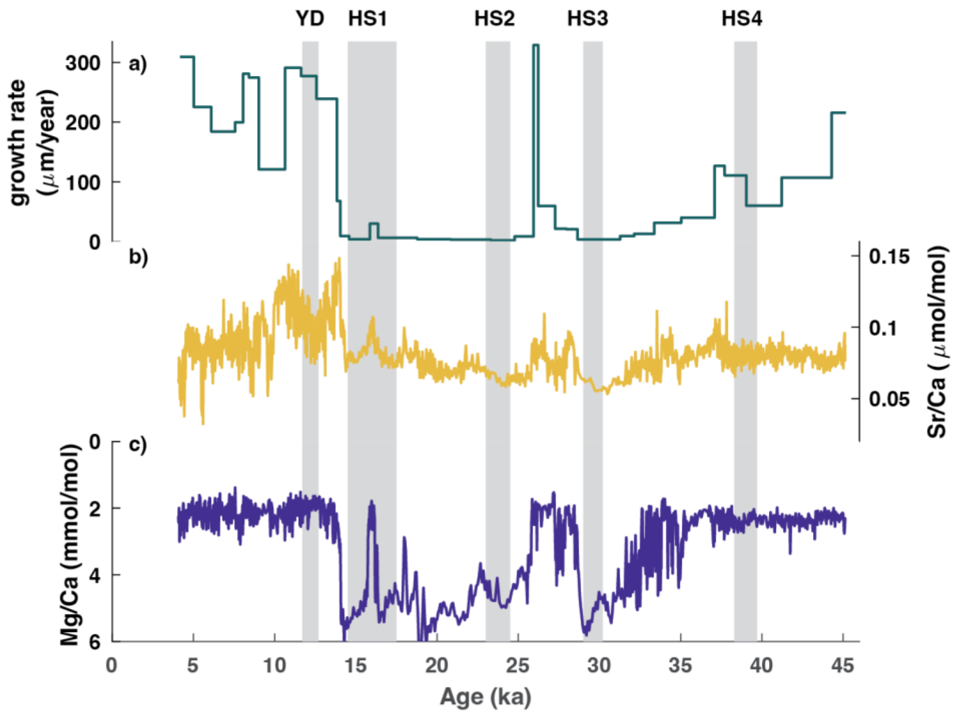

Fig. S4. HH-1 Sr/Ca vs other HH-1 proxies. a) growth rate (green), b) Sr/Ca (yellow), c) Mg/Ca (blue; note inverted axis).

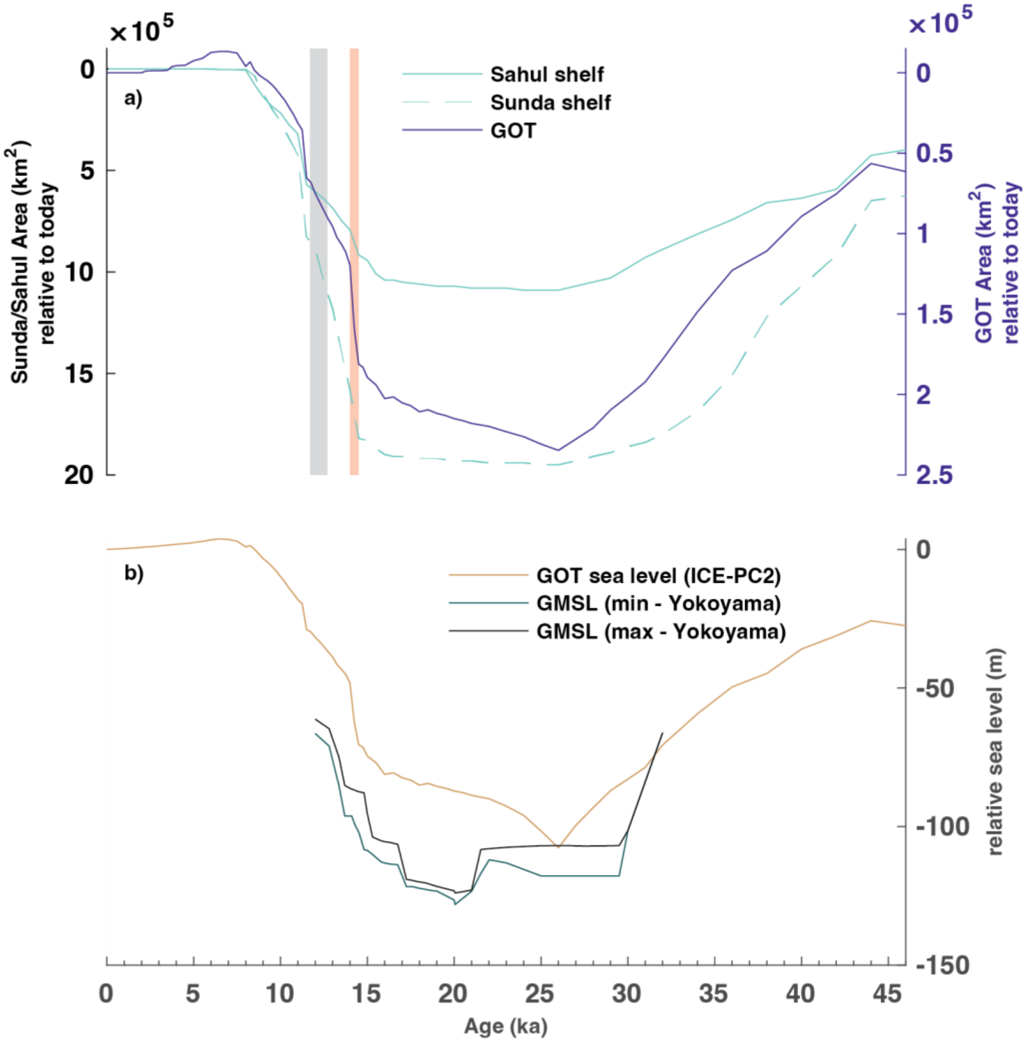

Fig. S5. Regional shelf exposure and sea level history. a) Shelf exposure curves of the Sahul Shelf (turquoise - solid), Sunda Shelf (turquoise - dashed), and the Gulf of Tonkin (GOT; dark blue) reconstructed from the ICE-PC2 data product (Pico et al., 2017). The pink shading denotes the timing of MWP1a (14 – 14.5 ka) and the grey denotes the YD (12.9 – 12.7 ka). The Sunda and Sahul shelf exposure curves are from (Pico et al., 2020). b) GOT relative sea level from ICE-PC2 data product (tan), and minimum (dark green) and maximum (black) estimates of global mean sea level (GMSL) from a coral-based reconstruction (Yokoyama et al., 2018).

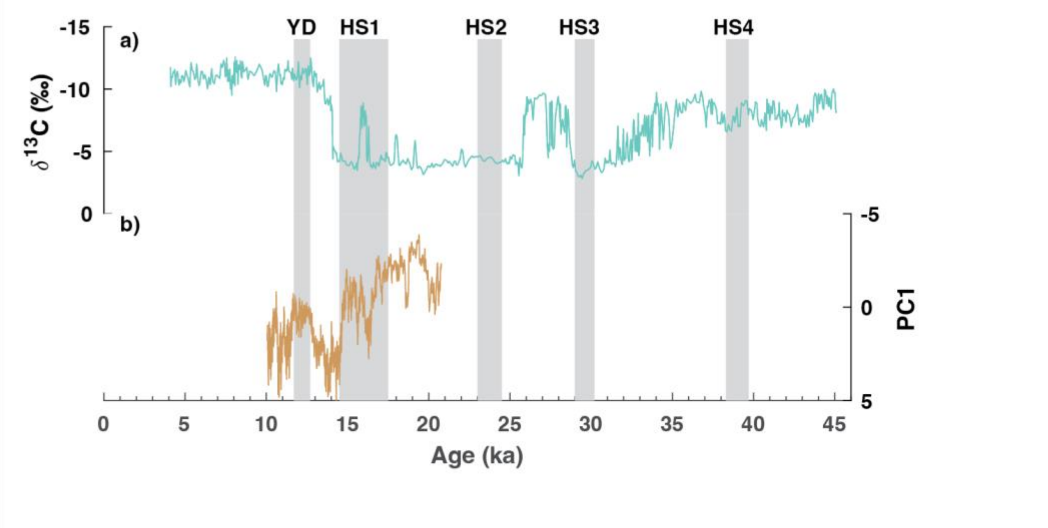

Fig. S6. Comparison of a) HH-1 δ^{13}C (turquoise) and b) PC1 of trace element records from two stalagmites from Haozhu Cave in central China (tan) (Zhang et al., 2018)**.**

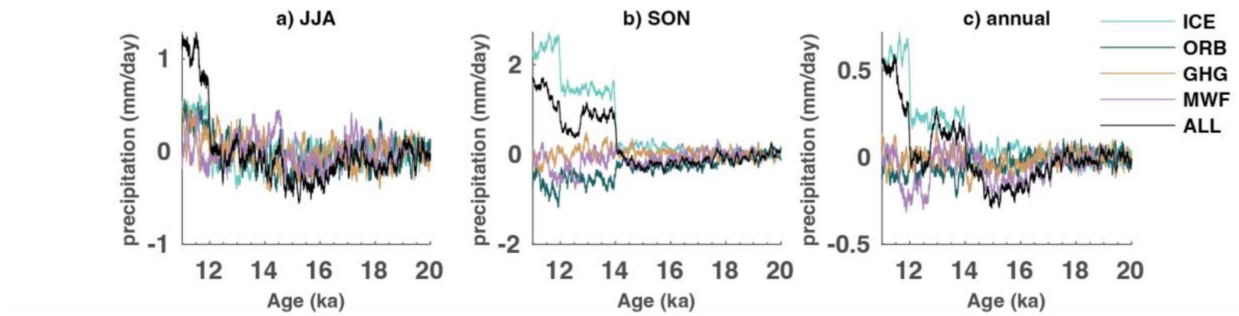

Fig. S7. Time series of individual forcings of simulated iTRACE precipitation. iTRACE a) JJA, b) SON, and c) annual precipitation time series from the grid cell encompassing the study site in response to different forcings (ICE - turquoise, ORB - green, GHG - tan, MWF - purple, and ALL forcings - black). We standardize the curves by subtracting the LGM climatology. The different forcings are isolated from the different iTRACE runs as follows; ICE = ICE – LGM, ORB = ICE + ORB – ICE – LGM , GHG = ICE + ORB + GHG – ICE + ORB – LGM, and MWF = ICE + ORB + GHG + MWF – ICE + ORB + GHG – LGM. Curves are smoothed with a 100 year running mean.

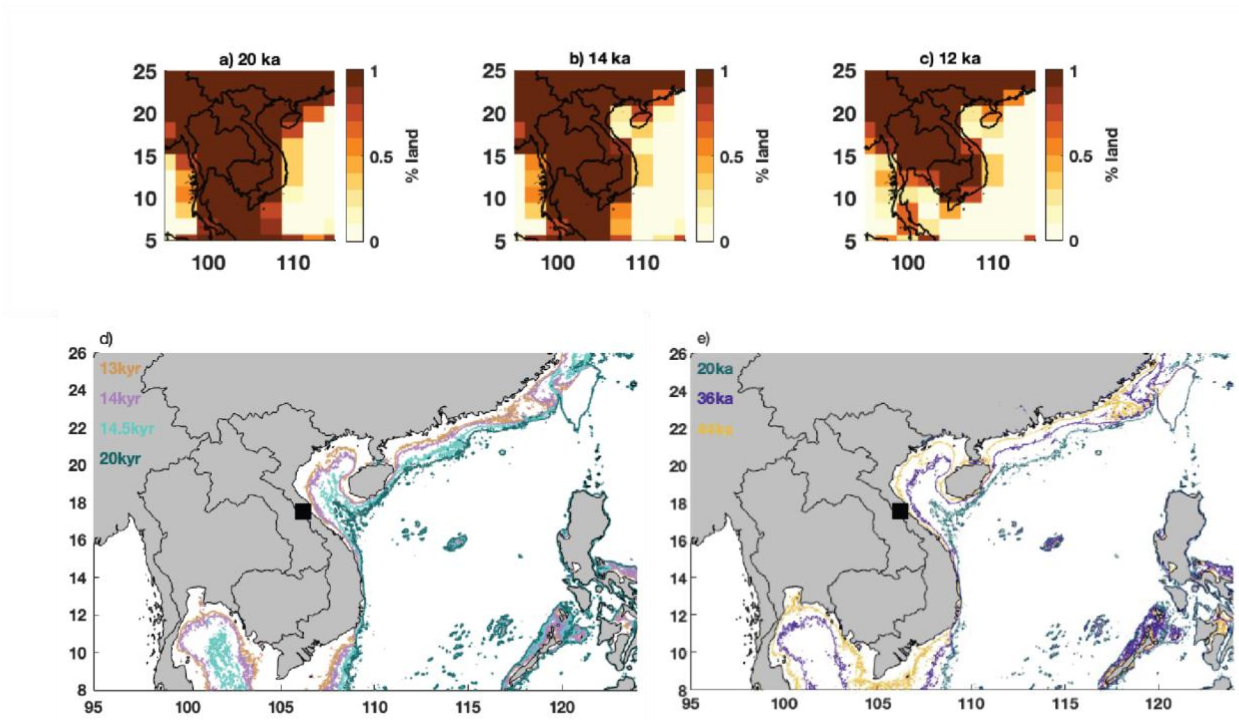

Fig. S8. Sea level change during the deglaciation. iTRACE atmosphere model land fraction used at a) 20 ka, b) 14 ka, and c) 12 ka. Each grid cell has a value ranging from 0% to 100% land. Paleoshorelines from the ICE-PC2 global ice history during the d) deglaciation and e) late MIS 3.

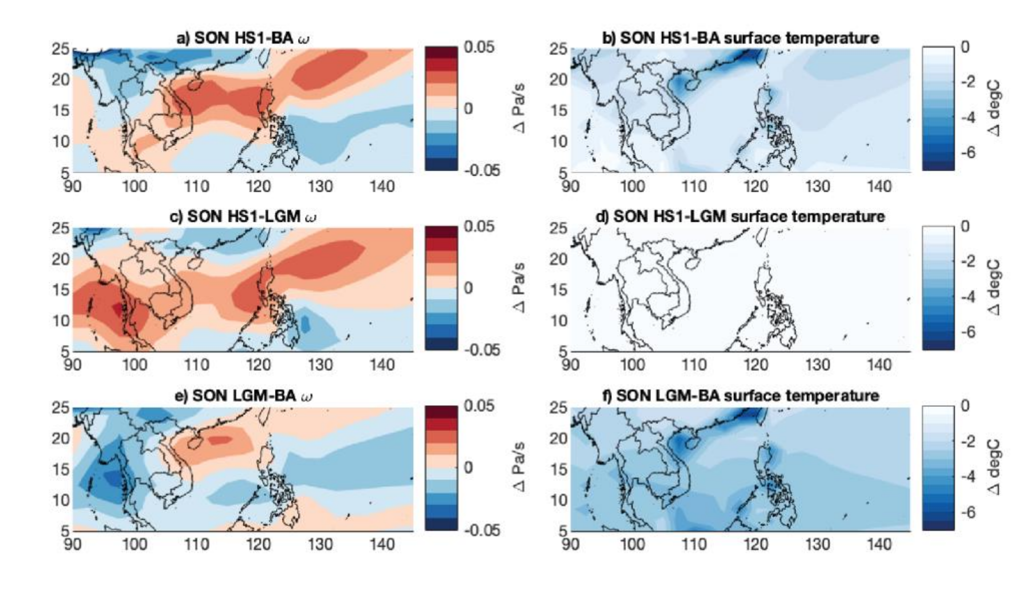

Fig. S9. **iTRACE JJA vertical velocity (ω) and surface temperature anomalies during for a,b) HS1 – BA, c,d) HS1 – LGM, and e,f) LGM – BA.** Note, colors in panel d are muted because temperature change is small.

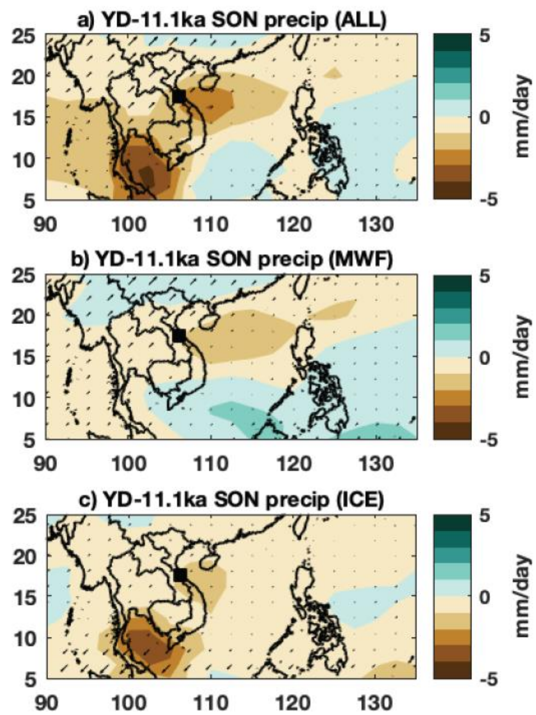

Fig. S10. iTRACE precipitation and 850 mbar wind anomalies over MSEA during YD – 11.1 ka for a) all forcings (ALL), b) meltwater forcing (MWF), and c) sea level forcing (ICE). The YD-11.1 ka time period encompasses a period in the iTRACE simulations with enhanced meltwater forcing during the YD and sea level change at 12 ka.

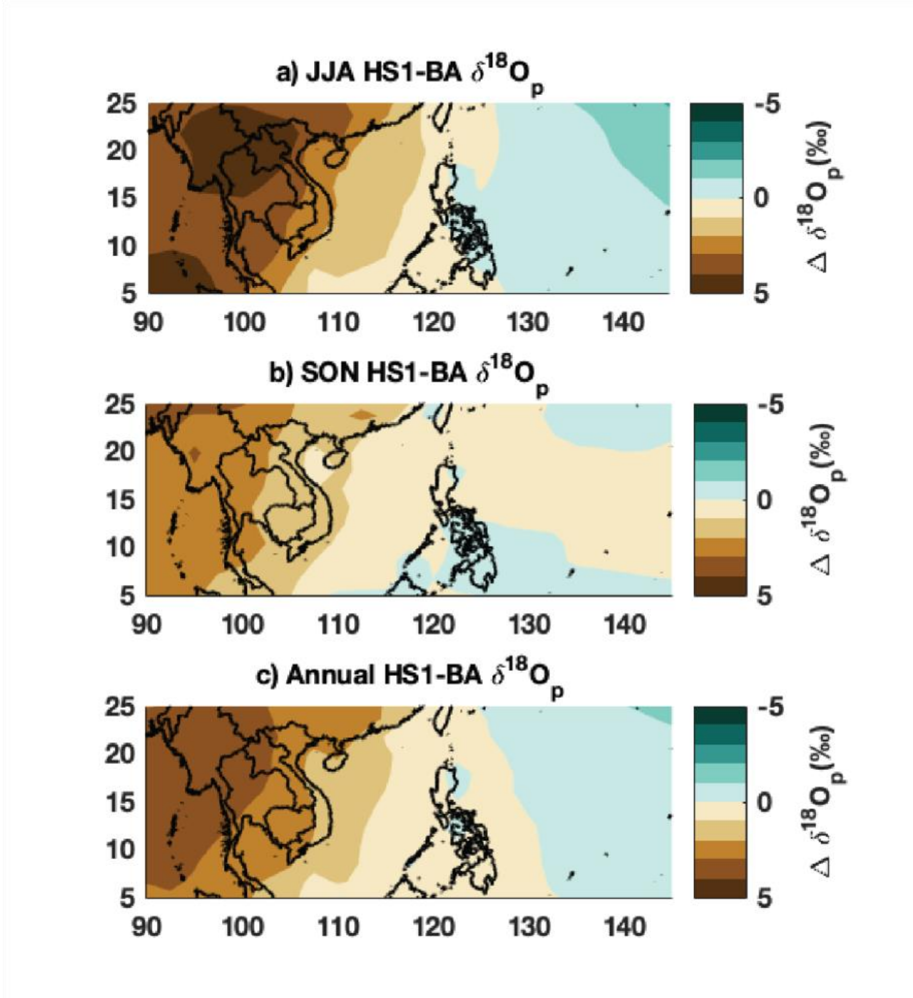

Fig. S11. iTRACE a) JJA, b) SON, and c) annual weighted $\delta^{18}O_p$ anomalies during HS1-BA.

Table S1. HH-1 U-Th dates.

Sample ID	Depth (cm)	^{238}U (ng/g)	^{232}Th (pg/g)	$\delta^{234}U$ (‰)	$^{230}Th/^{238}U$ (activity)	$^{230}Th/^{232}Th$ (ppm atomic)	$\delta^{234}U$ initial (‰)	Raw age (yrs BP)	Corr. age (yrs BP)
UU-H2	18.2	140 ± 3	790 ± 16	2728 ± 2	0.1444 ± 0.0006	405 ± 2	2759 ± 2	4290 ± 19	3961 ± 131
UU-H3	44.4	82 ± 2	388 ± 8	2845 ± 1	0.1776 ± 0.0008	596 ± 3	2885 ± 2	5128 ± 24	4848 ± 107
UU-H4	68.7	79 ± 2	168 ± 3	2873 ± 2	0.2150 ± 0.0011	1599 ± 11	2923 ± 2	6186 ± 33	6022 ± 57
UU-H5	95.7	87 ± 2	180 ± 4	2947 ± 1	0.2696 ± 0.0013	2071 ± 13	3011 ± 1	7651 ± 37	7492 ± 57
HH-U33	105.6	98 ± 2	166 ± 3	2897 ± 2	0.2828 ± 0.0012	2670 ± 12	2963 ± 2	8144 ± 36	8001 ± 51
UU-H6	115.6	78 ± 2	293 ± 6	2659 ± 1	0.2773 ± 0.0012	1167 ± 6	2722 ± 2	8517 ± 39	8272 ± 96
HH-U34	132.2	94 ± 2	571 ± 11	2806 ± 2	0.3089 ± 0.0014	805 ± 4	2877 ± 2	9140 ± 43	8800 ± 142
UU-H7	151.8	102 ± 2	203 ± 4	3130 ± 1	0.3913 ± 0.0015	3128 ± 16	3225 ± 2	10725 ± 43	10574 ± 59
UU-H8	180.4	101 ± 2	457 ± 9	2919 ± 2	0.4045 ± 0.0014	1415 ± 5	3016 ± 2	11728 ± 43	11463 ± 106
UU-H9	206.7	128 ± 3	180 ± 4	3146 ± 1	0.4603 ± 0.0016	5186 ± 31	3260 ± 2	12652 ± 46	12525 ± 54
UU-H10	235.9	129 ± 3	218 ± 4	3017 ± 1	0.4884 ± 0.0016	4570 ± 25	3137 ± 1	13918 ± 49	13777 ± 60
HH1-U25	238.0	140 ± 3	349 ± 7	3150 ± 2	0.5119 ± 0.0018	3248 ± 11	3277 ± 2	14130 ± 52	13958 ± 72
HH1-U37	238.3	173 ± 3	5549 ± 111	3666 ± 2	0.6238 ± 0.0026	308 ± 1	3816 ± 7	15370 ± 67	14148 ± 582
HH-U16	238.5	115 ± 2	1301 ± 26	3784 ± 1	0.6141 ± 0.0025	861 ± 3	3941 ± 3	14722 ± 63	14257 ± 207
HH1-U26	239.0	128 ± 3	1293 ± 26	3611 ± 1	0.6403 ± 0.0026	1004 ± 4	3773 ± 3	16002 ± 68	15566 ± 195
HH1-U27	240.5	120 ± 2	359 ± 7	3760 ± 1	0.6789 ± 0.0028	3595 ± 14	3938 ± 2	16456 ± 71	16280 ± 88
HH-U17	242.0	112 ± 2	468 ± 9	4161 ± 2	0.8376 ± 0.0033	3190 ± 13	4387 ± 2	18870 ± 79	18666 ± 104
HH1-U28	242.8	112 ± 2	572 ± 11	3952 ± 2	0.8850 ± 0.0033	2754 ± 10	4190 ± 2	20931 ± 85	20691 ± 120
HH1-U29	243.6	115 ± 2	361 ± 7	4229 ± 2	1.0361 ± 0.0035	5241 ± 17	4517 ± 3	23391 ± 86	23222 ± 99
HH-U18	243.9	137 ± 3	877 ± 18	3857 ± 3	1.0180 ± 0.0037	2534 ± 9	4135 ± 4	24882 ± 101	24597 ± 147
HH-U19	244.9	130 ± 3	281 ± 6	3224 ± 2	0.9214 ± 0.0036	6803 ± 27	3468 ± 2	26021 ± 111	25868 ± 119
HH-U20	254.7	131 ± 3	508 ± 10	3166 ± 2	0.9182 ± 0.0031	3750 ± 12	3408 ± 2	26322 ± 98	26100 ± 124
HH-U21	260.9	136 ± 3	463 ± 9	2835 ± 1	0.8750 ± 0.0031	4081 ± 14	3062 ± 2	27362 ± 107	27147 ± 129
UU-H11	262.4	122 ± 2	602 ± 12	3058 ± 1	0.9479 ± 0.0030	3056 ± 10	3308 ± 2	28071 ± 98	27804 ± 139
HH1-U30	263.8	121 ± 2	632 ± 13	3203 ± 1	1.0037 ± 0.0038	3042 ± 11	3471 ± 2	28753 ± 120	28481 ± 157
HH-U35	264.7	99 ± 2	827 ± 17	3946 ± 2	1.2800 ± 0.0040	2436 ± 8	4308 ± 3	31389 ± 110	31039 ± 175
HH1-U31	265.2	86 ± 2	386 ± 8	3697 ± 2	1.2442 ± 0.0044	4423 ± 15	4048 ± 3	32231 ± 129	32008 ± 150
HH-U22	266.8	101 ± 2	781 ± 16	3290 ± 2	1.1746 ± 0.0039	2418 ± 7	3613 ± 3	33492 ± 127	33134 ± 192
HH-U23	272.0	96 ± 2	487 ± 10	3488 ± 2	1.2826 ± 0.0044	4008 ± 13	3849 ± 3	35133 ± 137	34882 ± 164
HH-U24	280.2	121 ± 2	99 ± 2	3008 ± 2	1.2020 ± 0.0045	23362 ± 124	3341 ± 3	37161 ± 162	37058 ± 163
HH-U36	288.0	125 ± 2	187 ± 4	3014 ± 2	1.2210 ± 0.0050	12930 ± 50	3352 ± 3	37771 ± 178	37642 ± 181
UU-H12*	289.8	128 ± 3	1295 ± 26	2997 ± 2	1.1988 ± 0.0037	1886 ± 5	3324 ± 3	37173 ± 133	36701 ± 241
HH1-U32	302.8	133 ± 3	621 ± 12	2870 ± 2	1.2136 ± 0.0041	4119 ± 13	3203 ± 3	39140 ± 153	38877 ± 180
UU-H13	315.9	139 ± 3	680 ± 14	2856 ± 2	1.2674 ± 0.0043	4120 ± 14	3208 ± 3	41321 ± 166	41050 ± 194
UU-H14	348.8	135 ± 3	672 ± 14	2670 ± 2	1.2818 ± 0.0039	4095 ± 13	3025 ± 3	44396 ± 162	44113 ± 194
UU-H15	367.8	132 ± 3	223 ± 5	2660 ± 1	1.2991 ± 0.0039	12163 ± 59	3022 ± 2	45252 ± 160	45109 ± 164

Uncertainties are 2σ. Reported errors for ^{238}U and ^{232}Th concentrations are estimated to be ±1 % due to uncertainties in spike concentration; analytical uncertainties are smaller. Decay constants for ^{230}Th and ^{234}U are from (Cheng et al., 2013); decay constant for ^{238}U is 1.55125×10^{-10} yr^{-1} (Jaffey et al., 1971). All ages are relative to 1950. Corrected ages assume initial $^{230}Th/^{232}Th$ atomic ratio of 25 ± 12.5 ppm. *Date excluded from age model.

CHAPTER 3: A semi-quantitative estimate of sea-level-driven rainfall change in central Vietnam

3.1. Abstract

Changes in Southeast Asian autumn monsoon rainfall have broad-reaching impacts on the millions living in Mainland Southeast Asia. The variability of the autumn monsoon rainfall is poorly captured by climate models, making future predictions uncertain. Paleorecords, which help constrain past monsoon variability, show that changes in global sea level drove substantial and abrupt change in Southeast Asian autumn monsoon rainfall amount since the Late Pleistocene. However, the current hydroclimate record is qualitative, meaning changes in autumn rainfall amount are currently unquantified. Here we produce a semi-quantitative rainfall record using calcium isotopes ($\delta^{44}Ca$) in a speleothem from central Vietnam, a region dominated by the autumn monsoon. Our record estimates that autumn monsoon rainfall was 50 % lower during the Last Glacial Maximum, when sea level was low. Climate model simulations have a similar pattern to speleothem $\delta^{44}Ca$, but estimate a smaller 25 to 35 % reduction in autumn rainfall amount. While the significant uncertainties with the speleothem $\delta^{44}Ca$ proxy limit our interpretations, this reconstruction shows the promise of speleothem $\delta^{44}Ca$ records, particularly when used alongside climate model simulations.

3.2. Introduction

The Southeast Asian autumn monsoon (September-November) impacts millions of people along the eastern coast of Vietnam (Figure 3.1a) (Ramesh et al., 2021). Small changes to this highly seasonal phenomenon cause floods and droughts, which have devastating effects on the region's agriculture, infrastructure, and water availability (Du et al., 2018; Luu et al., 2020, 2021). Thus, understanding autumn rainfall variability in a changing climate is crucial for constraining the possible risks to this region.

Climate models fail to capture modern Southeast Asian autumn monsoon variability (Sengupta & Nigam, 2019), suggesting future projections of rainfall change remain uncertain. Paleoclimate records help bridge this gap by providing reconstructions of past monsoon variability. Even though paleorecords of the Southeast Asian autumn monsoon are limited, a recent study using the speleothem HH-1 from Hoa Huong cave in central Vietnam found that the autumn monsoon underwent significant, and at times abrupt, change over the last 45,000 years (Patterson et al., 2023). They demonstrated that changes in sea level, driven by global ice sheet volume, and the strength of the Atlantic Meridional Overturning Circulation drove autumn monsoon variability on centennial-millennial timescales. During some periods of rapid change (i.e. ice sheet melt during the deglaciation and Heinrich events), autumn rainfall amount abruptly shifted in a matter of decades. However, due to the current limitations of most speleothem hydroclimate proxies ($\delta^{18}O$, $\delta^{13}C$, Mg/Ca, and $\delta^{234}U_{initial}$), hydroclimate change in the HH-1 record was described qualitatively (i.e. "wetter" or "drier"). To better understand rainfall change in central Vietnam, we must move towards quantitative reconstructions, particularly during periods of abrupt change.

Calcium isotopes ($\delta^{44/40}Ca$, written as $\delta^{44}Ca$ from here on) are a promising new speleothem hydroclimate proxy (Johnson, 2021; Li et al., 2018; Reynard et al., 2011), which have been used to semi-quantitatively reconstruct rainfall amount (Magiera et al., 2019;

Owen et al., 2016; de Wet et al., 2021). The foundation of this method relies on the relatively simple calcium isotope systematics in cave environments and the relationship between speleothem δ^{44}Ca and prior calcite precipitation (PCP). Water infiltrating through the epikarst dissolves calcium from the host bedrock (Owen et al., 2016), which is then isotopically fractionated during calcite precipitation. PCP occurs when CO_2 degasses out of drip water in the epikarst or cave ceiling causing calcite to precipitate and certain isotopes/elements to be preferentially concentrated in the remaining drip water (Johnson et al., 2006). When calcite precipitates from this drip water onto a speleothem, the speleothem records this PCP geochemical signature. In the case of calcium isotopes, lighter isotopes (^{40}Ca) precipitate out of solution during PCP, leaving the remaining drip water rich in heaver isotopes (^{44}Ca) (Gussone et al., 2005; Tang et al., 2008). More PCP (high δ^{44}Ca) occurs during dry periods when infiltration is slower and more air is in the epikarst. Unlike other PCP-influenced proxies (e.g. Mg/Ca and δ^{13}C), which have a variety of climate and environmental controls (Fairchild & Treble, 2009; Fohlmeister et al., 2020), PCP primarily controls speleothem δ^{44}Ca values. Although other controls on calcite δ^{44}Ca include growth rate (Lemarchand et al., 2004; Reynard et al., 2011; Tang et al., 2008), temperature (Tang et al., 2008), and bedrock dissolution (de Wet et al., 2021), none of these controls are particularly strong, with most studies identifying PCP as the dominant control on their speleothem δ^{44}Ca record (Li et al., 2018; Magiera et al., 2019; Owen et al., 2016; Stoll et al., 2022; de Wet et al., 2021).

Using established geochemical relationships and modern cave δ^{44}Ca measurements, previous studies have used the strong relationship between PCP and speleothem δ^{44}Ca to quantify PCP amount (Li et al., 2018; Magiera et al., 2019; Owen et al., 2016; Stoll et al., 2022; de Wet et al., 2021). Then, assuming a relationship between PCP and rainfall, PCP is converted into rainfall amount. Since our understanding of the PCP-rainfall relationship remains rudimentary (Li et al., 2018), these reconstructions are referred to as semi-quantitative. Here, we generate a new δ^{44}Ca record from stalagmite HH-1 to estimate rainfall change in central Vietnam. First, we show that PCP is the primary control on HH-1 δ^{44}Ca. We then follow methods outlined in Owen et al. (2016) to reconstruct both PCP and rainfall amount. Our semi-quantitative reconstruction shows that rainfall from the Southeast Asian autumn monsoon changed substantially over the last 45,000 years, particularly in response to changes in sea level.

3.2.1. Study site and sample description

Hoa Huong cave is located in Phong Nha-Ke Bang National Park in central Vietnam (17.5°N, 106.2°E; Elev. 411 m) and receives the majority of its annual rainfall during autumn (~47 % from September – Novermber versus ~30 % from June – August (Patterson et al., 2023)), making this cave ideally situated to record Southeast Asian autumn monsoon variability (Figure 3.1a,b). Collected from Hoa Huong cave in March 2020, HH-1 is a 3.7 m-long previously broken stalagmite that grew continuously from 45 – 4 ka (Figure 1.2). HH-1 is a well-suited speleothem for δ^{44}Ca-PCP-rainfall reconstruction because previous work on the sample found that PCP strongly influenced the δ^{13}C and Mg/Ca hydroclimate records (Patterson et al., 2023). This indicates that 1) PCP is present in the HH-1 record, and 2) HH-1 δ^{44}Ca will likely record this same PCP-driven hydroclimate signal.

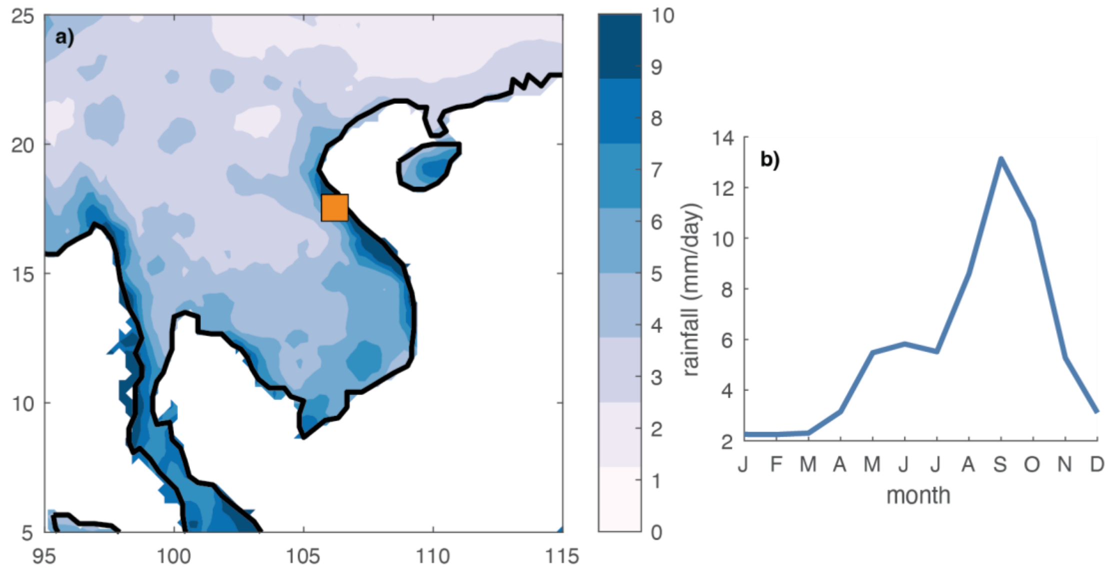

Figure 3.1. Study site. a) Map of SON (September, October, and November) rainfall in Mainland Southeast Asia derived from Asian Precipitation-Highly Resolved Observational Data Integration Towards Evaluation (APHRODITE) from 1951-2007 (Yatagai et al., 2012). The orange square denotes location of Hoa Huong cave. b) Seasonal cycle of APHRODITE rainfall from grid cell nearest the study site.

3.3. Methods

3.3.1. δ^{44}Ca analyses

We drilled 89 samples from the central growth axis of stalagmite HH-1 and one limestone bedrock sample from Hoa Huong Cave using a handheld rotary tool with a diamond bur. No drip water or modern calcite have been analyzed for δ^{44}Ca. We conducted all δ^{44}Ca analyses at Princeton University following the protocol in (Blättler & Higgins, 2017). Approximately 5 mg of sample was dissolved overnight in 2 mL concentrated (16N) HNO_3, dried down on a hotplate and re-dissolved in 5 mL 0.2 % HNO_3. To isolate calcium from other cations we used an automated ion chromatography system (Thermo Dionex IC-5000$^+$) with methanosulfonic acid as the eluent and a CS16 5 × 250 mm cation-exchange column (Blättler & Higgins, 2014).

δ^{44}Ca measurements were made on a Thermo Scientific Neptune Plus multi-collector inductively coupled plasma mass spectrometer (MC-ICP-MS) coupled with an ESI Apex-IR inlet system (Blättler & Higgins, 2017; Husson et al., 2015). Measurements were carried out at medium resolution to avoid $ArHH^+$ interferences. All Ca isotope data are reported in delta notation relative to seawater ($\delta^{44/40}Ca_{seawater}$ = 0‰), where

$$\delta^{44/40}Ca = (^{44}Ca/^{40}Ca_{sample} / ^{44}Ca/^{40}Ca_{seawater} - 1) * 1000$$

Due to isobaric inferences with ^{40}Ar, we are unable to directly measure ^{40}Ca and instead measure ^{42}Ca. Measured $\delta^{44/42}$Ca values are converted to $\delta^{44/40}$Ca assuming mass dependent fractionation with a slope of 2.05 and no excess radiogenic ^{40}Ca (Fantle & Tipper, 2014). Corrections are made for isobaric Sr^{2+} interferences by using measurements at m/z = 43.5, for doubly charged $^{87}Sr^{2+}$. Mass dependence is verified using a triple isotope plot ($\delta^{44/42}$Ca vs. $\delta^{44/43}$Ca) and all measured data fall along a slope of 0.51, similar to the 0.507 slope predicted by the exponential mass-dependent fractionation law. The long-term external reproducibility of $\delta^{44/40}$Ca values is estimated through the repeat purification and isotopic analyses of SRM915b (for $\delta^{44/40}$Ca values). Our measured values of -1.17±0.14 ‰ (2σ, n = 24) for SRM915b agree well with reported values of -1.16±0.08 ‰(Heuser & Eisenhauer, 2008) and -1.13±0.04 ‰ (Jacobson et al., 2015). For samples purified and analyzed once, we report the uncertainty as our long-term external reproducibility. When samples are purified and analyzed multiple times, we report the standard error of the mean.

3.3.2 iTRACE

iTRACE is a water isotope enabled transient simulation of the last deglaciation (11-20ka) (He et al., 2021). iTRACE simulations are performed in iCESM1.3 (Brady et al., 2019), which is comprised of Community Atmosphere Model version 1.3 (CAM5.3), the Community Land Model version 4 (CLM4), Parallel Ocean Program version 2 (POP2), and Los Alamos Sea Ice Model version 4 (CICE4). The resolution of the land and atmosphere is 1.9°x2.5° (latitude and longitude) with 30 vertical levels in the atmosphere. iCESM 1.3 simulations are well validated against modern observations of global precipitation and precipitation isotopes (Brady et al., 2019; Nusbaumer et al., 2017; T. E. Wong et al., 2017). The analyses in this study use the fully forced simulations which include changing continental ice sheets based on ICE-6G model (Peltier et al., 2015), KMT ocean bathymetry, orbital forcing, greenhouse gas concentrations from ice core records (Lüthi et al., 2008; Petit et al., 1999; Schilt et al., 2010) and meltwater fluxes following TRACE-21ka (Liu et al., 2009). The ice sheet configuration changes in 1,000 year increments and ocean bathymetry is modified twice at 14 ka and 12 ka based on changes in global sea level from the ICE-6G model (Figure S5 in *Appendix B*). See Patterson et al. (2023) for further information about iTRACE and model validation in central Vietnam.

3.4. Results

HH-1 δ^{44}Ca values are variable and range from -2.28 ‰ to -1.16 ‰ (Figure 3.2b). The record oscillates between periods of low δ^{44}Ca (~-1.88 +/- 0.2 ‰: 45 – 37 ka, 30 – 25 ka, 16 ka, and 14 – 4 ka) and high δ^{44}Ca (~-1.34 +/- 0.1‰; 30 ka and 25 – 14 ka). Of the high periods, δ^{44}Ca values are the most variable from 14 – 4 ka. Except for an increasing trend from 35 – 30 ka, the transition between these low/high periods are relatively abrupt. The overall pattern of HH-1 δ^{44}Ca variability is similar to other HH-1 proxies including Mg/Ca and δ^{13}C (Figure 3.2 c). In fact, the HH-1 δ^{44}Ca positively correlates with both records (r(Mg/Ca) = 0.75, $p < 0.01$ and r(δ^{13}C) = 0.64, $p < 0.01$).

We also examine well-known periods of abrupt change including Heinrich Stadials 1-4 and the Younger Dryas. Heinrich Stadials 1, 2, and 4 occur during periods of high δ^{44}Ca, whereas the YD and HS3 occur during periods of low δ^{44}Ca. HS1 and HS3 show small positive excursions, whereas HS2 and HS4 do not show an obvious positive or negative excursion. While δ^{44}Ca values are relatively stable through the Heinrich Stadials, δ^{44}Ca is much more variable during the YD.

The δ^{44}Ca value of the limestone bedrock from Hoa Huong Cave is -1.07 ‰, higher than all HH-1 stalagmite measurements.

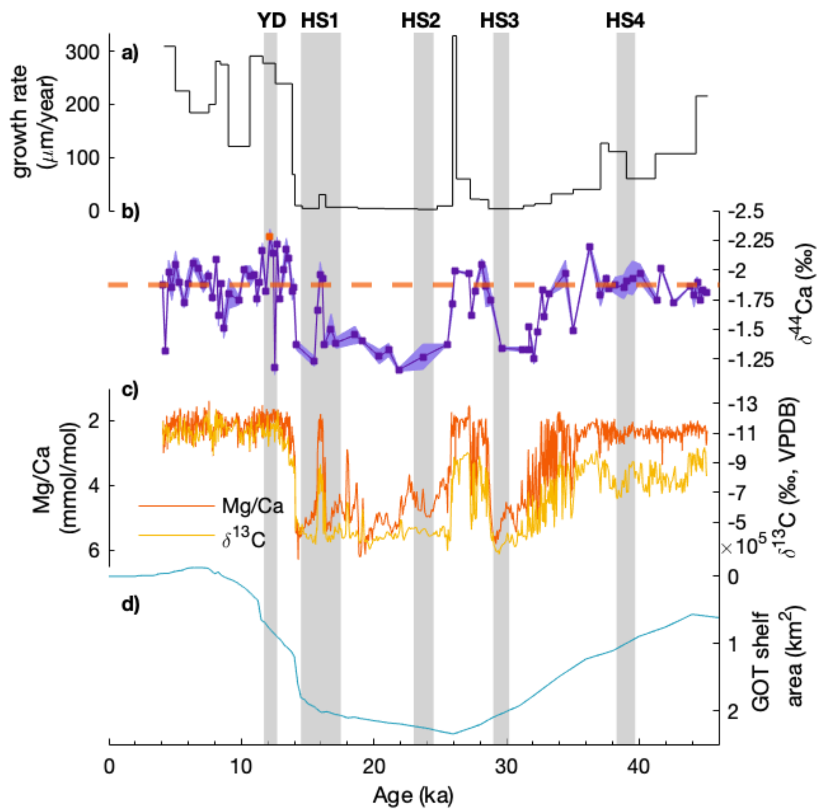

Figure 3.2. Timeseries of HH-1 proxies and sea level from 45 – 4 ka. a) HH-1 growth rate (solid black), b) HH-1 δ^{44}Ca with 1σ error (purple). Dashed orange line shows f = 1 value used for α_{mean}, and orange dot denotes the f = 1 value used for α_{min}. c) HH-1 Mg/Ca (orange) and δ^{13}C (yellow), d) Gulf of Tonkin (GOT) shelf exposure history (blue). Grey shading denotes the YD and Heinrich Stadials 1-4. The Mg/Ca, δ^{13}C, and GOT curves are from Patterson et al. (2023).

3.5. Discussion

3.5.1 Controls on stalagmite δ^{44}Ca

The strong correlations between δ^{44}Ca and the other HH-1 proxies (Mg/Ca and δ^{13}C) suggests that the same mechanism controls all three proxies (Figure 3.2). Previous work from Patterson et al. (2023) found that PCP primarily drives HH-1 δ^{13}C and Mg/Ca. Since PCP is a well-known control of speleothem δ^{44}Ca (Li et al., 2018; Magiera et al., 2019; Owen et al., 2016; Reynard et al., 2011; de Wet et al., 2021), the similarity between HH-1 the δ^{44}Ca and the PCP-driven proxies strongly indicates that PCP also drives δ^{44}Ca variability.

Crucially, the δ^{44}Ca record shares some common features with the Mg/Ca record (the strongest indicator of PCP), including relatively stable, low values from 45 – 37 ka and 30 – 35 ka (Figure 3.2b,c). In the Mg/Ca record, the stability of these periods defines a threshold where conditions are too wet for PCP to occur (PCP = 0) (Patterson et al., 2023). These shared low threshold features in the δ^{44}Ca record further corroborate our interpretation of δ^{44}Ca as proxy of PCP. One notable difference between the δ^{44}Ca and Mg/Ca records is the variability from 14 – 4 ka in the δ^{44}Ca record, an additional low threshold period in the Mg/Ca record. This discrepancy suggests that other factors may influence δ^{44}Ca and/or δ^{44}Ca is more sensitive to changes in PCP than Mg/Ca during this period.

Another known control of calcite δ^{44}Ca is growth rate (Lemarchand et al., 2004; Reynard et al., 2011; Tang et al., 2008). In the HH-1 record, periods of high growth rate generally correspond to lower δ^{44}Ca values, but this relationship is not consistent (Figure 3.2). HH-1 δ^{44}Ca does not linearly track changes in growth rate, particularly from 37 – 45 ka and 14 – 4 ka. Additionally, changes in growth rate alone cannot explain the full variability of the HH-1 δ^{44}Ca record. Tang et al. (2008) found that a 1000 % increase in growth rate causes a ~0.22 ‰ decrease in calcite δ^{44}Ca at 25 °C. Even though growth rate is highly variable in the HH-1 record (2-309 μm/year, Figure 3.2a), changes in growth rate are not large enough to solely cause many of the large shifts in δ^{44}Ca. For example, the 0.56 ‰ positive excursion at ~16.1 ka only corresponds to a 400 % change in growth rate. Using the relationship from Tang et al. (2008), this would only account for 0.09 ‰ of this 0.56 ‰

shift and is smaller than the 0.14 ‰ uncertainty of the $\delta^{44}Ca$ measurements. Furthermore, many shifts in growth rate also co-occur with changes in the PCP-driven proxies (Mg/Ca and $\delta^{13}C$), making the effects of PCP-driven vs growth rate-driven change difficult to differentiate. While growth rate could influence the HH-1 $\delta^{44}Ca$ record, the striking resemblance between $\delta^{44}Ca$ and the PCP-driven proxies strongly indicates that PCP is the dominant driver of $\delta^{44}Ca$ variability.

Following the findings of the HH-1 PCP-driven proxies in Patterson et al. (2023), we interpret HH-1 $\delta^{44}Ca$ as a record of Southeast Asian autumn monsoon rainfall. Patterson et al. (2023) found that ice sheet-modulated sea-level change, specifically the inundation/exposure of the Gulf of Tonkin and the South China Shelf, was the primary driver of autumn rainfall variability over the last 45,000 years. In central Vietnam, wetter conditions occurred during sea-level highstands (flooded Gulf of Tonkin and the South China Shelf) and drier conditions occurred during sea-level lowstands (exposed Gulf of Tonkin and the South China Shelf). The HH-1 $\delta^{44}Ca$ record follows this expected pattern with low values (low PCP, wet conditions) occurring during the sea-level highstands from 45 – 37 ka and 14 – 4 ka, and predominantly high values (high PCP, dry conditions) occurring during the sea-level lowstand from 30 – 14 ka (Figure 3.2b,d). We note that the negative (wet) excursions from 30 – 25 ka and at 16 ka, which are present in all HH-1 hydroclimate proxies, do not follow changes in sea level. Instead, the 30 – 25 ka excursion likely reflects the two wet Dansgaard–Oeschger events that occur during this time period, whereas the mechanism driving the 16 ka event is currently unexplained (Patterson et al., 2023).

A smaller control on the Southeast Asian autumn monsoon is meltwater events in the North Atlantic (the Younger Dryas and Heinrich Stadials), where the cascading effects of weakened Atlantic Meridional Circulation drives the formation of an anomalous anticyclone in the western Pacific during autumn, causing dry conditions in MSEA (He et al., 2021; Patterson et al., 2023). The positive excursions during HS1 and HS3 in the HH-1 δ^{44}Ca record are consistent with this mechanism and HH-1 Mg/Ca and δ^{13}C records (Figure 3.2). Although the response to these events is inconsistent; there are no obvious negative excursions during the YD, HS2, or HS4. Notably, the other HH-1 proxies also show variable responses to meltwater events. Since the magnitude of these excursions is much smaller than the hydroclimate response to sea level change, it is possible that the δ^{44}Ca proxy and other the PCP-driven proxies are not sensitive enough to detect these changes.

Because the HH-1 δ^{44}Ca record closely follows changes in other HH-1 proxies, we do not further interpret the climate forcings driving changes in hydroclimate. Instead, we choose to utilize the δ^{44}Ca record to quantify changes in PCP and create a semi-quantitative reconstruction of regional rainfall. We explore these relationships next.

3.5.2 Reconstructing PCP from δ^{44}Ca

To reconstruct PCP from δ^{44}Ca values, we follow methods outlined in Owen et al. (2016), and used in several other studies (Li et al., 2018; Magiera et al., 2019; de Wet et al., 2021). For each speleothem δ^{44}Ca measurement, we calculate the amount of Ca dissolved from the host rock that remains in solution (*f*), which is a Rayleigh fractionation process that occurs during PCP and can be described by the following equation.

$$f = \left(\frac{r_s}{\alpha * r_o}\right)^{\left(\frac{1}{\alpha-1}\right)}$$

(1)

The r_s and r_0 terms represent the $^{44}Ca/^{40}Ca$ ratio ($r = \delta/1000 + 1$) of precipitated calcite and initial drip water (which is assumed to be the same as the bedrock), respectively. The α term is a site-specific fractionation factor between water and calcite ($\alpha = (1000 + \delta^{44}Ca_{calcite}) / (1000 + \delta^{44}Ca_{dripwater})$). Ideally, α is calculated with paired measurements of drip water and modern calcite from the feeder drip above the sample. However, there is no active drip above HH-1. Other studies faced similar challenges and instead calculated α using measurements from other drip sites in the same cave system (Magiera et al., 2019; de Wet et al., 2021). However, the α between drip sites may vary (de Wet et al., 2021), demonstrating that this method may not always produce a suitable fractionation factor. Values of *f* range from 0 to 1, where a value of 1 occurs when no Ca precipitates out of the solution (no PCP) and 0 occurs when all Ca precipitates out of the solution (100% PCP).

Since we do not have $\delta^{44}Ca$ drip water and modern calcite measurements from Hoa Huong cave, we estimated α with a different method. We first identified portions of the HH-1 $\delta^{44}Ca$ record where no PCP occurs ($f = 1$). Then, assuming $f = 1$ and $r_0 = \delta^{44}Ca$ of the bedrock (-1.07 ‰), we approximated a site-specific fractionation factor by solving for α in equation (1). We calculated two different fractionation factors, $\alpha_{min} = 0.99879$ and $\alpha_{mean} = 0.99920$. For α_{min}, we assume that the minimum value in the HH-1 $\delta^{44}Ca$ record ($r_s = -2.28$ ‰, red point in Figure 3.2b) undergoes no PCP ($f = 1$). For α_{mean}, we took the mean $\delta^{44}Ca$ value from 4 – 14 ka and 35 – 45 ka ($r_s = -1.88$ ‰, dashed line in Figure 3.2b), periods in the HH-1 record where PCP-driven proxies (δ^{44}Ca, Mg, and δ^{13}C) all reach a lower threshold (indicating little to no PCP was occurring). Ultimately, α_{min} is a conservative estimate, whereas the α_{mean} uses information from multiple proxies to constrain PCP. Notably, both fractionation factors fall within the range calculated by other studies, α = 0.9987 – 0.99934 (Magiera et al., 2019; Owen et al., 2016; de Wet et al., 2021).

Using these α values, we derived f for each speleothem δ^{44}Ca measurement using equation (1), creating two different time series of PCP (Figure 3.3). The time series vary identically, but have a different range. The α_{min} time series ranges from 0.39 to 1, whereas the α_{mean} time series has a larger range from 0.41 to 1.66. Around 40% of the values from the α_{mean} time series are above f = 1 (Figure 3.3b). Because these values are theoretically impossible, we treat all values of f > 1 the same as values of f = 1 (i.e. no PCP). As values of f decrease, the two time series converge (Figure 3.3a), with the lowest values in each reconstruction being quite similar. This similarity increases our confidence of low estimates of PCP. For this reason, we will focus the analyses of the semi-quantitative reconstruction of rainfall on large shifts in the hydroclimate record, rather than variability during the wetter periods.

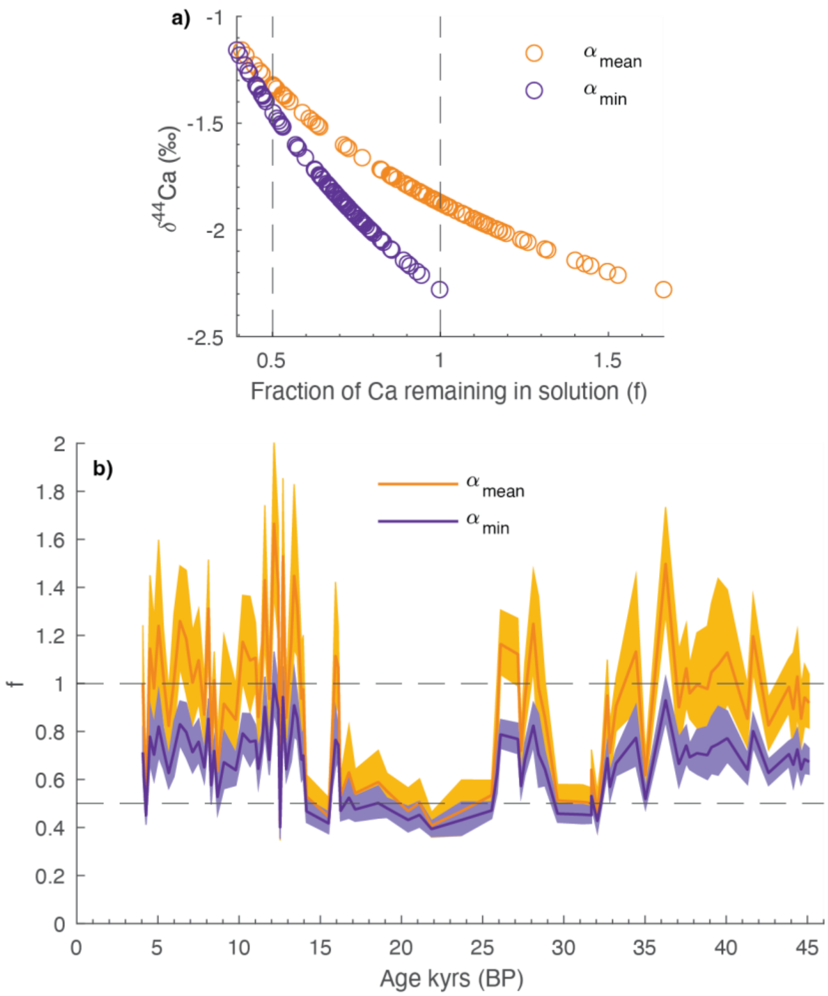

Figure 3.3. HH-1 PCP reconstruction. a) Scatter plot speleothem δ^{44}Ca and the fraction of calcium remaining in solution (*f*) calculated from equation (1) using α_{mean} (orange) and α_{min} (purple). b) Timeseries of *f* using α_{mean} (orange) and α_{min} (purple) with 1σ shading. Dashed horizontal lines denote *f* = 1 (no PCP) and *f* = 0.5 (50 % PCP).

3.5.3. Semi-quantitative rainfall change in central Vietnam

We next convert PCP (*f*) to rainfall amount assuming a linear relationship between rainfall amount and *f* (Equation 2)(Owen et al., 2016). Since the linear relationship between PCP and rainfall has not been extensively tested, like other studies (Magiera et al., 2019; Owen et al., 2016; de Wet et al., 2021), we interpret our results as a semi-quantitative reconstruction of rainfall.

$$P_{paleo} = \left(\frac{P_{modern} * f_{paleo}}{f_{modern}}\right)$$

(2)

Here, P represents total annual precipitation and f is from equation (1). P_{modern}, average annual rainfall at the study site, is 1.67 m/year (1951-2007) (Yatagai et al., 2012). Since we lack the monitoring data to calculate a modern f value, we assume f_{modern} is similar to the average value during the Holocene. Using this method, α_{min} and α_{mean} produce the same results. For the sake of simplicity, we calculate a single P_{paleo} time series using the α_{mean}-derived time series where f_{modern} = 1. The resulting precipitation time series ranges 0.68 – 2.78 m/year (Figure 3.4a).

Due to uncertainties in our interpretation of HH-1 δ^{44}Ca variability (e.g. variability during the Holocene) and propagated analytical uncertainty (average standard deviation = +/- 0.28 m), we focus our discussion on the large sea-level driven changes to local rainfall. Our record indicates that rainfall amount was similar to modern levels during both sea-level highstands (Figure 3.3a). During the sea-level lowstand, annual rainfall decreased by ~50 %. Interestingly, a study using a pollen record from the continental shelf in the north South China Sea, proposed a similar 50 % reduction in rainfall during the Last Glacial Maximum, ~20 ka (Kershaw et al., 2001). However, the absence of (semi-)quantitative paleoclimate records of rainfall change in Southeast Asia make additional comparisons impossible.

To further test whether this 50 % decrease in annual rainfall is reasonable, we compare these findings to iTRACE, an isotope enabled transient climate model simulation of the deglaciation, 20 – 11 ka (see *Methods*). Previous work using iTRACE found that the model correctly captures changes in central Vietnam rainfall, including the sea-level driven increase in autumn rainfall at 14 ka (Patterson et al., 2023). Notably, we compare our HH-1 rainfall reconstruction to relative changes in iTRACE autumn (SON) rainfall rather than annual rainfall amount (Figure 3.4). This is because iTRACE simulations overestimate summer rainfall in central Vietnam, which results in iTRACE 1) overestimating total annual rainfall (see Figure S1g in *Appendix B*) and 2) muting the sea-level driven change in the annual rainfall time series (Figure 3.5). iTRACE simulations reveal SON rainfall increased ~25 % from the sea level lowstand (20 – 15 ka) to the Bolling Allerod (15 – 14 ka) and increased ~35 % when compared to the early Holocene (11.1 – 11 ka). While these numbers are lower than the 50% value from the HH-1 record, they still suggest that local sea-level rise at 14 ka substantially increased rainfall in central Vietnam.

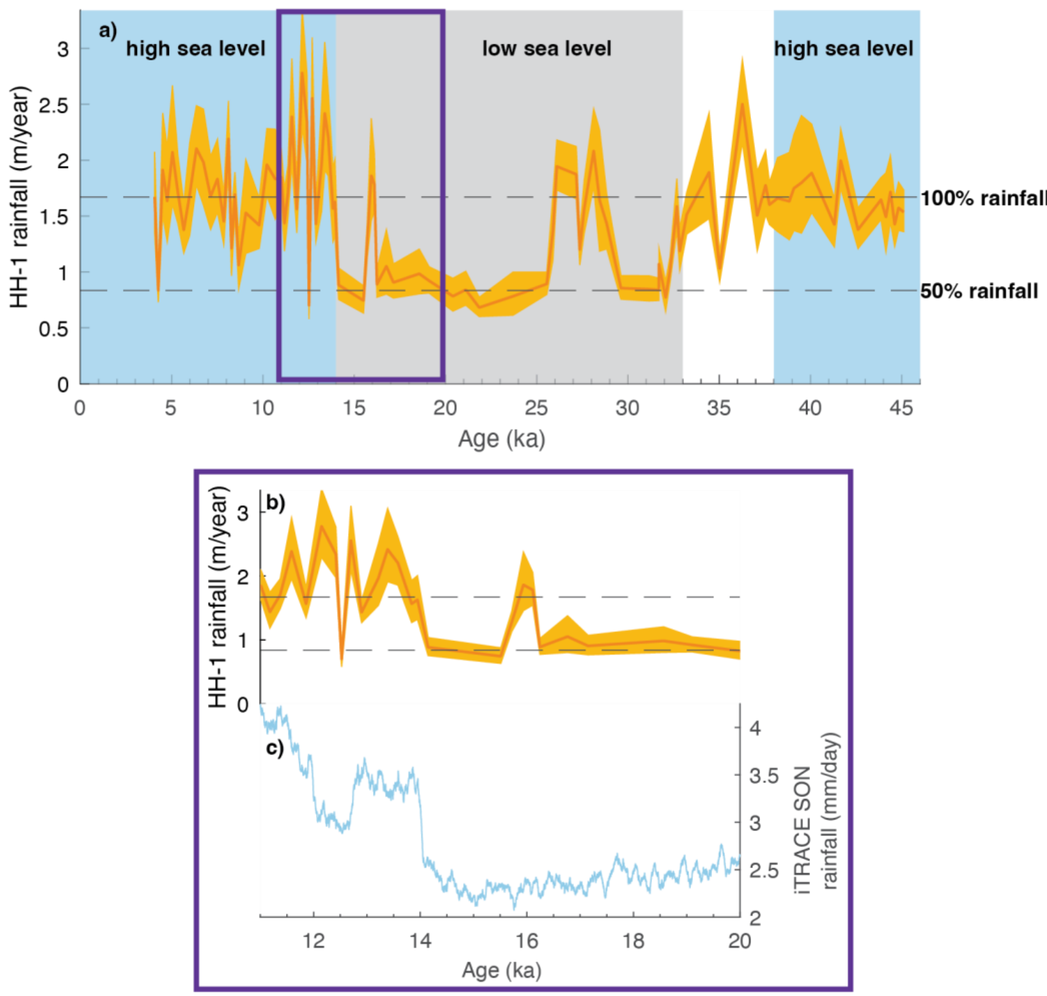

Figure 3.4. HH-1 rainfall reconstruction and climate model output. a) Timeseries of rainfall with 1σ shading reconstructed from equation (2). Horizontal dashed lines show 100 % modern rainfall (1.67 m/yr) and 50% modern rainfall (0.84 m/yr). Shaded regions denote periods of high and low sea level. b) Same as (a), but from 20 – 11 ka. c) iTRACE SON precipitation from the grid cell encompassing the study site. We smoothed the iTRACE time series with a 100 yr running mean for aesthetic purposes and readability.

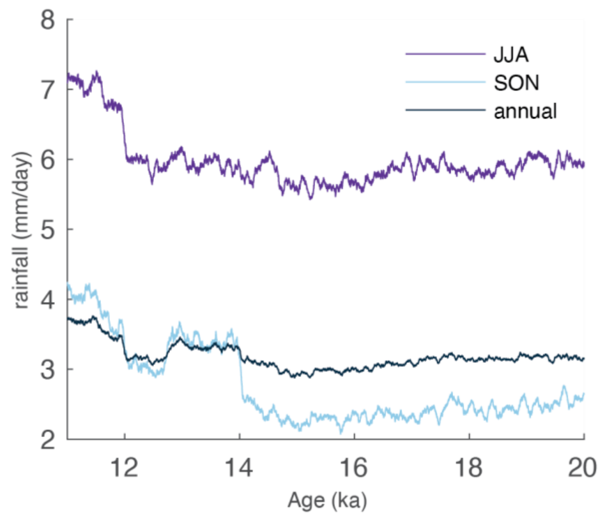

Figure 3.5. Time series of simulated iTRACE precipitation. Mean JJA (purple), SON (light blue) and annual (dark blue) precipitation.

3.6. Conclusions

Our new speleothem δ^{44}Ca records adds to the growing number of studies utilizing this semi-quantitative rainfall proxy. Through multiproxy comparison, we show that PCP is the primary driver of the HH-1 δ^{44}Ca record. This adds confidence to our PCP and rainfall amount reconstructions. Our findings also highlight some limitations of speleothem δ^{44}Ca. Without a better understanding of modern δ^{44}Ca systematics in Hoa Huong cave, we cannot constrain an appropriate fractionation factor, which makes calculations of *f*, and thus PCP, less certain. Additionally, much work remains to determine whether a linear relationship between PCP and rainfall is appropriate, particularly over long timescales (de Wet et al., 2021).

Nevertheless, the similarities between the δ^{44}Ca-based and model-based rainfall reconstructions are promising. Combined model and speleothem results estimate that autumn rainfall in central Vietnam may have increased by as much as 25 to 50 % in a matter of decades during the deglaciation. While additional analyses (both model and geochemical) are necessary to further constrain this value, these findings suggest that the Southeast Asian autumn monsoon is capable of significant change in relatively short periods of time.

CHAPTER 4: Exploring and removing the influence of prior calcite precipitation on speleothem oxygen isotopes in Southeast Asia

Supporting information located in Appendix C.

4.1. Abstract

Prior calcite precipitation (PCP), an in-cave process known to impact speleothem proxy records, is a widely ignored control of speleothem oxygen isotopes ($\delta^{18}O$). Given that $\delta^{18}O$ is the most commonly measured speleothem proxy, understanding the effects of PCP could have far-reaching implications for numerous existing and future records. In this study, we investigate the effects of PCP on a stalagmite $\delta^{18}O$ record from central Vietnam, spanning 45 – 4 ka. Through a multiproxy comparison, we demonstrate that PCP is the primary driver of speleothem $\delta^{18}O$ variability, rather than the $\delta^{18}O$ of precipitation ($\delta^{18}O_p$). To illustrate the impact of PCP, we employ a geochemical model that utilizes speleothem Mg/Ca data and cave environment measurements to remove the PCP signal from the $\delta^{18}O$ record. The resulting corrected record exhibits substantially improved agreement with regional speleothem $\delta^{18}O$ records and climate model simulations, suggesting that the corrected record better reflects $\delta^{18}O_p$. By utilizing this corrected record to interpret changes in central Vietnam $\delta^{18}O_p$, we find that meltwater events in the north Atlantic are the primary driver of $\delta^{18}O_p$ during the Late Pleistocene. However, the drivers of $\delta^{18}O_p$ during the Holocene remain uncertain. Crucially, without considering the effects of PCP, our interpretations of the $\delta^{18}O$ record would have been misleading. To avoid misinterpretations of speleothem $\delta^{18}O$, our results emphasize the necessity of considering

PCP as a significant driver of speleothem $\delta^{18}O$, which can be diagnosed through comparisons to other PCP-sensitive proxies (e.g. trace elements and $\delta^{13}C$). Doing so will improve the accuracy of speleothem $\delta^{18}O$ reconstructions and thus, refine our understanding of past climate change.

4.2. Introduction

While oxygen isotope ($\delta^{18}O$) records from speleothems are widely used to reconstruct past climate variability, the effects of karst and in-cave processes on speleothem $\delta^{18}O$, such as prior calcite precipitation (PCP), have been largely overlooked. Currently, the interpretation of most speleothem $\delta^{18}O$ records relies on the well-established links between $\delta^{18}O$ and climate. When precipitated under equilibrium conditions, the primary controls on the $\delta^{18}O$ of speleothem calcite are cave temperature and drip water $\delta^{18}O$, which typically reflects the $\delta^{18}O$ of precipitation ($\delta^{18}O_p$) falling above the cave (Lachniet, 2009). In reality, karst and in-cave processes also affect $\delta^{18}O$ (Hendy, 1971; Mickler et al., 2006; Treble et al., 2022), resulting in the disequilibrium precipitation of most speleothem calcites (Daëron et al., 2019). PCP, a well-known process in karst systems (Fairchild et al., 2000), has long been thought to have no significant impact on speleothem $\delta^{18}O$. However, a recent modeling study challenged this assumption and demonstrated that PCP can theoretically offset speleothem $\delta^{18}O$ by several permil (‰) (Deininger et al., 2021). This finding raises concerns that PCP could potentially obscure climate-driven speleothem $\delta^{18}O$ variability. Consequently, without accounting for the effects of PCP, speleothem $\delta^{18}O$ records could be susceptible to misinterpretation. Given the multitude of published speleothem $\delta^{18}O$ records worldwide (Comas-Bru et al., 2020), it becomes paramount to explore the viability of this theory.

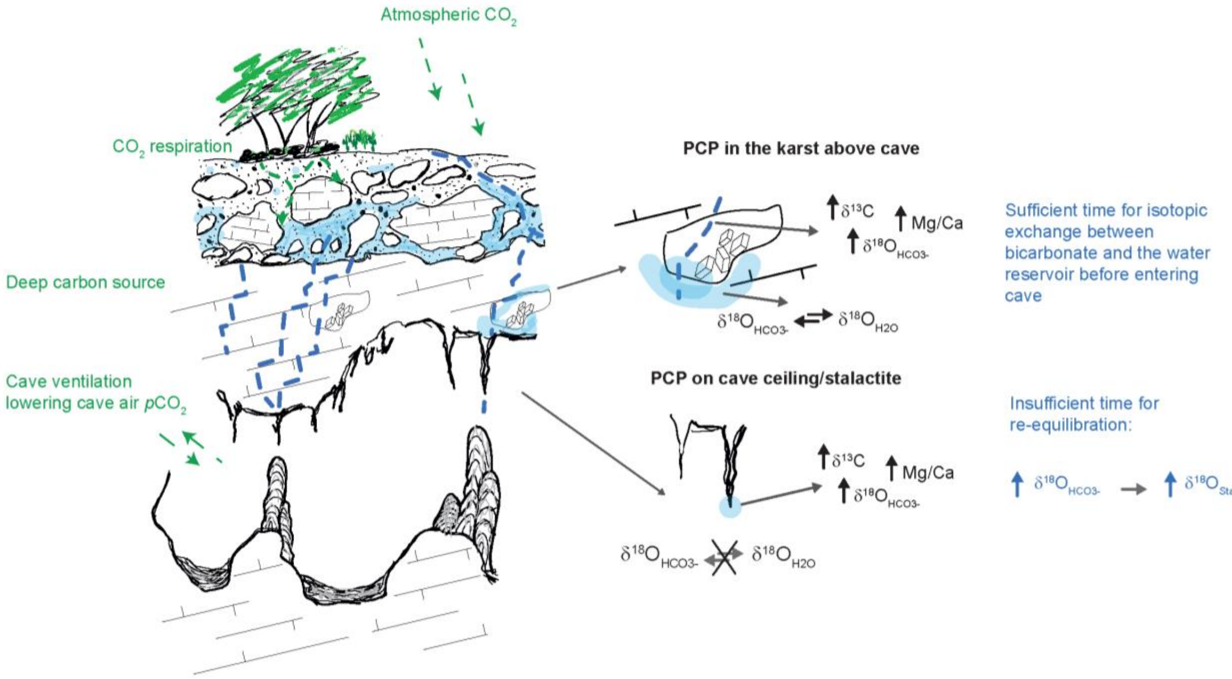

Figure 4.1. Schematic of PCP in a cave system. The left panel shows the flow path of drip water and calcite precipitation of along the infiltration pathway. The right panel shows detailed change in isotopes ($\delta^{18}O$ and $\delta^{13}C$) and trace elements (Mg/Ca) during PCP in the epikarst vs the cave ceiling.

PCP occurs when CO_2 degasses from the drip water prior to speleothem precipitation, resulting in calcite precipitation in the epikarst or on the cave ceiling/stalactite (Figure 4.1) (Johnson et al., 2006). During PCP, lighter isotopes (^{12}C and ^{16}O) preferentially degas, enriching the remaining drip water HCO_3^- pool in heavier isotopes (^{13}C and ^{18}O). Laboratory experiments simulating this process show that the calcite that precipitates from this pool of HCO_3^- reflects this enriched isotopic signature (higher $\delta^{13}C$ and $\delta^{18}O$ values) (Hansen et al., 2019; Polag et al., 2010). Similarly, Mg^{2+} and other trace elements with a partition coefficient < 1 are preferentially excluded during calcite precipitation (Fairchild & Treble, 2009), increasing alongside $\delta^{18}O$ in the remaining solution. Dry conditions enhance PCP because more air in the epikarst and slower infiltration rates increases CO_2 degassing, accumulating heavier isotopes and trace elements in the drip water (higher $\delta^{18}O$, $\delta^{13}C$, and Mg/Ca). Thus, PCP reflects local hydroclimate change.

While PCP is a well-known control of speleothem $\delta^{13}C$ and Mg/Ca records (Griffiths et al., 2020; Patterson et al., 2023; Wright et al., 2023), it is not generally considered to affect speleothem $\delta^{18}O$. Traditionally, H_2O exchange, the isotopic re-equilibration between HCO_3^- and H_2O, was thought to eliminate the PCP signal from drip water $\delta^{18}O$ before speleothem formation. With enough time, H_2O exchange reestablishes the initial pre-PCP $\delta^{18}O$ value of the drip water HCO_3^- pool, erasing the PCP signature (Hendy, 1971). However, several laboratory and modeling experiments found that H_2O exchange takes much longer than previous estimates (Beck et al., 2005; Dreybrodt, 2008; Scholz et al., 2009). Using these new estimates, a recent modeling study demonstrated that speleothem $\delta^{18}O$ does preserve a PCP signal when H_2O isotopic re-equilibration is incomplete (Deininger et al., 2021). Importantly, they suggest that incomplete H_2O exchange is more likely to occur during PCP on the cave ceiling/stalactite rather than in the epikarst. This is because the residence time of drip water in the epikarst far exceeds the time necessary for re-equilibration, whereas the residence time of drip water on the cave ceiling or stalactite may be sufficiently short to maintain isotopic disequilibrium during calcite precipitation.

Although geochemical models successfully simulate the effects of PCP on calcite $\delta^{18}O$, these effects have not been widely investigated in speleothem $\delta^{18}O$ records. Here we examine the impact of PCP on a previously published $\delta^{18}O$ record from central Vietnam

(Patterson et al., 2023). Using a geochemical model to remove the PCP signal from the speleothem $\delta^{18}O$ record (see *Methods*), we demonstrate that PCP overprints the expected $\delta^{18}O_p$ signal in the record. After removing the PCP signal, the corrected $\delta^{18}O$ record shows improved agreement with regional $\delta^{18}O$ speleothem records and climate model output, revealing a more realistic reflection of $\delta^{18}O_p$ from our record.

4.3. Results/Discussion

4.3.1. Controls on central Vietnam $\delta^{18}O_p$ and stalagmite $\delta^{18}O$

In this study we use a 3.7m long previously broken stalagmite (HH-1) collected from Hoa Huong cave in Phong Nha-Ke Bang National Park in central Vietnam (Figure 1.2, S1a; 17.5°N, 106.2°E). HH-1 grew continuously from 45 – 4 ka, and was previously used to investigate local hydroclimate change in central Vietnam (Patterson et al., 2023). We use the published HH-1 stable isotope records (768 $\delta^{18}O$ and $\delta^{13}C$ samples, ~50 year resolution) and Mg/Ca record (1,385 Mg/Ca samples, ~30 year resolution) (Figure 4.2), as well as monitoring data from Hoa Huong cave to conduct our analyses. To interpret the HH-1 $\delta^{18}O$ record we first review the controls on $\delta^{18}O_p$ in central Vietnam.

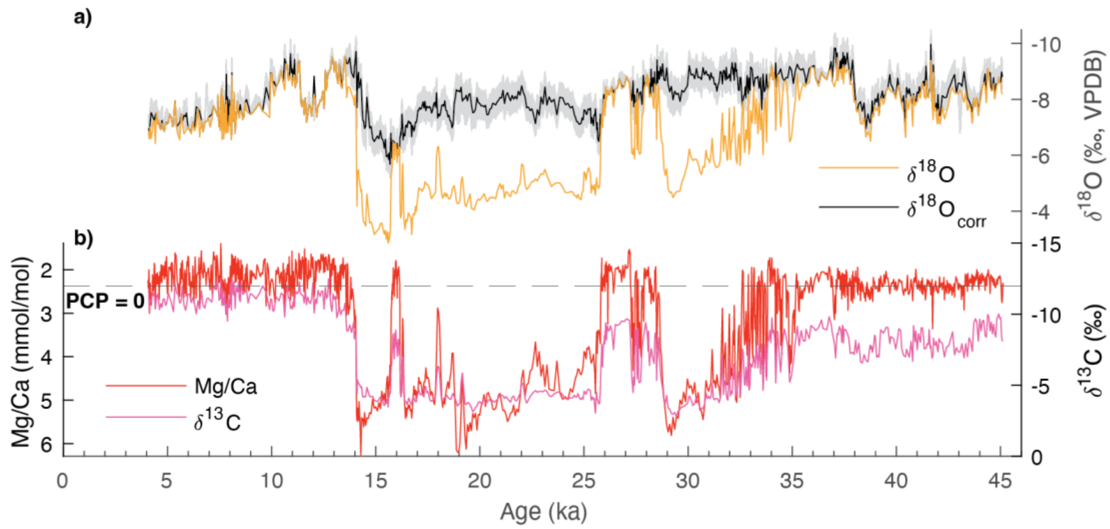

Figure 4.2. HH-1 proxies from 45 – 4 ka. a) HH-1 $\delta^{18}O$ (orange) and corrected $\delta^{18}O$ ($\delta^{18}O_{corr}$, black). Grey shading denotes 1 sigma error of the correction. b) HH-1 Mg/Ca (red) and $\delta^{13}C$ (pink). Black dashed line shows Mg/Ca threshold used to denote 0 PCP or Mg/Ca_0 (see *Methods*).

We expect HH-1 $\delta^{18}O$ to record weighted annual mean $\delta^{18}O_p$, which reflects the rainfall climatology in central Vietnam. Central Vietnam receives the majority of its annual rainfall from the northeast autumn monsoon (SON) and a lesser amount from the southwest summer monsoon (JJA) (Figure S1b). Thus, both summer and autumn rainfall influence annual $\delta^{18}O_p$. Summer (more negative $\delta^{18}O$) and autumn (more positive $\delta^{18}O$) $\delta^{18}O_p$ are isotopically distinct (Figure S1b), making the annual proportion of summer vs autumn rainfall a dominant control on annual $\delta^{18}O_p$ (Wolf et al., 2020). The timing of the southward migration of the Intertropical Convergence Zone from summer to autumn is the driver of this shift because the southwesterly winds that bring moisture from the Indian Ocean and Bay of Bengal during the summer change to northeasterly winds that bring moisture from the western Pacific and South China Sea during the autumn. Importantly, neither summer nor autumn $\delta^{18}O_p$ reflect local rainfall amount (Wolf et al., 2020), meaning large-scale atmospheric processes control $\delta^{18}O_p$ in both monsoon systems. The upstream rainout of moisture sourced from the Bay of Bengal and Indian Ocean drives summer monsoon $\delta^{18}O_p$ (Pausata et al., 2011; Yang et al., 2016), whereas the mechanisms driving autumn $\delta^{18}O_p$ variability are less understood. In summary, we expect HH-1 $\delta^{18}O$ to reflect a combination of summer and autumn $\delta^{18}O_p$, which are governed by large-scale processes rather than local rainfall amount.

Since regional hydroclimatic processes control annual $\delta^{18}O_p$ in central Vietnam, we expected HH-1 $\delta^{18}O$ to differ from proxies of local hydroclimate (Mg/Ca, $\delta^{13}C$). However, we found a remarkable similarity and strong correlation between the HH-1 $\delta^{18}O$ record and the HH-1 $\delta^{13}C$ ($r = 0.79$, $p < 0.01$) and Mg/Ca ($r = 0.87$, $p < 0.01$) records (Figure 4.2). The Mg/Ca and $\delta^{13}C$ records exhibit a similarly strong correlation ($r = 89$, $p < 0.01$), suggesting the same mechanism controls all three proxies (Mg/Ca, $\delta^{13}C$, and $\delta^{18}O$). Following the interpretation of Patterson et al. (2023), we propose that this mechanism is PCP. If PCP influences stalagmite $\delta^{18}O$, this suggests that PCP primarily occurred on a stalactite or the cave ceiling (Deininger et al., 2021). While there is no stalactite above HH-1, we do see evidence of a previously connected soda straw on top of HH-1 indicating that some form of calcite precipitation likely occurred above the growing stalagmite.

We are not suggesting that $\delta^{18}O_p$ has no effect on HH-1 $\delta^{18}O$, but rather PCP may overprint the $\delta^{18}O_p$ signal in the HH-1 $\delta^{18}O$ record. To test this hypothesis, we use a geochemical model to remove the PCP signal from the HH-1 $\delta^{18}O$ record. Our method uses established geochemical relationships to 1) use the HH-1 Mg/Ca record to quantify PCP length (the duration of PCP in seconds), 2) convert PCP length to the equivalent change in $\delta^{18}O$, and 3) subtract the simulated $\delta^{18}O$ change from the HH-1 $\delta^{18}O$ record (see *Methods*). The resulting corrected $\delta^{18}O$ record ($\delta^{18}O_{corr}$) should reflect $\delta^{18}O$ changes driven by regional hydroclimate change ($\delta^{18}O_p$) rather than local hydroclimate change (PCP). We analyze the results of this correction in the following sections.

4.3.2. PCP corrected $\delta^{18}O$

Assuming PCP is the dominant control of all three HH-1 proxies ($\delta^{13}C$, $\delta^{18}O$, and Mg/Ca), we interpret HH-1 $\delta^{18}O$ as a record of local hydroclimate change driven by autumn rainfall variability (orange line, Figure 4.2a), the same interpretation used for the $\delta^{13}C$ and Mg/Ca records in Patterson et al. (2023). Previous work on these records revealed that on centennial-glacial timescales, global sea level change and the strength of the Atlantic Meridional Overturning Circulation (AMOC) are the primary drivers of local hydroclimate change in central Vietnam. Global sea level change causes predominantly dry conditions during periods of low sea level (35 – 14 ka) and wet conditions during periods of high sea level (Late MIS 3 and the Holocene), and meltwater fluxes into the North Atlantic lead to dry conditions during Heinrich Stadials. Using this prior knowledge of the HH-1 records, we assess changes to the HH-1 $\delta^{18}O$ record after we apply the PCP correction. Due to assumptions we make in the correction method and the resulting uncertainties (see *Methods*), we focus our analyses on large-scale changes in the HH-1 $\delta^{18}O_{corr}$ record.

As expected, the HH-1 $\delta^{18}O$ and $\delta^{18}O_{corr}$ records have notable differences (Figure 4.2a). The original $\delta^{18}O$ record ranges from -3 to -10 ‰, whereas the $\delta^{18}O_{corr}$ record has a smaller range of -6 to -10 ‰. Because the correction removes the PCP signal, the largest changes occur during periods of high PCP (high $\delta^{18}O$ and Mg/Ca) and the smallest changes occur during periods of low PCP (low $\delta^{18}O$ and Mg/Ca). This results in minimal corrections during wetter periods of the record, 45 – 35 ka and 13 – 4 ka, and large corrections during the driest periods of the record, 35 – 30 ka and 25 – 14 ka. With corrections reaching over 4‰ in places, they remove some notable features the original $\delta^{18}O$ record shares with the HH-1 Mg/Ca and $\delta^{13}C$ records. This includes the drying trend starting at 35 ka and the abrupt shift to wet conditions at 14 ka, both features reflecting changes in autumn rainfall amount driven by sea level change (Patterson et al., 2023). The correction also removes the anomalous negative excursions (wet excursions) from 30 – 25 ka and at 16 ka. Features preserved in the $\delta^{18}O_{corr}$ record include positive excursions during the Younger Dryas and Heinrich Stadials 1, 3, and 4. Overall, the $\delta^{18}O_{corr}$ record no longer shows a relationship with sea level change, but remains sensitive to changes in AMOC (Younger Dryas and Heinrich Stadials).

To test whether HH-1 $\delta^{18}O_{corr}$ tracks the changes in $\delta^{18}O_p$, we compare the HH-1 $\delta^{18}O_{corr}$ record to regional speleothem $\delta^{18}O$ records and isotope enabled climate model output. We first compare HH-1 $\delta^{18}O_{corr}$ to a composite $\delta^{18}O$ stalagmite record from China, which reflects Asian summer monsoon strength (Cheng et al., 2016). The China composite shows better agreement with the HH-1 $\delta^{18}O_{corr}$ record than the original HH-1 $\delta^{18}O$ record (Figure 4.3). They have similar values and are strongly in phase from 45 – 11 ka. Both show positive excursions during Heinrich Stadials and the Younger Dryas, and negative excursions during some Dansgaard Oeschger Events. Since $\delta^{18}O_p$ is the primary driver of the China composite $\delta^{18}O$ record, its similarities to the HH-1 $\delta^{18}O_{corr}$ indicate that HH-1 $\delta^{18}O_{corr}$ also reflects $\delta^{18}O_p$ variability. Interestingly, these records are antiphased during the Holcoene. Since the HH-1 record ends at ~4 ka, we are unable to determine whether this antiphasing continues for the duration of the Holocene.

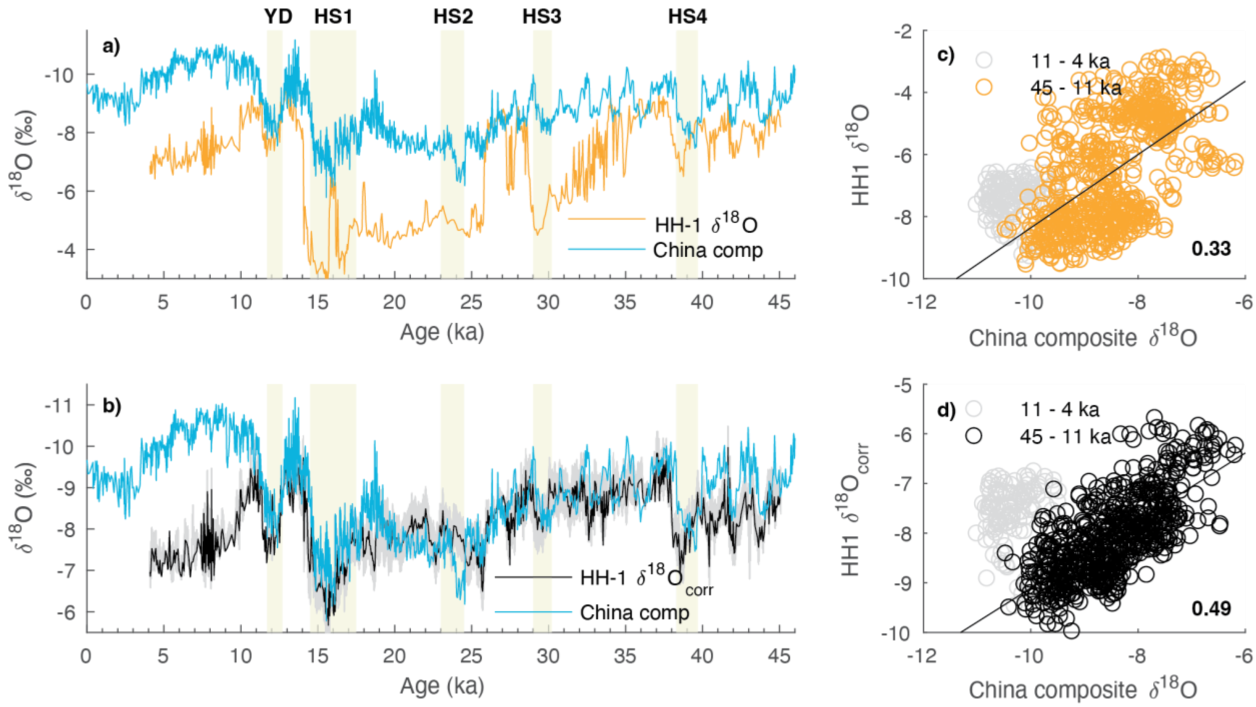

Figure 4.3. HH-1 δ^{18}O and $\delta^{18}O_{corr}$ compared to a composite δ^{18}O record of Chinese stalagmites. Time series and scatter plots of China composite δ^{18}O (blue) vs a,c) HH-1 δ^{18}O (gold) and b,d) HH-1 $\delta^{18}O_{corr}$ (black). Holocene values (grey circles) were excluded from R^2 values displayed on bottom right corner of panels c and d.

To compare the HH-1 δ^{18}O records to simulated central Vietnam $\delta^{18}O_p$, we use climate model simulations from iTRACE, an isotope-enabled transient climate model spanning the deglaciation, 20 – 11 ka (see *Methods* in Patterson et al. (2023)). Like the comparisons to regional δ^{18}O records, the JJA, SON, and annual iTRACE δ^{18}O time series better correlate to the HH-1 $\delta^{18}O_{corr}$ record than the original δ^{18}O record (Figures 4.4,4.5). While the correlation with JJA is highest (Figure 4.5d), the HH-1 $\delta^{18}O_{corr}$ time series better visually matches the δ^{18}O values and magnitude of change in the annual and SON time series (Figure 4.4b). The strong agreement between these records suggests that iTRACE correctly simulates $\delta^{18}O_p$ variability in central Vietnam and provides further evidence that the HH-1 $\delta^{18}O_{corr}$ record reflects changes in $\delta^{18}O_p$.

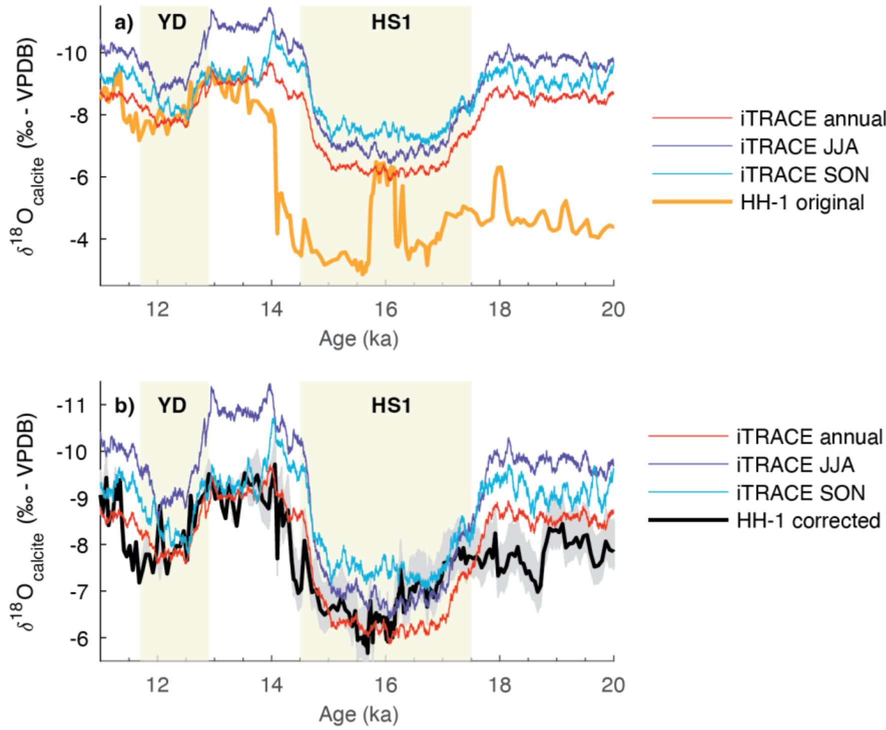

Figure 4.4. HH-1 $\delta^{18}O$ and $\delta^{18}O_{corr}$ compared to iTRACE $\delta^{18}O$. Time series of HH-1 a) $\delta^{18}O$ (orange) and b) $\delta^{18}O_{corr}$ (black) vs iTRACE JJA (purple), SON (light blue), and annual $\delta^{18}O_c$ (red). iTRACE $\delta^{18}O_c$ (VPDB) calculated from mean weighted $\delta^{18}O_p$ (VSMOW) output using Equation 1 in (Daëron et al., 2019). iTRACE curves are smoothed with a 100 year running mean.

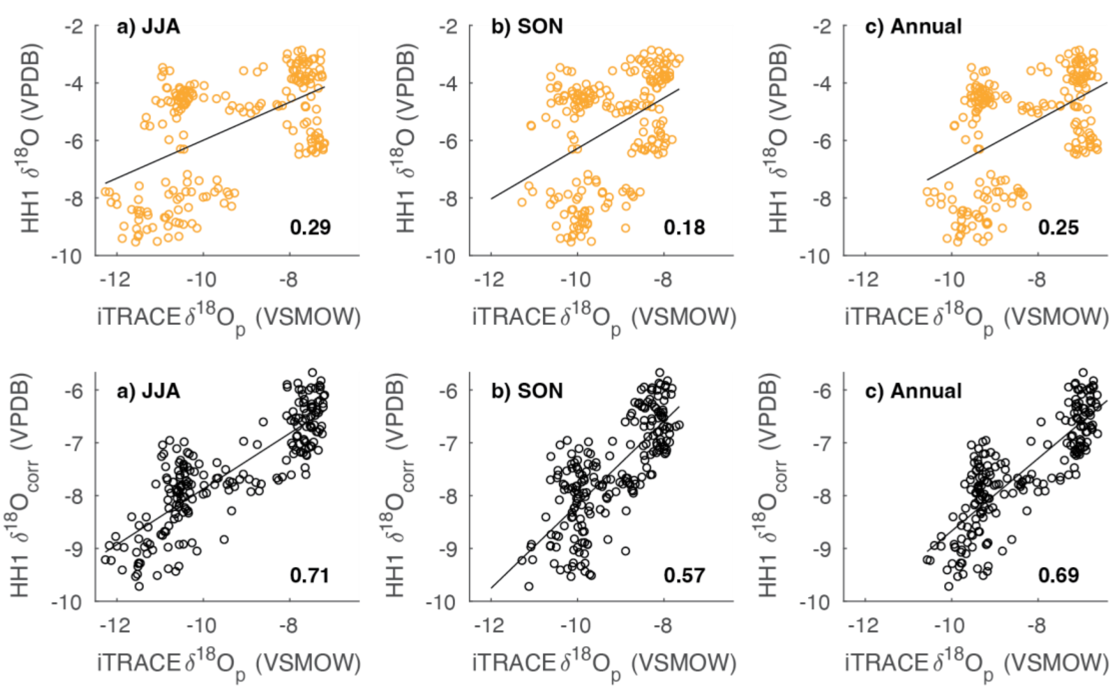

Figure 4.5. Scatter plots of iTRACE $\delta^{18}O_p$ vs HH-1 $\delta^{18}O$ (orange, a-c) and HH-1 δ^{18}Ocorr (black, d-f). iTRACE output was smoothed with a 50 yr running mean. R^2 value displayed in bottom right corner of each panel.

4.3.3. Central Vietnam $\delta^{18}O_p$ variability over the last 45,000 years

We interpret HH-1 $\delta^{18}O_{corr}$ as a record of weighted annual mean $\delta^{18}O_p$ in central Vietnam. Understanding this record is challenging because both summer (JJA) and autumn (SON) rainfall, specifically the relative contribution of each season, drive modern annual $\delta^{18}O_p$ variability in central Vietnam (Wolf et al., 2020). This means that HH-1 $\delta^{18}O_{corr}$ variability could reflect changes in JJA $\delta^{18}O_p$, SON $\delta^{18}O_p$, or the two seasons simultaneously. For this reason, we consider both the summer and autumn monsoons when interpreting the HH-1 $\delta^{18}O_{corr}$ record.

We first examine $\delta^{18}O_p$ variability during the deglaciation using iTRACE simulations. The similarity between the simulated JJA and SON $\delta^{18}O_p$ time series and their strong correlation with the HH-1 $\delta^{18}O_{corr}$ record makes disentangling the summer and autumn monsoon signals difficult (Figures 4.4, 4.5). A previous analysis of iTRACE simulations found that changes in seasonality (summer vs autumn rainfall) minimally contributes to annual $\delta^{18}O_p$ change across East and Southeast Asia (He et al., 2021). Instead, they show that changes in the isotopic composition of JJA rainfall controls annual $\delta^{18}O_p$ variability during the deglaciation, with SON $\delta^{18}O_p$ playing a minor role. However, iTRACE simulations underestimate SON rainfall amount (see Figure S1e in *Appendix B*), suggesting that the model may not capture the full influence of SON rainfall on the annual $\delta^{18}O_p$ signal. Ultimately, HH-1 $\delta^{18}O_{corr}$ record best matches the values of the annual $\delta^{18}O_p$ simulation

(Figure 4.4), suggesting that our stalagmite likely records the combined $\delta^{18}O_p$ signal of both monsoon seasons.

When broken down into individual forcings, iTRACE $\delta^{18}O_p$ simulations reveal that meltwater forcing drives the majority of $\delta^{18}O_p$ variability during the deglaciation (MWF curve in Figure S2). This includes positive excursions during the HS1 and YD meltwater events, features also present in HH-1. In addition to HS1 and the YD, the HH-1 $\delta^{18}O_{corr}$ record shows positive excursions during Heinrich Stadials 3 and 4, indicating central Vietnam $\delta^{18}O_p$ responds somewhat consistently to meltwater events. The absence of HS2 in the HH-1 record indicates that HS2 is weaker compared to other instances, which aligns with observations made in other paleoclimate records (Lynch-Stieglitz et al., 2014; Wright et al., 2023). The signature of meltwater events on the Asian summer monsoon is well documented in speleothem $\delta^{18}O$ records (Cheng et al., 2016; Zhang et al., 2018). During meltwater events the southward shift of the ITCZ and westerly jet weakens moisture transport (Zhang & Delworth, 2005), which reduces upstream rainout and increases $\delta^{18}O_p$ values across the region (Pausata et al., 2011). Conversely, the meltwater-driven mechanism on $\delta^{18}O_p$ during SON is currently unknown.

The drivers of Holocene $\delta^{18}O_p$ variability in central Vietnam are less clear. During the Holocene, speleothem $\delta^{18}O$ records of Asian summer monsoon intensity reach their $\delta^{18}O$ minimum in the early Holocene (Figure 4.3), lagging Northern Hemisphere Summer Insolation by ~3 kyrs (Cheng et al., 2016; Wang et al., 2008). The HH-1 $\delta^{18}O_{corr}$ record does not follow this trend, but rather increases starting at 11 ka. This suggests factors other than changes to summer $\delta^{18}O_p$ affect central Vietnam $\delta^{18}O_p$ during the Holocene. Two possibilities included changes in seasonality (summer versus autumn precipitation amount) and/or the isotopic composition of autumn rainfall,

Decreased seasonality (decreased summer precipitation relative to autumn precipitation) is one possible driver of increased Holocene $\delta^{18}O$ in the HH-1 $\delta^{18}O_{corr}$ record. Less summer rainfall (more negative $\delta^{18}O_p$) or more autumn rainfall (more positive $\delta^{18}O_p$) would increase annual $\delta^{18}O_p$ values. The orbitally and greenhouse gas forced (ORB+GHG, the strongest forcings during the Holocene) iTRACE simulations, do not agree with this theory, showing JJA precipitation increasing relative to SON precipitation into the Holocene (Figure S3). A lake record from Thailand shows similar results, with summer precipitation peaking during the mid-Holocene (Chawchai et al., 2013). As for changes in autumn precipitation amount, the HH-1 proxies of local hydroclimate, which reflect autumn rainfall amount, show relatively little change in autumn rainfall during the Holocene (Figure 4.2). Importantly, during the Holocene and in other portions of the HH-1 record, both proxies reach a lower threshold (dashed line in Figure 4.2b), where they are less sensitive to hydroclimate. This suggests that the HH-1 record may not fully capture hydroclimate variability during the Holocene. Additional records of Holocene autumn rainfall are necessary to evaluate changes in local rainfall amount. Altogether these results do not suggest that seasonality drove HH-1 $\delta^{18}O$ change during the Holocene.

Higher autumn monsoon $\delta^{18}O_p$ values would also increase annual $\delta^{18}O_p$ during the Holocene. Since we know little about the isotopic controls on autumn monsoon rainfall, we can only speculate on its potential drivers. For instance, a decrease in local autumn rainfall amount could decrease $\delta^{18}O_p$. However, this is unlikely, because $\delta^{18}O_p$ of autumn rainfall is not linked to rainfall amount (He et al., 2021; Wolf et al., 2020). Other factors, such as a more proximal moisture source (less upstream rainout, (Pausata et al., 2011)), decreased stratiform versus convective precipitation (Aggarwal et al., 2016), changes in microphysical cloud processes (Bony et al., 2008; Risi et al., 2008), and decreased cloud-top height (Cai & Tian, 2016) would all increase autumn $\delta^{18}O_p$. Without a deeper understanding of the drivers of SON $\delta^{18}O_p$, we cannot propose a single mechanism.

In summary, during the Late Pleistocene, meltwater-forced changes in $\delta^{18}O_p$ drive central Vietnam $\delta^{18}O_p$ variability. With the HH-1 $\delta^{18}O_{corr}$ record deviating from other regional $\delta^{18}O$ records during the Holocene, our understanding of Holocene $\delta^{18}O_p$ variability in central Vietnam is less clear. Moving forward, more $\delta^{18}O$ records from this region, particularly of the Holocene, and more in-depth investigations into autumn monsoon $\delta^{18}O_p$ dynamics are essential.

4.4. Implications

In this study, we emphasize the significant impact of PCP on a speleothem $\delta^{18}O$ record, which has far-reaching implications for our understanding of 45,000 years of central Vietnam $\delta^{18}O_p$ variability. Without consideration of PCP and our attempts to remove it, we would have severely misinterpreted the HH-1 $\delta^{18}O$ record. Furthermore, this would have led us to misdiagnose model-proxy disagreement with iTRACE, despite the model performing well. While certain inaccuracies in speleothem $\delta^{18}O$ records are inevitable, it remains essential to address and eliminate them to improve their utility and reliability.

Although PCP only affects speleothem $\delta^{18}O$ under certain conditions (when PCP occurs on the cave ceiling or stalactite), future studies should screen for PCP-influenced

$\delta^{18}O$ when generating new speleothem records. This could be done through the generation of multiproxy stable isotope and trace elements records from the same speleothem. While it is currently unknown how widespread the effects PCP on speleothem $\delta^{18}O$ are, PCP is a well-documented driver of many existing $\delta^{13}C$ and trace element records. Thus, generating and interpreting speleothem $\delta^{13}C$ and trace element records alongside $\delta^{18}O$ records could identify whether PCP occurs in drip waters feeding the speleothem sample. As shown in this study, strong similarities between speleothem $\delta^{18}O$ and these proxies are an indicator of PCP-influenced $\delta^{18}O$.

Furthermore, we show that with a Mg/Ca record and a good understanding of the cave environment, it is possible to remove the PCP signal from a speleothem $\delta^{18}O$ record. Although this method is relatively novel, it builds upon well-established geochemical relationships. We acknowledge that this method requires a precise understanding of cave environment and may not be suitable for all PCP-affected speleothem records. Nonetheless our findings reveal the potential of this method and underscore its significance in advancing the field of speleothem science.

4.5. Methods

4.5.1. $\delta^{18}O$ PCP correction procedure and model description

Our geochemical model corrects for PCP in the HH-1 $\delta^{18}O$ record using the HH-1 Mg/Ca time series. Notably, Mg/Ca has been used to remove PCP from speleothem $\delta^{13}C$ records (Stoll et al., 2022), but has been underutilized as a method to correct speleothem $\delta^{18}O$ records. Because the methods we utilize are well-established, we outline our general procedure and model description here.

The following equations describe how PCP affects speleothem Mg/Ca and $\delta^{18}O$.

$$Mg/Ca_0 + Mg/Ca_{PCP} = Mg/Ca_{observed} \text{ (Eq. 1)}$$

$$\delta^{18}O_0 + \delta^{18}O_{PCP} = \delta^{18}O_{observed} \text{ (Eq. 2)}$$

Here, the Mg/Ca_0 and $\delta^{18}O_0$ terms represent the initial Mg/Ca and $\delta^{18}O$ values of calcite precipitated from drip water. Mg/Ca_0 generally reflects bedrock or soil derived Mg flushed into the epikarst, whereas $\delta^{18}O_p$ is the main driver of $\delta^{18}O_0$. We assume Mg/Ca_0 does not change much through time, so we use a constant Mg/Ca_0 value in the model (see model parameters section). Conversely, we expect $\delta^{18}O_0$ to vary through time and follow changes in $\delta^{18}O_p$. The Mg/Ca_{PCP} and $\delta^{18}O_{PCP}$ terms represent the Rayleigh fractionation between the drip water and precipitated calcite that occurs during PCP. Mg/Ca_{PCP} or $\delta^{18}O_{PCP}$ is a function of PCP length, the duration of calcite precipitation (in seconds) that occurs in the drip water prior to reaching the speleothem. The $Mg/Ca_{observed}$ and $\delta^{18}O_{observed}$ terms represent the measured $\delta^{18}O$ and Mg/Ca values in the speleothem. Longer PCP lengths (higher X_{PCP}) allow for increased Rayleigh fractionation between drip water and precipitated calcite, resulting in larger differences between X_0 and $X_{observed}$ (higher speleothem $\delta^{18}O$ and Mg/Ca). The model first estimates PCP length for each time point with the HH-1 Mg/Ca time series ($Mg/Ca_{observed}$) and a constant Mg/Ca_0 value (Eq. 1, Figure S4). From PCP length, we calculate the equivalent PCP induced change in $\delta^{18}O$ ($\delta^{18}O_{PCP}$). The $\delta^{18}O_{PCP}$ value is then subtracted from the original HH-1 time series ($\delta^{18}O_{observed}$) to produce the final $\delta^{18}O_{corr}$ time series (Eq. 2, Figure 4.2a). Ultimately, $\delta^{18}O_{corr}$ should approximate $\delta^{18}O_0$, which reflects $\delta^{18}O_p$ variability.

Our model utilizes well-established geochemical relationships. We use an isotope and calcite precipitation model that was first described in Scholz et al. 2009 and is later used in many geochemical modeling studies (Deininger et al., 2012; Deininger & Scholz, 2019; Skiba & Fohlmeister, 2023). The model simulates $\delta^{18}O$ evolution of HCO_3^- through time with a Rayleigh distillation model. This model has three sinks (H_2O, CO_2 degassing and $CaCO_3$ precipitation), estimates carbonate precipitation rate using an exponential approach (Dreybrodt, 1980), and accounts for oxygen isotope exchange between drip water HCO_3^- and the water reservoir (H_2O exchange).

4.5.2. Model parameters

The isotope evolution and $CaCO_3$ precipitation models we use for the PCP correction require a variety of parameters as inputs (Table S1). We use direct measurements of the cave environment when possible and when unavailable, use model output and values from the literature. To understand the uncertainty of our correction, we also performed sensitivity testing with some of the model parameters. Here, we describe each parameter and explain the values we chose for the initial correction as well as the sensitivity testing.

We use a constant value of 2.23 mmol/mol for Mg/Ca_0 (black dashed line in Figure 4.2b). We derived this value by averaging two portions of the HH-1 Mg/Ca record (45 – 37 ka, and 11 – 4 ka) where little to no PCP occurred. The comparatively low and relative stable Mg/Ca values are indicators that little to no PCP occurred during these periods. For sensitivity testing, we varied Mg/Ca_0, between 1.96 – 2.5 mmol/mol, the standard deviation of the two time periods.

Since temperature was not constant during the last 45,000 years, we approximated a temperature time series using a combination of cave monitoring data and iTRACE climate model output (Figure S5). We assumed a constant temperature of 21 °C during the Holocene (11 – 4 ka in the HH-1 record), the average modern annual temperature of Hoa Huong cave. From 20 – 11 ka, we varied temperature based on a 50 year running mean of simulated iTRACE surface temperature from the grid cell encompassing the study site. We used a constant temperature of 18.5 °C for the time period of 45 – 20 ka, the average iTRACE simulated surface temperature from 20 – 19.9 ka. For sensitivity testing, we varied temperature from +/- 2 °C, the current seasonal range in Hoa Huong cave (Patterson et al., 2023).

The model also required inputs of the initial Ca concentration (Ca_0) and equilibrium Ca concentration (Ca_{eq})of the drip water, which are related to the pCO_2 in the epikarst and in the cave, respectively. Because we do not have measurements of epikarst pCO_2, we rely on values reported in the literature to estimate Ca_0. For our model to be feasible, we use a value of 3.4 mol/mol^3, which is equivalent to a pCO_2 of 45,000 ppm at 20 °C (assume same temperature for all following pCO_2 values). We acknowledge that this value is higher than most soil pCO_2 measurements, however several studies found epikarst pCO_2 values to be as high as 60,000 – 100,000 ppm (Benavente et al., 2010; Peyraube et al., 2013). We test a range of values, 3.4 – 4 $mmol/mol^3$ (equivalent to 45,000 – 63,000 ppm), during our sensitivity testing. For Ca_{eq}, we used a value of 0.8 mol/mol^3, which corresponds to a pCO2 value of 1,400 ppm, an average of the measured pCO_2 values from Hoa Huong Cave. For the sensitivity testing, we use a range of 0.6 – 1.4 mmol/mol3, which corresponds to pCO_2 values of 200 – 3,000 ppm. Our low estimate of 200 ppm reflects atmospheric conditions during the last glacial maximum and also assumes that the cave is fully ventilated. We based our highest estimate of 3,120 ppm on the highest measured value of pCO_2 recorded in Hoa Huong cave.

Since there is no active drip at the collection site, we are unable to measure the drip interval. Even though the large growth rate changes indicate that drip interval likely did change through time, we use a constant drip interval of 1 drip/second. However, previous work found changes in drip interval had a negligible effect on the isotopic composition of calcite when compared to the effects of PCP (Skiba & Fohlmeister, 2023).

We use the Day & Henderson (2013) laboratory-based measurements to calculate the partition coefficient of Mg ($D_{(Mg)}$). Since $D_{(Mg)}$ is temperature dependent, we calculate $D_{(Mg)}$ at each time step using the approximated cave temperature record (Fig S5). The model also uses temperature dependent $\delta^{18}O$ fractionation factors (see Skiba and Fohlmeister (2023) for full list).

4.5.3. Model uncertainty and sensitivity testing

For the sensitivity analyses, we performed a series of Monte Carlo simulations with 1,000 simulations each. To assess the uncertainty of the full model, we randomly varied each parameter at each time step (Figure S6a, grey shading on $\delta^{18}O_{corr}$ in figures 4.2-4.4). To assess the uncertainty of some parameters, we randomly varied a single parameter (Mg/Ca_0, cave temperature, Ca_0, and Ca_{eq}) while keeping the remaining variables constant (Figure S6b-d). For the full model run, the average 1σ deviation was +/- 0.21 ‰, a relatively small value when compared to full range of variability in the HH-1 $\delta^{18}O_{corr}$ record. Our tests also revealed that the Mg/Ca_0 parameter causes nearly all of the variability in the simulations (Figure S6b). The variability of the remaining variables (temperature, Ca_0, and Ca_{eq}), is negligible. This suggests an accurate estimate of Mg/Ca_0 is crucial for future use of this correction method.

We also tested whether including H_2O exchange in the model impacted the correction results and found that its inclusion made very little impact on the correction (Figure S7). This is because PCP length is substantially shorter than the time required for complete H_2O exchange (Figure S4).

Importantly, our model only accounts for PCP occurring immediately prior to speleothem precipitation (i.e. PCP on the cave ceiling or stalactite) and excludes PCP in the epikarst. Since epikarst PCP has no effect on $\delta^{18}O$ (Deininger et al., 2021), we expect the speleothem $\delta^{18}O$ record to only reflect PCP on the cave ceiling/stalactite. Conversely, epikarst PCP does effect drip water Mg/Ca. In cases where PCP occurs in the epikarst and in the cave, our model would overestimate Mg/Ca-derived PCP length, resulted in an overcorrection of the speleothem $\delta^{18}O$ record. Because we cannot currently detangle epikarst PCP from in cave PCP, we present this caveat to our model approach. The strong agreement between the HH-1 $\delta^{18}O_{corr}$ record and other regional speleothem/climate model records indicates that our correction method was successful. This mean that most, if not all PCP, records in the HH-1 speleothem occurred on the cave ceiling/stalactite.

APPENDIX C

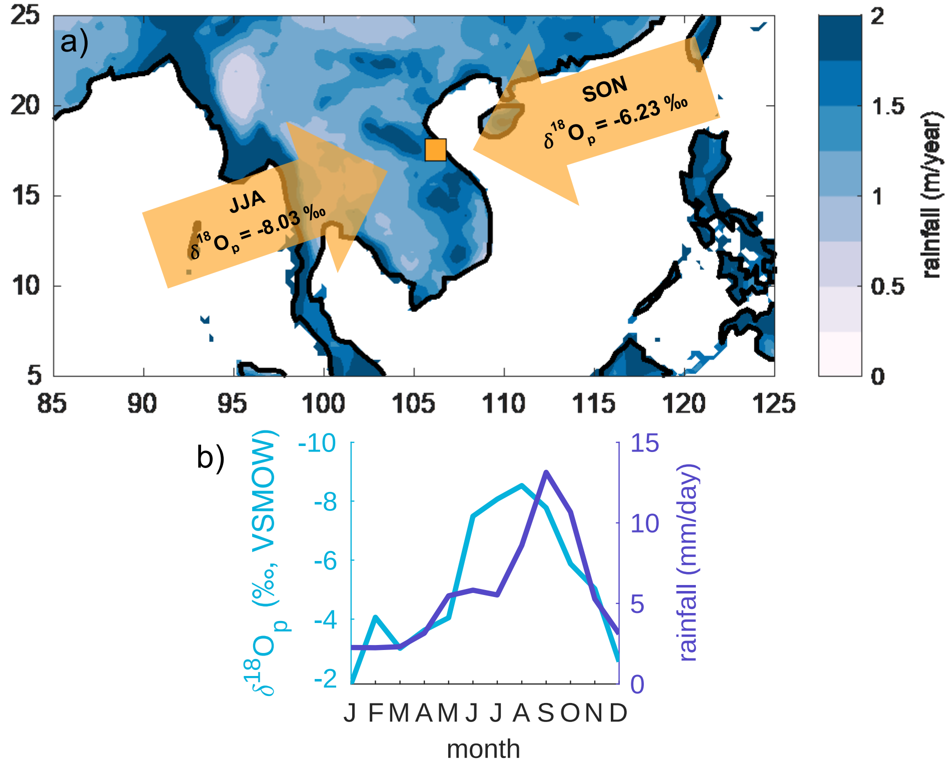

Figure S1. Study site climatology. a) Map of total annual precipitation in MSEA derived from Asian Precipitation-Highly Resolved Observational Data Integration Towards Evaluation (APHRODITE) (Yatagai et al., 2012). Arrows show wind direction of the SW monsoon and NE monsoon with average $\delta^{18}O_p$ values of JJA and SON precipitation. Orange square denotes study site location. b) Average seasonal cycle of study site APHRODITE rainfall (purple) from the cell encompassing Hoa Huong Cave and $\delta^{18}O_p$ (light blue, see *Section 1 in Appendix A*) at Phong Nha-Ke Bang Park Headquarters.

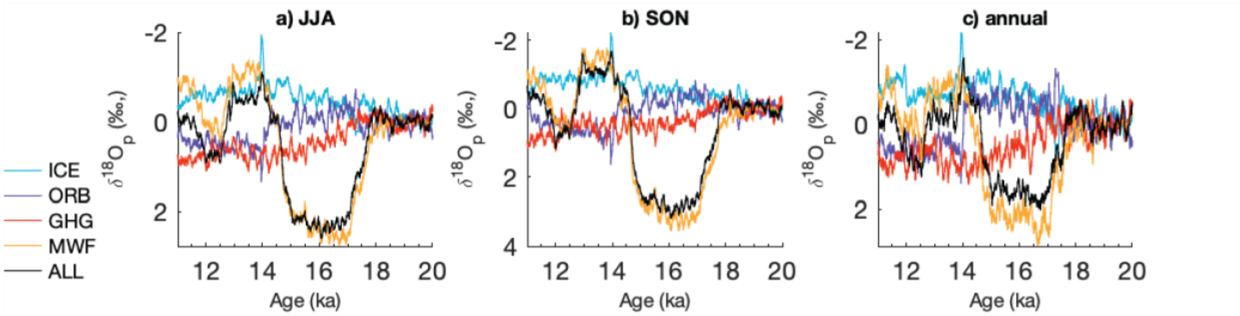

Figure S2. Time series of individual forcings of weighted simulated iTRACE $\delta^{18}O_p$. iTRACE a) JJA, b) SON, and c) annual precipitation time series from the grid cell encompassing the study site in response to different forcings (ICE - light blue, ORB - purple, GHG - red, MWF - orange, and ALL forcings - black). We standardize the curves by subtracting the LGM climatology. The different forcings are isolated from the different iTRACE runs as follows; ICE = ICE – LGM, ORB = ICE + ORB – ICE – LGM , GHG = ICE + ORB + GHG – ICE + ORB – LGM, and MWF = ICE + ORB + GHG + MWF – ICE + ORB + GHG – LGM. Curves are smoothed with a 100 year running mean.

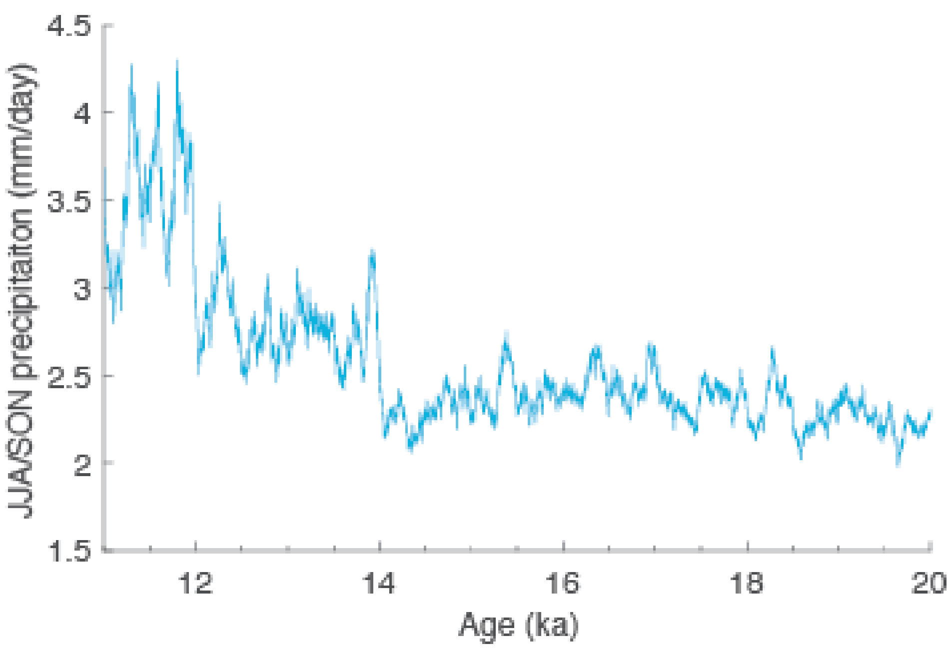

Figure S3. The fraction of JJA vs SON precipitation from iTRACE simulations for orbital and greenhouse gas (ORB+GHG) forcings. Curve smoothed with a 100 year running mean.

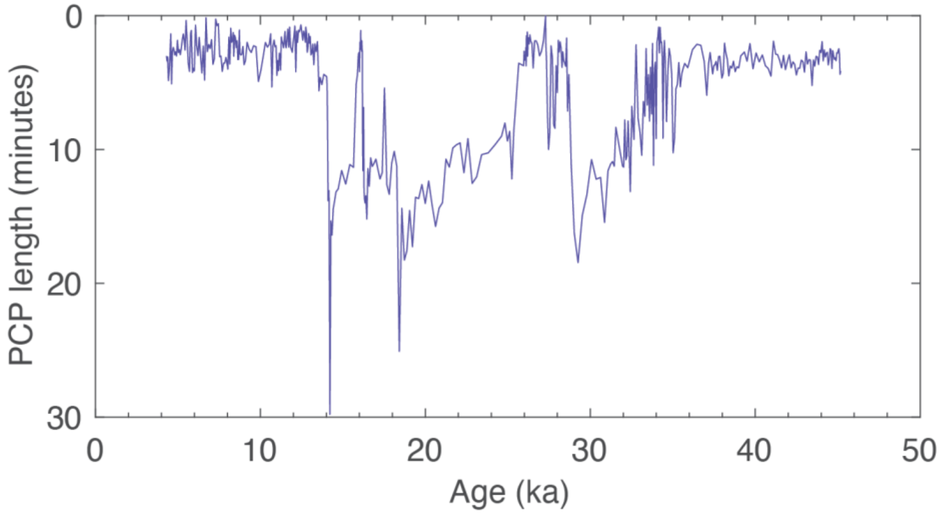

Figure S4. Output of PCP length from the PCP correction model.

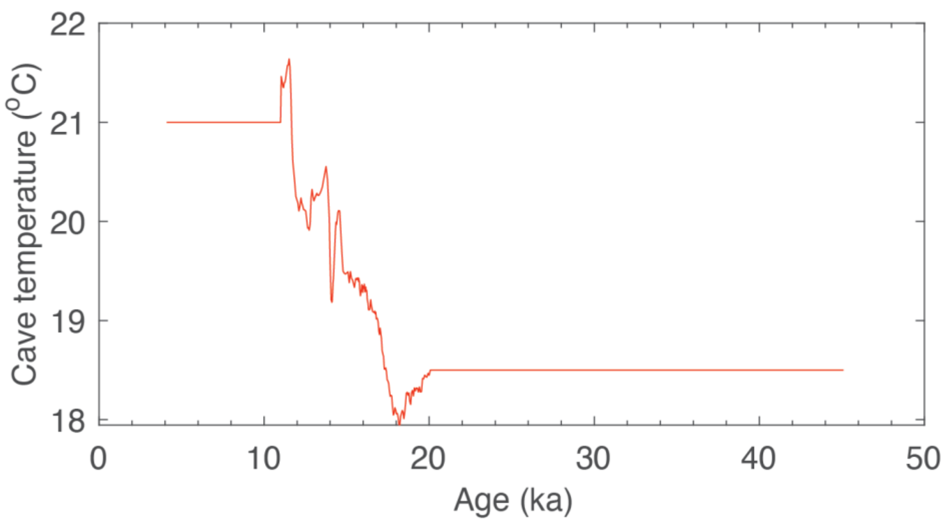

Figure S5. Time series of temperature values used in the PCP correction model.

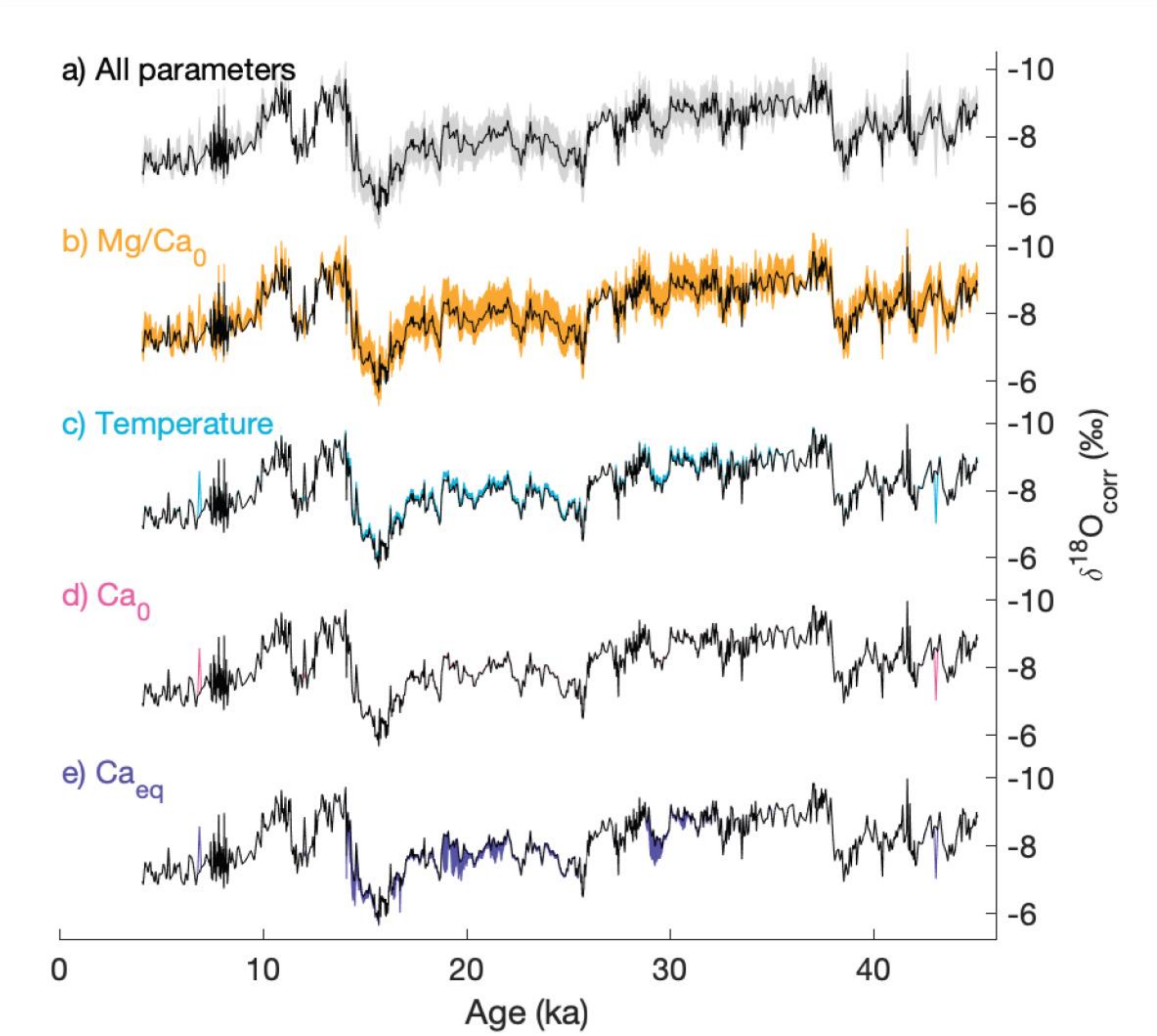

Figure S6. Sensitivity analyses of different parameters used in the PCP correction model. The black curve in all panels is the final $\delta^{18}O_{corr}$ time series. Shading shows the 1σ standard deviation of the 1000 Monte Carlo simulations at each time point for a) all parameters (grey), b) Mg/Ca_0 (orange), c) cave temperature (light blue), d) Ca_0 (pink), e) Ca_{eq} (purple). In some cases (e.g. panel c), the shading may be too small to see on the plot.

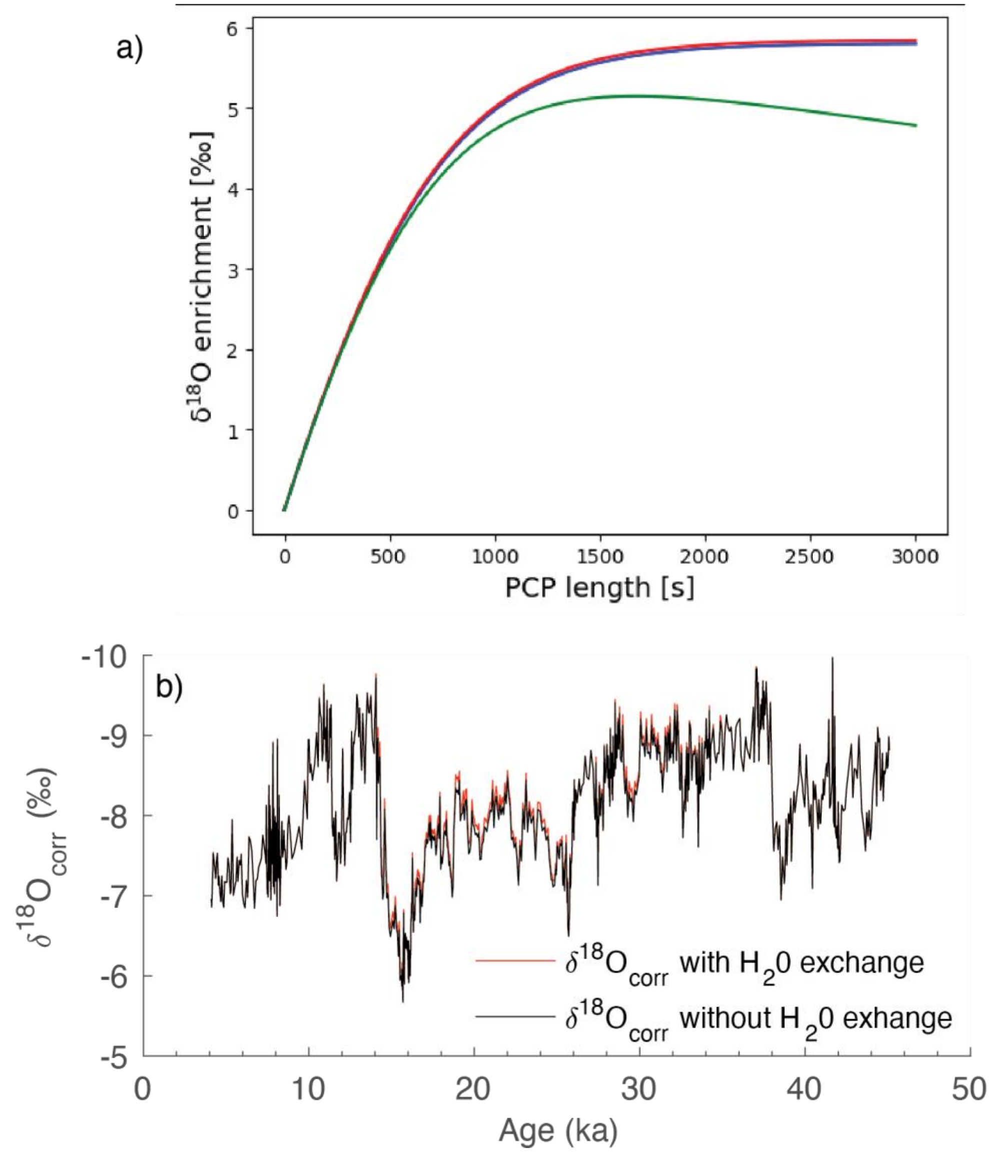

Figure S7. PCP correction with and without H_2O exchange incorporated in the model. a) PCP length vs δ^{18}O enrichment. b) HH-1 $\delta^{18}O_{corr}$ curves with H_2O exchange (black) and without H_2O exchange (red).

Table S1. Values used for PCP correction model and sensitivity testing

Parameter	Value	Sensitivity testing
Mg/Ca	2.23 mmol/mol	1.96 – 2.5 mmol/mol
Cave temperature	21ºC (4 – 11 ka) iTRACE mean annual T (11 – 20 ka) 8.5ºC (20 – 45 ka)	+/- 2ºC
Ca_0	3.4 mol/mol^3	3.4 – 4 (mol/mol^3) Equivalent to 45,000 – 63,000 ppm
Ca_{eq}	0.8 mol/mol^3	0.6 – 1.4 (mol/mol^3) Equivalent to 200 – 3,120 ppm
Drip interval	1 drip/second	N/A

CHAPTER 5: CONCLUSIONS

In this dissertation I use stalagmite HH-1, cave monitoring measurements, climate model output, and geochemical models to investigate central Vietnam hydroclimate and Southeast Asian autumn monsoon variability over the last 45,000 years. My three data chapters (Chapters 2-4) utilize different methods and geochemical proxies to reconstruct changes in local and regional hydroclimate. Below, I briefly summarize the main findings, implications, and areas for future work for each chapter.

In Chapter 2, I present a new qualitative multiproxy record of autumn monsoon rainfall, which provides significant advancements in our understanding of central Vietnam hydroclimate. I find that, since the Late Pleistocene, the Southeast Asian autumn monsoon was highly variable and underwent periods of abrupt change. Using both the speleothem record and climate model output, I identify a previously unknown driver of Southeast Asian autumn monsoon variability on millennial to orbital timescales – local sea level change, specifically the inundation and exposure of the Gulf of Tonkin and South China shelf. Altogether, these findings shed new light on the understudied Southeast Asian autumn monsoon. However, due to the 30-year resolution of the HH-1 record, I was unable to investigate short-term hydroclimate change. Thus, additional high resolution paleoclimate reconstructions are needed to study autumn rainfall variability on interannual to multidecadal timescales. This could be partially achieved by sampling stalagmite HH-1 at a higher resolution (e.g. high resolution micromilling and/or laser ablation methods). Additional speleothem samples will be necessary to investigate interannual to decadal variability during periods of slow growth in HH-1 (e.g. the Last Glacial Maximum) and/or not covered by the sample (modern – 4 ka or >45,000 ka).

The implications of the role of sea-level in the HH-1 record extend beyond the Southeast Asian autumn monsoon. While future projections for land exposure change in the Gulf of Tonkin and the South China shelf are minimal, my findings underscore the potential for rapid shifts in local sea level to trigger abrupt hydroclimate change in surrounding regions. Given the projected sea-level rise driven by anthropogenic climate change, vast landmasses worldwide, including the vulnerable Mekong Delta in southern Vietnam, face the risk of inundation. My results serve as a crucial example of how such landmass transformations can significantly impact precipitation patterns on a local scale.

In Chapter 3, I present a semi-quantitative reconstruction of rainfall using δ^{44}Ca. Calcium isotopes are a promising and new speleothem proxy, making my findings a valuable addition to the limited literature in the field. My analyses demonstrate that HH-1 δ^{44}Ca measurements not only serve as a record of central Vietnam hydroclimate but also, when translated to rainfall amount, exhibit comparable changes to climate model simulations. Ultimately, the δ^{44}Ca record builds upon the results of Chapter 2, as it semi-quantifies the shifts in rainfall amount caused by sea-level change.

The introduction of quantitative reconstructions of rainfall amount is a significant advancement for speleothem science, given that most proxies used in this field are qualitative. Importantly, substantial methodological limitations and uncertainties around δ^{44}Ca-derived rainfall remain. To further refine these estimates of rainfall change, it is imperative to deepen our understanding of site-specific calcium isotope systematics and the relationship between precipitation and PCP. Addressing these challenges would transform semi-quantitative reconstruction into more comprehensive and robust quantitative records of past rainfall change.

For future work with calcium isotopes in Hoa Huong cave, I would recommend collecting and measuring the $\delta^{44}Ca$ of modern calcite, drip water, and additional bedrock samples. These data would better constrain a site-specific fractionation factor, which would improve our estimates of PCP and rainfall amount. To address the unknown relationship between PCP and rainfall amount, I would suggest conducting a multiyear cave monitoring program where measurements of drip rate, drip water $\delta^{44}Ca$, modern calcite $\delta^{44}Ca$ are compared directly to local rainfall amount. Lastly, I suggest generating multiple overlapping speleothem $\delta^{44}Ca$ records from Hoa Huong cave, which would reveal the reproducibility and consistency of calcite $\delta^{44}Ca$ in a single cave system.

Chapter 4 focuses on the HH-1 $\delta^{18}O$ record, which I use to interpret large-scale hydroclimate change rather the local rainfall amount. I demonstrate that PCP, a long-dismissed control on speleothem $\delta^{18}O$, affects the HH-1 record. After correcting the $\delta^{18}O$ record for the effects of PCP, HH-1 $\delta^{18}O$ shows agreement with regional $\delta^{18}O$ records and climate model simulations. Although controls on autumn $\delta^{18}O_p$ and the drivers of Holocene $\delta^{18}O_p$ variability remain partially unresolved, the HH-1 $\delta^{18}O$ record is a robust reconstruction of central Vietnam $\delta^{18}O_p$. The corrected $\delta^{18}O$ record builds upon a vast network of speleothem $\delta^{18}O$ records from across the Asian monsoon region, providing the longest record from Mainland Southeast Asia, a region largely devoid of $\delta^{18}O$ paleorecords. Additional $\delta^{18}O$ records from central Vietnam, particularly those spanning the Holocene, would prove invaluable in resolving the main drivers of regional $\delta^{18}O_p$. To better constrain controls on modern and past autumn $\delta^{18}O_p$, I would recommend an in-depth investigation of local instrumental data and isotope-enabled climate model output, similar to that of Yang et al., 2016.

The novel approach I adopt to interpret and correct the HH-1 $\delta^{18}O$ record has significant implications for the field of speleothem science. Considering $\delta^{18}O$ is the most commonly utilized proxy in speleothems, with hundreds of records worldwide, my findings that PCP affects speleothem $\delta^{18}O$ prompts a reevaluation of existing and future speleothem $\delta^{18}O$ records. As a result, my research sets the foundation for screening and correcting speleothem $\delta^{18}O$ records for PCP. However, further work is necessary to evaluate the prevalence of PCP-influenced $\delta^{18}O$ and to rigorously test the effectiveness of the geochemical model used in the correction method. This knowledge will enhance the accuracy and reliability of speleothem-based $\delta^{18}O$ reconstructions, thus avoiding misinterpretation of climate records.

Lastly, proxy-model comparisons are a common thread throughout my dissertation. These comparisons serve a dual purpose: 1) to validate climate model output, and 2) to identify the primary large-scale drivers of Southeast Asian autumn monsoon rainfall amount and $\delta^{18}O_p$. The remarkable agreement observed between the iTRACE simulations and the HH-1 record is a promising indication that the model accurately captures the dynamics of the Southeast Asian autumn monsoon. Using this information, I was able to use climate model output to identify sea level as the main driver of the autumn rainfall variability on millennial to orbital timescales. Importantly, this agreement also strengthens our confidence in the model to correctly simulate future hydroclimate change.

Despite the valuable insights gained from these comparisons, it is important to acknowledge that the use of only one climate model presents some limitations.

Incorporating additional climate models would improve the certainty of the conclusions of my dissertation. For example, in Chapter 3, using a diverse suite of climate models would provide a more comprehensive estimate of past rainfall change, improving my assessment of the δ^{44}Ca-derived rainfall record. Future studies should consider including multiple climate models to better refine our understanding of the Southeast Asian autumn monsoon and its broader implications for regional hydroclimate variability.

In summary, my dissertation comprehensively explores Southeast Asian autumn monsoon variability since the Late Pleistocene, significantly enriching our knowledge of this understudied phenomenon and holding the potential to better inform our predictions of future hydroclimate change. My implementation of novel geochemical proxies, such as δ^{44}Ca, along with the development of innovative methods like PCP removal, improved my analyses and advances speleothem science. Ultimately, my work opens new avenues for research and contributes to the broader field of climate science.

REFERENCES

Aggarwal, P. K., Romatschke, U., Araguas-Araguas, L., Belachew, D., Berg, P., Schumacher, C., & Funk, A. (2016). Proportions of convective and stratiform precipitation revealed in water isotope ratios. *Nature Geoscience*, *9*(8), 624–629.

Baker, A., Hartmann, A., Duan, W., Hankin, S., Comas-Bru, L., Cuthbert, M. O., et al. (2019). Global analysis reveals climatic controls on the oxygen isotope composition of cave drip water. *Nature Communications*, *10*(1), 2984.

Benavente, J., Vadillo, I., Carrasco, F., Soler, A., Liñán, C., & Moral, F. (2010). Air carbon dioxide contents in the vadose zone of a Mediterranean Karst. *Vadose Zone Journal: VZJ*, *9*(1), 126.

Blättler, C. L., & Higgins, J. A. (2014). Calcium isotopes in evaporites record variations in Phanerozoic seawater SO4 and Ca. *Geology*, *42*(8), 711–714.

Blättler, C. L., & Higgins, J. A. (2017). Testing Urey's carbonate–silicate cycle using the calcium isotopic composition of sedimentary carbonates. *Earth and Planetary Science Letters*, *479*, 241–251.

Bony, S., Risi, C., & Vimeux, F. (2008). Influence of convective processes on the isotopic composition (δ18O andδD) of precipitation and water vapor in the tropics: 1. Radiative-convective equilibrium and Tropical Ocean–Global Atmosphere–Coupled Ocean-Atmosphere Response Experiment (TOGA-COARE) simulations. *Journal of Geophysical Research*, *113*(D19). https://doi.org/10.1029/2008jd009942

Brady, E., Stevenson, S., Bailey, D., Liu, Z., Noone, D., Nusbaumer, J., et al. (2019). The connected isotopic water cycle in the community earth system model version 1. *Journal of Advances in Modeling Earth Systems*, *11*(8), 2547–2566.

Breitenbach, S. F. M., Rehfeld, K., Goswami, B., Baldini, J. U. L., Ridley, H. E., Kennett, D., et al. (2012). COnstructing Proxy-Record Age models (COPRA). *Climate of the Past*, *8*(5), 1765–1779.

Buckley, B. M., Anchukaitis, K. J., Penny, D., Fletcher, R., Cook, E. R., Sano, M., et al. (2010). Climate as a contributing factor in the demise of Angkor, Cambodia. *Proceedings of the National Academy of Sciences*, *107*(15), 6748–6752.

Buckley, B. M., Stahle, D. K., Luu, H. T., & Wang, S. Y. S. (2017). Central Vietnam climate over the past five centuries from cypress tree rings. *Climate Dynamics*. Retrieved from https://link.springer.com/article/10.1007/s00382-016-3297-y

Burns, S. J., Godfrey, L. R., Faina, P., McGee, D., Hardt, B., Ranivoharimanana, L., & Randrianasy, J. (2016). Rapid human-induced landscape transformation in Madagascar at the end of the first millennium of the Common Era. *Quaternary Science Reviews*, *134*, 92–99.

Cai, Z., & Tian, L. (2016). Atmospheric Controls on Seasonal and Interannual Variations in the Precipitation Isotope in the East Asian Monsoon Region. *Journal of Climate*, *29*(4), 1339–1352.

Carlson, A. E., & Clark, P. U. (2012). Ice sheet sources of sea level rise and freshwater discharge during the last deglaciation. *Reviews of Geophysics* , *50*(4). https://doi.org/10.1029/2011rg000371

Chawchai, S., Chabangborn, A., Kylander, M., Löwemark, L., Mörth, C.-M., Blaauw, M., et al. (2013). Lake Kumphawapi--an archive of Holocene palaeoenvironmental and palaeoclimatic changes in northeast Thailand. *Quaternary Science Reviews*, *68*, 59–75.

Chawchai, S., Liu, G., Bissen, R., Scholz, D., Riechelmann, D. F. C., Vonhof, H., et al. (2020). Hydroclimate variability of western Thailand during the last 1400 years. *Quaternary Science Reviews*, *241*, 106423.

Chawchai, S., Tan, L., Löwemark, L., Wang, H.-C., Yu, T.-L., Chung, Y.-C., et al. (2021). Hydroclimate variability of central Indo-Pacific region during the Holocene. *Quaternary Science Reviews*, *253*, 106779.

Chen, T.-C., Tsay, J.-D., Yen, M.-C., & Matsumoto, J. (2012). Interannual Variation of the Late Fall Rainfall in Central Vietnam. *Journal of Climate*, *25*(1), 392–413.

Cheng, H., Edwards, R. L., Broecker, W. S., Denton, G. H., Kong, X., Wang, Y., et al. (2009). Ice age terminations. *Science*, *326*(5950), 248–252.

Cheng, H., Lawrence Edwards, R., Shen, C.-C., Polyak, V. J., Asmerom, Y., Woodhead, J., et al. (2013). Improvements in 230Th dating, 230Th and 234U half-life values, and U–Th isotopic measurements by multi-collector inductively coupled plasma mass spectrometry. *Earth and Planetary Science Letters*, *371–372*, 82–91.

Cheng, H., Edwards, R. L., Sinha, A., Spötl, C., Yi, L., Chen, S., et al. (2016). The Asian monsoon over the past 640,000 years and ice age terminations. *Nature*, *534*(7609), 640–646.

Comas-Bru, L., Rehfeld, K., Roesch, C., Amirnezhad-Mozhdehi, S., Harrison, S. P., Atsawawaranunt, K., et al. (2020). SISALv2: a comprehensive speleothem isotope database with multiple age--depth models. *Earth System Science Data*, *12*(4), 2579–2606.

Cook, E. R., Anchukaitis, K. J., Buckley, B. M., D'Arrigo, R. D., Jacoby, G. C., & Wright, W. E. (2010). Asian monsoon failure and megadrought during the last millennium. *Science*, *328*(5977), 486–489.

Creveling, J. R., Mitrovica, J. X., Clark, P. U., Waelbroeck, C., & Pico, T. (2017). Predicted bounds on peak global mean sea level during marine isotope stages 5a and 5c. *Quaternary Science Reviews*, *163*, 193–208.

Cross, M., McGee, D., Broecker, W. S., Quade, J., Shakun, J. D., Cheng, H., et al. (2015). Great Basin hydrology, paleoclimate, and connections with the North Atlantic: A speleothem stable isotope and trace element record from Lehman Caves, NV. *Quaternary Science Reviews*, *127*, 186–198.

Daëron, M., Drysdale, R. N., Peral, M., Huyghe, D., Blamart, D., Coplen, T. B., et al. (2019). Most Earth-surface calcites precipitate out of isotopic equilibrium. *Nature Communications*, *10*(1), 429.

Dang, H., Jian, Z., Wang, Y., Mohtadi, M., Rosenthal, Y., Ye, L., et al. (2020). Pacific warm pool subsurface heat sequestration modulated Walker circulation and ENSO activity during the Holocene. *Science Advances*, *6*(42), eabc0402.

Day, C. C., & Henderson, G. M. (2013). Controls on trace-element partitioning in cave-analogue calcite. *Geochimica et Cosmochimica Acta*, *120*, 612–627.

Deininger, M., & Scholz, D. (2019). ISOLUTION 1.0: an ISOtope evoLUTION model describing the stable oxygen (δ18O) and carbon (δ13C) isotope values of speleothems. *International Journal of Speleology / Societa Speleologica Italiana*, *48*(1), 21–32.

Deininger, M., Fohlmeister, J., Scholz, D., & Mangini, A. (2012). Isotope disequilibrium effects: The influence of evaporation and ventilation effects on the carbon and oxygen isotope composition of speleothems--A model approach. *Geochimica et Cosmochimica Acta*, *96*, 57–79.

Deininger, M., Hansen, M., Fohlmeister, J., Schröder-Ritzrau, A., Burstyn, Y., & Scholz, D. (2021). Are oxygen isotope fractionation factors between calcite and water derived from speleothems systematically biased due to prior calcite precipitation (PCP)? *Geochimica et Cosmochimica Acta*, *305*, 212–227.

Di Nezio, P. N., Timmermann, A., Tierney, J. E., Jin, F.-F., Otto-Bliesner, B., Rosenbloom, N., et al. (2016). The climate response of the Indo-Pacific warm pool to glacial sea level. *Paleoceanography*, *31*(6), 866–894.

DiNezio, P. N., & Tierney, J. E. (2013). The effect of sea level on glacial Indo-Pacific climate. *Nature Geoscience*, *6*(6), 485–491.

Dorale, J. A., Edwards, R. L., Ito, E., & Gonzalez, L. A. (1998). Climate and vegetation history of the midcontinent from 75 to 25 ka: A speleothem record from crevice cave, missouri, USA. *Science*, *282*(5395), 1871–1874.

Dorale, Jeffrey A., Edwards, R. L., Alexander, E. C., Shen, C.-C., Richards, D. A., & Cheng, H. (2004). Uranium-Series Dating of Speleothems: Current Techniques, Limits, & Applications. In *Studies of Cave Sediments* (pp. 177–197). Springer US.

Dreybrodt, W. (1980). Deposition of calcite from thin films of natural calcareous solutions and the growth of speleothems. *Chemical Geology*, *29*(1), 89–105.

Du, T. L. T., Bui, D. D., Nguyen, M. D., & Lee, H. (2018). Satellite-Based, Multi-Indices for Evaluation of Agricultural Droughts in a Highly Dynamic Tropical Catchment, Central Vietnam. *WATER*, *10*(5), 659.

Du, X., Russell, J. M., Liu, Z., Otto-Bliesner, B. L., Gao, Y., Zhu, C., et al. (2021). Deglacial trends in Indo-Pacific warm pool hydroclimate in an isotope-enabled Earth system model and implications for isotope-based paleoclimate reconstructions. *Quaternary Science Reviews*, *270*, 107188.

Edwards, L. R., Chen, J. H., & Wasserburg, G. J. (1987). 238U234U230Th232Th systematics and the precise measurement of time over the past 500,000 years. *Earth and Planetary Science Letters*, *81*(2), 175–192.

Fairchild, I. J., & Baker, A. (2012). *Speleothem Science: From Process to Past Environments*. John Wiley & Sons.

Fairchild, I. J., & Treble, P. C. (2009). Trace elements in speleothems as recorders of environmental change. *Quaternary Science Reviews*, *28*(5), 449–468.

Fairchild, I. J., Borsato, A., Tooth, A. F., Frisia, S., Hawkesworth, C. J., Huang, Y., et al. (2000). Controls on trace element (Sr–Mg) compositions of carbonate cave waters: implications for speleothem climatic records. *Chemical Geology*, *166*(3), 255–269.

Fairchild, I. J., Smith, C. L., Baker, A., Fuller, L., Spötl, C., Mattey, D., et al. (2006). Modification and preservation of environmental signals in speleothems. *Earth-Science Reviews*, *75*(1), 105–153.

Fantle, M. S., & Tipper, E. T. (2014). Calcium isotopes in the global biogeochemical Ca cycle: Implications for development of a Ca isotope proxy. *Earth-Science Reviews*, *129*, 148–177.

Fleischer, R. L., & Raabe, O. G. (1978). Recoiling alpha-emitting nuclei. Mechanisms for uranium-series disequilibrium. *Geochimica et Cosmochimica Acta*, *42*(7), 973–978.

Fohlmeister, J., Voarintsoa, N. R. G., Lechleitner, F. A., Boyd, M., Brandtstätter, S., Jacobson, M. J., & L. Oster, J. (2020). Main controls on the stable carbon isotope composition of speleothems. *Geochimica et Cosmochimica Acta*, *279*, 67–87.

Frisia, S., Fairchild, I. J., Fohlmeister, J., Miorandi, R., Spötl, C., & Borsato, A. (2011). Carbon mass-balance modelling and carbon isotope exchange processes in dynamic caves. *Geochimica et Cosmochimica Acta*, *75*(2), 380–400.

Gabitov, R. I., Sadekov, A., & Leinweber, A. (2014). Crystal growth rate effect on Mg/Ca and Sr/Ca partitioning between calcite and fluid: An in situ approach. *Chemical Geology*, *367*, 70–82.

Genty, D., Blamart, D., Ouahdi, R., Gilmour, M., Baker, A., Jouzel, J., & Van-Exter, S. (2003). Precise dating of Dansgaard–Oeschger climate oscillations in western Europe from stalagmite data. *Nature*, *421*, 833.

Goldsmith, Y., Broecker, W. S., Xu, H., Polissar, P. J., deMenocal, P. B., Porat, N., et al. (2017). Northward extent of East Asian monsoon covaries with intensity on orbital and millennial timescales. *Proceedings of the National Academy of Sciences of the United States of America*, *114*(8), 1817–1821.

Griffiths, M. L., Drysdale, R. N., Gagan, M. K., Zhao, J.-X., Ayliffe, L. K., Hellstrom, J. C., et al. (2009). Increasing Australian–Indonesian monsoon rainfall linked to early Holocene sea-level rise. *Nature Geoscience*, *2*, 636.

Griffiths, Michael L., Johnson, K. R., Pausata, F. S. R., White, J. C., Henderson, G. M., Wood, C. T., et al. (2020). End of Green Sahara amplified mid- to late Holocene megadroughts in mainland Southeast Asia. *Nature Communications*, *11*(1), 4204.

Gussone, N., Böhm, F., Eisenhauer, A., Dietzel, M., Heuser, A., Teichert, B. M. A., et al. (2005). Calcium isotope fractionation in calcite and aragonite. *Geochimica et Cosmochimica Acta*, *69*(18), 4485–4494.

Hällberg, P. L., Schenk, F., Yamoah, K. A., Kuang, X., & Smittenberg, R. H. (2022). Seasonal aridity in the Indo-Pacific Warm Pool during the Late Glacial driven by El Niño-like conditions. *Climate of the Past*, *18*(7), 1655–1674.

Hansen, M., Scholz, D., Schöne, B. R., & Spötl, C. (2019). Simulating speleothem growth in the laboratory: Determination of the stable isotope fractionation (δ13C and δ18O) between H2O, DIC and CaCO3. *Chemical Geology*, *509*, 20–44.

He, C., Liu, Z., Otto-Bliesner, B. L., Brady, E. C., Zhu, C., Tomas, R., et al. (2021). Hydroclimate footprint of pan-Asian monsoon water isotope during the last deglaciation. *Science Advances*, *7*(4). https://doi.org/10.1126/sciadv.abe2611

He, Chengfei, Liu, Z., Otto-Bliesner, B. L., Brady, E. C., Zhu, C., Tomas, R., et al. (2021). Deglacial variability of South China hydroclimate heavily contributed by autumn rainfall. *Nature Communications*, *12*(1), 1–9.

Hellstrom, J. (2006). U–Th dating of speleothems with high initial 230Th using stratigraphical constraint. *Quaternary Geochronology*, *1*(4), 289–295.

Hellstrom, J. C., & McCulloch, M. T. (2000). Multi-proxy constraints on the climatic significance of trace element records from a New Zealand speleothem. *Earth and Planetary Science Letters*, *179*(2), 287–297.

Hendy, C. H. (1971). The isotopic geochemistry of speleothems—I. The calculation of the effects of different modes of formation on the isotopic composition of speleothems and their applicability as palaeoclimatic indicators. *Geochimica et Cosmochimica Acta*, *35*(8), 801–824.

Heuser, A., & Eisenhauer, A. (2008). The Calcium Isotope Composition (δ44/40Ca) of NIST SRM 915b and NIST SRM 1486. *Geostandards and Geoanalytical Research*, *32*(2), 27–32.

Hu, C., Henderson, G. M., Huang, J., Xie, S., Sun, Y., & Johnson, K. R. (2008). Quantification of Holocene Asian monsoon rainfall from spatially separated cave records. *Earth and Planetary Science Letters*, *266*(3), 221–232.

Huang, Y., & Fairchild, I. J. (2001). Partitioning of Sr2+ and Mg2+ into calcite under karst-analogue experimental conditions. *Geochimica et Cosmochimica Acta*, *65*(1), 47–62.

Husson, J. M., Higgins, J. A., Maloof, A. C., & Schoene, B. (2015). Ca and Mg isotope constraints on the origin of Earth's deepest δ13C excursion. *Geochimica et Cosmochimica Acta*, *160*, 243–266.

Ivanovich, M. (1982). Uranium series disequilibria applications in geochronology. In *Uranium series disequilibrium: applications to environmental problems*. inis.iaea.org.

Jacobson, A. D., Grace Andrews, M., Lehn, G. O., & Holmden, C. (2015). Silicate versus carbonate weathering in Iceland: New insights from Ca isotopes. *Earth and Planetary Science Letters*, *416*, 132–142.

Jaffey, A. H., Flynn, K. F., Glendenin, L. E., Bentley, W. C., & Essling, A. M. (1971). Precision measurement of half-lives and specific activities ofU235andU238. *Physical Review C: Nuclear Physics*, *4*(5), 1889–1906.

Jian, Z., Wang, Y., Dang, H., Mohtadi, M., Rosenthal, Y., Lea, D. W., et al. (2022). Warm pool ocean heat content regulates ocean-continent moisture transport. *Nature*, *612*(7938), 92–99.

Johnson, K. R. (2021). California's volatile hydroclimate: Lessons from the paleoclimate record. *Geophysical Research Letters*, *48*(23). https://doi.org/10.1029/2021gl095512

Johnson, K. R., Hu, C., Belshaw, N. S., & Henderson, G. M. (2006). Seasonal trace-element and stable-isotope variations in a Chinese speleothem: The potential for high-resolution paleomonsoon reconstruction. *Earth and Planetary Science Letters*, *244*(1), 394–407.

Johnston, P. (1993). The effect of spatially non-uniform water loads on prediction of sea-level change. *Geophysical Journal International*, *114*(3), 615–634.

Kalnay, E., Kanamitsu, M., Kistler, R., Collins, W., Deaven, D., Gandin, L., et al. (1996). The NCEP/NCAR 40-Year Reanalysis Project. *Bulletin of the American Meteorological Society*, *77*(3), 437–472.

Kendall, R. A., Mitrovica, J. X., & Milne, G. A. (2005). On post-glacial sea level--II. Numerical formulation and comparative results on spherically symmetric models. *Geophysical Journal International*, *161*(3), 679–706.

Kershaw, A. P., Penny, D., van der Kaars, S., Anshari, G., & Thamotherampillai, A. (2001). Vegetation and climate in lowland southeast Asia at the Last Glacial Maximum. *Faunal and Floral Migrations and Evolution in SE Asia-Australasia*, 227–236.

Kim, S.-T., & O'Neil, J. R. (1997). Equilibrium and nonequilibrium oxygen isotope effects in synthetic carbonates. *Geochimica et Cosmochimica Acta*, *61*(16), 3461–3475.

Lachniet, M. S. (2009). Climatic and environmental controls on speleothem oxygen-isotope values. *Quaternary Science Reviews*, *28*(5), 412–432.

Lambeck, K., Purcell, A., Johnston, P., Nakada, M., & Yokoyama, Y. (2003). Water-load definition in the glacio-hydro-isostatic sea-level equation. *Quaternary Science Reviews*, *22*(2), 309–318.

Lemarchand, D., Wasserburg, G. J., & Papanastassiou, D. A. (2004). Rate-controlled calcium isotope fractionation in synthetic calcite. *Geochimica et Cosmochimica Acta*, *68*(22), 4665–4678.

Li, R., Wang, S.-Y., Gillies, R. R., Buckley, B. M., Truong, L. H., & Cho, C. (2015). Decadal oscillation of autumn precipitation in Central Vietnam modulated by the East Pacific–North Pacific (EP–NP) teleconnection. *Environmental Research Letters: ERL [Web Site]*, *10*(2), 024008.

Li, X., Cui, X., He, D., Liao, J., & Hu, C. (2018). Evaluation of the Heshang Cave stalagmite calcium isotope composition as a paleohydrologic proxy by comparison with the instrumental precipitation record. *Scientific Reports*, *8*(1), 2615.

Liu, Z., Otto-Bliesner, B. L., He, F., Brady, E. C., Tomas, R., Clark, P. U., et al. (2009). Transient Simulation of Last Deglaciation with a New Mechanism for Bølling-Allerød Warming. *Science*, *325*(5938), 310–314.

Lüthi, D., Le Floch, M., Bereiter, B., Blunier, T., Barnola, J.-M., Siegenthaler, U., et al. (2008). High-resolution carbon dioxide concentration record 650,000–800,000 years before present. *Nature*, *453*(7193), 379–382.

Luu, C., Tran, H. X., Pham, B. T., Al-Ansari, N., Tran, T. Q., Duong, N. Q., et al. (2020). Framework of Spatial Flood Risk Assessment for a Case Study in Quang Binh Province, Vietnam. *Sustainability: Science Practice and Policy*, *12*(7), 3058.

Luu, C., Duy, B. Q., & Jason, von M. (2021). Mapping direct flood impacts from a 2020 extreme flood event in Central Vietnam using spatial analysis techniques. *International Journal of Disaster Resilience in the Built Environment*, *ahead-of-print*(ahead-of-print). https://doi.org/10.1108/IJDRBE-07-2021-0070

Lynch-Stieglitz, J., Schmidt, M. W., Gene Henry, L., Curry, W. B., Skinner, L. C., Mulitza, S., et al. (2014). Muted change in Atlantic overturning circulation over some glacial-aged Heinrich events. *Nature Geoscience*, *7*(2), 144–150.

Magiera, M., Lechleitner, F. A., Erhardt, A. M., Hartland, A., Kwiecien, O., Cheng, H., et al. (2019). Local and Regional Indian Summer Monsoon Precipitation Dynamics During Termination II and the Last Interglacial. *Geophysical Research Letters*, *46*(21), 12454–12463.

Maher, K., DePaolo, D. J., & Christensen, J. N. (2006). U–Sr isotopic speedometer: Fluid flow and chemical weathering rates in aquifers. *Geochimica et Cosmochimica Acta*, *70*(17), 4417–4435.

Martín-Chivelet, J., Muñoz-García, M. B., Cruz, J. A., Ortega, A. I., & Turrero, M. J. (2017). Speleothem Architectural Analysis: Integrated approach for stalagmite-based paleoclimate research. *Sedimentary Geology*, *353*, 28–45.

McGee, D., Quade, J., Edwards, R. L., Broecker, W. S., Cheng, H., Reiners, P. W., & Evenson, N. (2012). Lacustrine cave carbonates: Novel archives of paleohydrologic change in the Bonneville Basin (Utah, USA). *Earth and Planetary Science Letters*, *351–352*, 182–194.

Meyer, K., Breecker, D. O., Banner, J. L., & Guilfoyle, A. (2011). Carbon in karst: investigating sources, transport and isotopic fractionation to better inform the interpretation of speleothem climate records of central Texas caves (Vol. 2011, pp. PP31C-1876). ui.adsabs.harvard.edu.

Mickler, P. J., Stern, L. A., & Banner, J. L. (2006). Large kinetic isotope effects in modern speleothems. *GSA Bulletin*, *118*(1–2), 65–81.

Milne, G. A., & Mitrovica, J. X. (1996). Postglacial sea-level change on a rotating Earth: first results from a gravitationally self-consistent sea-level equation. *Geophysical Journal International*. Retrieved from https://academic.oup.com/gji/article-abstract/126/3/F13/2042362

Milne, Glenn A., Mitrovica, J. X., & Davis, J. L. (1999). Near-field hydro-isostasy: the implementation of a revised sea-level equation. *Geophysical Journal International*, *139*(2), 464–482.

Misra, V., & DiNapoli, S. (2014). The variability of the Southeast Asian summer monsoon. *International Journal of Climatology*, *34*(3), 893–901.

Mitrovica, J. X., Wahr, J., Matsuyama, I., & Paulson, A. (2005). The rotational stability of an ice-age earth. *Geophysical Journal International*, *161*(2), 491–506.

Nguyen-Thi, H. A., Matsumoto, J., Ngo-Duc, T., & Endo, N. (2012). A Climatological Study of Tropical Cyclone Rainfall in Vietnam. *Solaiat; Sociedad Odontologica Latino-Americana De Implantes Aloplasticos Y Transplantes*, *8*, 41–44.

Nusbaumer, J., Wong, T. E., Bardeen, C., & Noone, D. (2017). Evaluating hydrological processes in the C ommunity A tmosphere M odel V ersion 5 (C AM5) using stable isotope ratios of water. *Journal of Advances in Modeling Earth Systems*, *9*(2), 949–977.

Owen, R. A., Day, C. C., Hu, C.-Y., Liu, Y.-H., Pointing, Blättler, C. L., & Henderson, G. M. (2016). Calcium isotopes in caves as a proxy for aridity: Modern calibration and application to the 8.2 kyr event. *Earth and Planetary Science Letters*, *443*, 129–138.

Patterson, E. W., Johnson, K. R., Griffiths, M. L., Kinsley, C. W., McGee, D., Du, X., et al. (2023). Glacial changes in sea level modulated millennial-scale variability of Southeast Asian autumn monsoon rainfall. *Proceedings of the National Academy of Sciences*, *120*(27), e2219489120.

Pausata, F. S. R., Battisti, D. S., Nisancioglu, K. H., & Bitz, C. M. (2011). Chinese stalagmite δ18O controlled by changes in the Indian monsoon during a simulated Heinrich event. *Nature Geoscience*, *4*, 474.

Peltier, W. R., & Fairbanks, R. G. (2006). Global glacial ice volume and Last Glacial Maximum duration from an extended Barbados sea level record. *Quaternary Science Reviews*, *25*(23), 3322–3337.

Peltier, W. R., Argus, D. F., & Drummond, R. (2015). Space geodesy constrains ice age terminal deglaciation: The global ICE-6G_C (VM5a) model. *Journal of Geophysical Research, [Solid Earth]*, *120*(1), 450–487.

Petit, J. R., Jouzel, J., Raynaud, D., Barkov, N. I., Barnola, J.-M., Basile, I., et al. (1999). Climate and atmospheric history of the past 420,000 years from the Vostok ice core, Antarctica. *Nature*, *399*(6735), 429–436.

Peyraube, N., Lastennet, R., Denis, A., & Malaurent, P. (2013). Estimation of epikarst air PCO2 using measurements of water δ13CTDIC, cave air PCO2 and δ13CCO2. *Geochimica et Cosmochimica Acta*, *118*, 1–17.

Pico, T., Mitrovica, J. X., Ferrier, K. L., & Braun, J. (2016). Global ice volume during MIS 3 inferred from a sea-level analysis of sedimentary core records in the Yellow River Delta. *Quaternary Science Reviews*, *152*, 72–79.

Pico, T., Creveling, J. R., & Mitrovica, J. X. (2017). Sea-level records from the U.S. mid-Atlantic constrain Laurentide Ice Sheet extent during Marine Isotope Stage 3. *Nature Communications*, *8*, 15612.

Pico, T., McGee, D., Russell, J., & Mitrovica, J. X. (2020). Recent constraints on MIS 3 sea level support role of continental shelf exposure as a control on Indo-pacific hydroclimate. *Paleoceanography and Paleoclimatology*, *35*(8). https://doi.org/10.1029/2020pa003998

Polag, D., Scholz, D., Mühlinghaus, C., Spötl, C., Schröder-Ritzrau, A., Segl, M., & Mangini, A. (2010). Stable isotope fractionation in speleothems: Laboratory experiments. *Chemical Geology*, *279*(1), 31–39.

Ramesh, N., Nicolas, Q., & Boos, W. R. (2021). The Globally Coherent Pattern of Autumn Monsoon Precipitation. *Journal of Climate*, *34*(14), 5687–5705.

Reynard, L. M., Day, C. C., & Henderson, G. M. (2011). Large fractionation of calcium isotopes during cave-analogue calcium carbonate growth. *Geochimica et Cosmochimica Acta*, *75*(13), 3726–3740.

Richards, D. A., & Dorale, J. A. (2003). Uranium-series Chronology and Environmental Applications of Speleothems. *Reviews in Mineralogy and Geochemistry*, *52*(1), 407–460.

Risi, C., Bony, S., & Vimeux, F. (2008). Influence of convective processes on the isotopic composition (δ18O andδD) of precipitation and water vapor in the tropics: 2.

Physical interpretation of the amount effect. *Journal of Geophysical Research*, *113*(D19). https://doi.org/10.1029/2008jd009943

Ruggieri, E. (2013). A Bayesian approach to detecting change points in climatic records. *International Journal of Climatology*, *33*(2), 520–528.

Schilt, A., Baumgartner, M., Blunier, T., Schwander, J., Spahni, R., Fischer, H., & Stocker, T. F. (2010). Glacial–interglacial and millennial-scale variations in the atmospheric nitrous oxide concentration during the last 800,000 years. *Quaternary Science Reviews*, *29*(1), 182–192.

Sengupta, A., & Nigam, S. (2019). The Northeast Winter Monsoon over the Indian Subcontinent and Southeast Asia: Evolution, Interannual Variability, and Model Simulations. *Journal of Climate*, *32*(1), 231–249.

Skiba, V., & Fohlmeister, J. (2023). Contemporaneously growing speleothems and their value to decipher in-cave processes – A modelling approach. *Geochimica et Cosmochimica Acta*, *348*, 381–396.

Stein, A. F., Draxler, R. R., Rolph, G. D., Stunder, B. J. B., Cohen, M. D., & Ngan, F. (2015). NOAA's HYSPLIT atmospheric transport and dispersion modeling system. *Bulletin of the American Meteorological Society*, *96*(12), 2059–2077.

Stojanovic, M., Liberato, M. L. R., Sorí, R., Vázquez, M., Phan-Van, T., Duongvan, H., et al. (2020). Trends and Extremes of Drought Episodes in Vietnam Sub-Regions during 1980–2017 at Different Timescales. *WATER*, *12*(3), 813.

Stoll, H. M., Day, C., Lechleitner, F., Kost, O., Endres, L., Sliwinski, J., et al. (2022). Distinguishing the vegetation and soil component of δ 13 C variation in speleothem records from degassing and prior calcite precipitation effects. *Climate of the Past Discussions*, 1–30.

Sun, Yan, Wang, S.-Y. S., Li, R., Buckley, B. M., Gillies, R., & Hansen, K. G. (2018). Feasibility of Predicting Vietnam's Autumn Rainfall Regime Based on the Tree-Ring Record and Decadal Variability. *Climate*, *6*(2), 42.

Sun, Youbin, Wang, X., Liu, Q., & Clemens, S. C. (2010). Impacts of post-depositional processes on rapid monsoon signals recorded by the last glacial loess deposits of northern China. *Earth and Planetary Science Letters*, *289*(1), 171–179.

Sun, Youbin, Clemens, S. C., Morrill, C., Lin, X., Wang, X., & An, Z. (2011). Influence of Atlantic meridional overturning circulation on the East Asian winter monsoon. *Nature Geoscience*, *5*(1), 46–49.

Supharatid, S., Nafung, J., & Aribarg, T. (2021). Projected changes in temperature and precipitation over mainland Southeast Asia by CMIP6 models. *Journal of Water and Climate Change*, *13*(1), 337–356.

Tabor, C. R., Otto-Bliesner, B. L., Brady, E. C., Nusbaumer, J., Zhu, J., Erb, M. P., et al. (2018). Interpreting precession-driven δ 18 O variability in the south Asian monsoon region. *Journal of Geophysical Research*, *123*(11), 5927–5946.

Tang, J., Dietzel, M., Böhm, F., Köhler, S. J., & Eisenhauer, A. (2008). Sr2+/Ca2+ and 44Ca/40Ca fractionation during inorganic calcite formation: II. Ca isotopes. *Geochimica et Cosmochimica Acta*, *72*(15), 3733–3745.

Treble, P. C., Baker, A., Abram, N. J., Hellstrom, J. C., Crawford, J., Gagan, M. K., et al. (2022). Ubiquitous karst hydrological control on speleothem oxygen isotope variability in a global study. *Communications Earth & Environment*, *3*(1), 1–10.

Wang, J. K., Johnson, K. R., Borsato, A., Amaya, D. J., Griffiths, M. L., Henderson, G. M., et al. (2019). Hydroclimatic variability in Southeast Asia over the past two millennia. *Earth and Planetary Science Letters*, *525*, 115737.

Wang, S.-Y. S., Promchote, P., Truong, L. H., Buckley, B. M., Li, R., Gillies, R., et al. (2015). Changes in the autumn precipitation and tropical cyclone activity over Central Vietnam and its East Sea. Retrieved from https://academiccommons.columbia.edu/doi/10.7916/D8RX9C1K

Wang, Y., Cheng, H., Edwards, R. L., Kong, X., Shao, X., Chen, S., et al. (2008). Millennial- and orbital-scale changes in the East Asian monsoon over the past 224,000 years. *Nature*, *451*(7182), 1090–1093.

Wang, Y. J., Cheng, H., Edwards, R. L., An, Z. S., Wu, J. Y., Shen, C. C., & Dorale, J. A. (2001). A high-resolution absolute-dated late Pleistocene Monsoon record from Hulu Cave, China. *Science*, *294*(5550), 2345–2348.

Wassenburg, J. A., Riechelmann, S., Schröder-Ritzrau, A., Riechelmann, D. F. C., Richter, D. K., Immenhauser, A., et al. (2020). Calcite Mg and Sr partition coefficients in cave environments: Implications for interpreting prior calcite precipitation in speleothems. *Geochimica et Cosmochimica Acta*, *269*, 581–596.

Wen, X., Liu, Z., Wang, S., Cheng, J., & Zhu, J. (2016). Correlation and anti-correlation of the East Asian summer and winter monsoons during the last 21,000 years. *Nature Communications*, *7*, 11999.

Wendt, K. A., Pythoud, M., Moseley, G. E., Dublyansky, Y. V., Lawrence Edwards, R., & Spötl, C. (2020). Paleohydrology of southwest Nevada (USA) based on groundwater 234U/238U over the past 475 ky. *Gdańskie Studia Azji Wschodniej*. Retrieved from https://pubs.geoscienceworld.org/gsa/gsabulletin/article/570640/?searchresult=1

Wendt, K. A., Li, X., & Lawrence Edwards, R. (2021). Uranium–Thorium Dating of Speleothems. *Elements* , *17*(2), 87–92.

de Wet, C. B., Erhardt, A. M., Sharp, W. D., Marks, N. E., Bradbury, H. J., Turchyn, A. V., et al. (2021). Semiquantitative estimates of rainfall variability during the 8.2 kyr event in California using speleothem calcium isotope ratios. *Geophysical Research Letters*, *48*(3). https://doi.org/10.1029/2020gl089154

Wolf, A. (2023). *EasHyClustering: Use Python to plot meteorological data from HYSPLIT clustering*. Github. https://doi.org/10.5281/zenodo.7574382

Wolf, A., Roberts, W. H. G., Ersek, V., Johnson, K. R., & Griffiths, M. L. (2020). Rainwater isotopes in central Vietnam controlled by two oceanic moisture sources and rainout effects. *Scientific Reports*, *10*(1), 1–14.

Wong, C. I., & Breecker, D. O. (2015). Advancements in the use of speleothems as climate archives. *Quaternary Science Reviews*, *127*, 1–18.

Wong, T. E., Nusbaumer, J., & Noone, D. C. (2017). Evaluation of modeled land-atmosphere exchanges with a comprehensive water isotope fractionation scheme in version 4 of the C ommunity L and M odel. *Journal of Advances in Modeling Earth Systems*, *9*(2), 978–1001.

Wood, C. T. (2019). *Multiproxy speleothem analyses applied to late Pleistocene and Holocene hydrologic reconstruction in Southeast Asia*. UC Irvine. Retrieved from https://escholarship.org/content/qt1k76f87j/qt1k76f87j.pdf?t=q8rw0g

Wright, K. T., Johnson, K. R., Bhattacharya, T., Marks, G. S., McGee, D., Elsbury, D., et al. (2022). Precipitation in northeast Mexico primarily controlled by the relative warming of Atlantic SSTs. *Geophysical Research Letters*, *49*(11). https://doi.org/10.1029/2022gl098186

Wright, K. T., Johnson, K. R., Marks, G. S., McGee, D., Bhattacharya, T., Goldsmith, G. R., et al. (2023). Dynamic and thermodynamic influences on precipitation in Northeast Mexico on orbital to millennial timescales. *Nature Communications*, *14*(1), 2279.

Yamoah, K. A., Chabangborn, A., Chawchai, S., Schenk, F., Wohlfarth, B., & Smittenberg, R. H. (2016). A 2000-year leaf wax-based hydrogen isotope record from Southeast Asia suggests low frequency ENSO-like teleconnections on a centennial timescale. *Quaternary Science Reviews*, *148*, 44–53.

Yamoah, K. A., Chabangborn, A., Chawchai, S., Fritz, S., Löwemark, L., Kaboth-Bahr, S., et al. (2021). A muted El Niño-like condition during late MIS 3. *Quaternary Science Reviews*, *254*, 106782.

Yancheva, G., Nowaczyk, N. R., Mingram, J., Dulski, P., Schettler, G., Negendank, J. F. W., et al. (2007). Influence of the intertropical convergence zone on the East Asian monsoon. *Nature*, *445*(7123), 74–77.

Yang, H., Johnson, K. R., Griffiths, M. L., & Yoshimura, K. (2016). Interannual controls on oxygen isotope variability in Asian monsoon precipitation and implications for paleoclimate reconstructions. *Journal of Geophysical Research, D: Atmospheres*, *121*(14), 8410–8428.

Yatagai, A., Kamiguchi, K., Arakawa, O., Hamada, A., Yasutomi, N., & Kitoh, A. (2012). APHRODITE: Constructing a Long-Term Daily Gridded Precipitation Dataset for Asia

Based on a Dense Network of Rain Gauges. *Bulletin of the American Meteorological Society*, *93*(9), 1401–1415.

Yokoyama, Y., Esat, T. M., Thompson, W. G., Thomas, A. L., Webster, J. M., Miyairi, Y., et al. (2018). Rapid glaciation and a two-step sea level plunge into the Last Glacial Maximum. *Nature*, *559*(7715), 603–607.

Zhang, H., Griffiths, M. L., Chiang, J. C. H., Kong, W., Wu, S., Atwood, A., et al. (2018). East Asian hydroclimate modulated by the position of the westerlies during Termination I. *Science*, *362*(6414), 580–583.

Zhang, R., & Delworth, T. L. (2005). Simulated Tropical Response to a Substantial Weakening of the Atlantic Thermohaline Circulation. *Journal of Climate*, *18*(12), 1853–1860.